INVESTIGATION OF INTERFACES BY SECOND HARMONIC ELLIPSOMETRY

A Thesis Submitted to the

UNIVERSITY OF SOUTHAMPTON

in support of Candidature

for the

Degree of Doctor of Philosophy

By

Alasdair Kieran Alexander

September 2000

UNIVERSITY OF SOUTHAMPTON

ABSTRACT

FACULTY OF SCIENCE

CHEMISTRY

Doctor of Philosophy

INVESTIGATION OF SURFACE AND BULK PROPERTIES OF MATERIALS BY SECOND HARMONIC ELLIPSOMETRY

by Alasdair Kieran Alexander

Surface Second Harmonic Generation (SHG) and ellipsometry have been combined to give Second Harmonic Ellipsometry (SHE), a new technique, which already appears to be greater than the sum of the parent techniques.

X-, Y- and Z-cut quartz crystals were available for investigation, though the structure (α- or β-) and the direction of optical rotation for these was unknown. The three flats were investigated by ellipsometry, SHG and (for Y- and Z-Cuts) SHE. The results and fits for Z-cut quartz are presented here. Transmission ellipsometric experiments revealed that the rotation was anticlockwise about the optic or Z- axis and that the specific rotation in /mm matched closely with literature values. Also the X- and Y-Cut materials gave results expected for birefringent crystals. SHG experiments further revealed that the quartz was trigonal in structure and therefore was α-quartz (β- quartz is hexagonal). The intensities are fitted to a trigonal model with the $\chi^{(2)}$ components χ_{xxx} and χ_{xyz} being the only non-zero contributors. The presence of the chiral component, χ_{xyz} was particularly significant. The results for SHE are also presented, and the ellipsometric quantities Δ and ψ are fitted.

The dye molecule Rhodamine 6G (R6G) is also investigated by ellipsometry. Wavelength scans at variable angle of incidence and constant concentration, and fixed angle of incidence and variable concentration are presented. The results are fitted to give values of the refractive index components n and k for each wavelength. The model fits for all thicknesses over 10Å.

Finally, initial results for SHE from Liquid interfaces are presented. The results for water (non-zero Δ) were sensitive enough to detect the presence of an organic impurity, which was missed by surface tension. Δ reverted to 0° when the water filters were replaced. Results from Rhodamine 6G are also presented.

CONTENTS

"Every physicist thinks he knows what a photon is. I spent my life [trying] to find out what a photon is and I still don't know it."

Albert Einstein

DECLARATION

I performed the work described in this thesis in the Chemistry Department at the University of Southampton between October 1995 and September 1998. Those who assisted in this work are all acknowledged where applicable.

Alasdair Kieran Alexander

September 2000

ACKNOWLEDGEMENTS

I wish to thank my supervisor Dr Jeremy Frey for his enthusiasm and constant stream of ideas, which have kept the project moving forwards.

Dr Bob Greef has helped enormously in the ellipsometric side of the work and his VisualBasic skills are responsible for the SHE data acquisition and analysis programs.

Dr Rowland Spencer Smith has been particularly supportive and his eternally optimistic approach has been much appreciated. Again his programming ability has been much appreciated in both SHG and SHE data acquisition.

I am grateful to Professor Warren Lawrence and Andrew Timson who have been closely involved in this project. Their ideas and suggestions have led to many corrections and improvements to the technique.

Thanks to everyone at the workshop and glassblowing workshop for coping with some bizarre design requests and electronics workshop for much needed repairs.

Thanks to Frey Group members past, present and honorary, Warren, Mike, Steve, Adam, Sal, Lefty and Colin for help, ideas and entertainment.

I wish to thank The University of Southampton and Glaxo Wellcome plc for financial backing and in particular Dr George Tranter for useful discussions.

Thank you to my parents for their continued advice and support.

Finally, I am indebted to Ali for her proof reading skills, constant encouragement and support.

Chapter One

INTRODUCTION

The importance and diversity of the physical and chemical behaviour of surfaces has been known for centuries. Surface chemistry plays a vital role in everyday life, for example, transport of ions across a cell membrane, corrosion in metals and development of an image on photographic film. Although scientists have long been aware of the need to investigate surfaces, it has only been in the latter half of this century that major advances have been made. This is due mainly to the difficulty in distinguishing between a material's surface behaviour from its bulk properties, which are normally dominant.

1.1 Methods of Studying Surfaces

1) Surface and Interfacial Tension

The surface tension of a liquid interface can change dramatically from that of the pure liquid(s) upon addition of a surface-active agent (surfactant). Measured by a torsion balance, the addition of impurities affects the surface excess, which can be easily calculated. The main disadvantage of this technique is that only surfactant molecules give changes with acceptable margins of error.

2) Ultra High Vacuum (UHV) Techniques

In UHV conditions, the number of inter-atomic collisions near the surface is reduced and the environment can therefore be kept clean long enough to examine the surface. Pressures of the order of 10^{-11}-10^{-12} Torr can be used, corresponding to a collision frequency of once or twice per atom per hour. The surface is a single crystal, which can be polished or etched. It can then be cleaned by an electronic heater or by bombardment with accelerated gas.

3) Photoemission Spectroscopy

If X-ray or UV radiation strikes a material, electrons are emitted by its surface. When detected, X-rays lead to detailed information about the chemical composition of the surface, whereas UV radiation can reveal the valence shell electronic structures of the materials.

4) Electron Energy Loss Spectroscopy (EELS)

This technique monitors the energy loss suffered by a beam of electrons when it is reflected from a surface. The vibration spectrum of the adsorbate is recorded to high resolution and very tiny amounts of adsorbate can be detected.

5) Auger Electron Spectroscopy

The Auger Effect is the emission of a second electron after high-energy radiation has expelled an inner shell electron. Either the radiation generated (X-ray fluorescence) or the ejection of the second Auger electron is measured. The energies of the Auger electrons emitted are characteristic of the materials present.

6) Low Energy Electron Diffraction (LEED)

If an electron beam is directed onto a material, it will be scattered by the charges of the material's nuclei and electrons. If the energy of the beam is low enough, it will not be able to penetrate deeply (>2-3nm) into the material and the diffraction can only be caused by atoms on or close to the surface. This technique can reveal the presence of features such as terraces, steps and kinks in a surface and also the features' respective densities (density = number of features per unit area).

7) Scanning Probe Microscopy (SPM) Techniques.

These are variations on a method of imaging surfaces with atomic or near-atomic resolution. A small tip is scanned across the surface of a sample in order to construct a 3-D image of the surface. Fine control of the scan is accomplished using piezoelectrically induced motions. If the tip and the surface are both conducting, the structure of the surface can be detected by tunnelling of electrons from the tip to the surface (Scanning Tunnelling Microscopy, STM). Any type of surface can be probed by the molecular forces exerted by the surface against the tip (Atomic Force Microscopy, AFM). The tip can be constantly in contact with the surface, it can gently tap the surface while oscillating at high frequency, or it can be scanned just minutely above the surface. Measurements can be made under ambient conditions with little or no sample preparation required. Surface images can be digitally acquired, stored, and

manipulated. A highlight was the first direct observation of the double helix structure of DNA by STM (Ref. 1.1)

8) Molecular Beam Techniques

If a surface has been examined by LEED, it can be further investigated by directing a molecular beam onto it. If a known adsorbate reacts at the surface, the ejected products can be analysed by a mass spectrometer. The time of flight of a particle can be measured and interpreted in terms of its residence time on the surface.

9) Electrochemical Techniques

Many metal surfaces can be examined by electrochemical methods. For example, the rate of corrosion of metals and also the inhibition effect of galvanisation (coating with a layer of zinc which will corrode in preference to iron due to its more negative electrode potential. However, the zinc will survive due to its protection by a hydrated oxide layer).

10) Surface Enhanced Raman Spectroscopy (SERS)

Raman spectroscopy investigates the frequencies of radiation scattered by molecules. A monochromatic beam is passed through the sample and the radiation scattered perpendicular to the beam is monitored.

Under some conditions the Raman intensity can be greatly enhanced with signal intensity up to $\sim 10^6$ times greater than that predicted by calculations. The Raman intensity can be as much as 1 to 10 photons per second in the gas or liquid phase. It depends on molecules coupling to electromagnetic resonances of small (with respect to the wavelength of the light) metal particles. One major inconvenience is the presence of a strong fluorescent signal from the substrate.

Each of these techniques has its merits and has enhanced our knowledge of surfaces. However, this work concentrates on ellipsometry and second harmonic generation (SHG) and also on how they can be used together in a single experiment to provide even more information about both surface and bulk behaviour.

1.2 Ellipsometry

Ellipsometry is a linear optical technique, often used for studying surfaces, but in particular, it is the primary means available for the investigation of thin films (Ref. 1.3). Elliptically polarised light is obtained when linearly polarised light of a known orientation is reflected at oblique incidence from a surface. The shape and orientation of the ellipse are described by the parameters Δ and ψ, and depend on the angle of incidence, the direction of polarisation of the incident light, and the reflection properties of the surface. A complementary technique is polarimetry, which calculates the same parameters by transmission through the material. This provides more information about bulk properties of materials.

Ellipsometry was first practised at the end of the last century (Refs. 1.3-1.4). In 1901, Drude (Ref. 1.5) used the contemporary apparatus of a polariser, the surface in question, a compensator and an analyser. However, the term, "ellipsometry", was only coined in 1945 by Rothen (Ref. 1.6). These early experiments were conducted by a technique called nulling, which involves the extinguishing of the beam for a particular combination of polarisers. Unfortunately, the human eye was used as the detector of the null position and wasn't sensitive enough to measure the tiny differences around the null.

Later, rotating-analyser ellipsometry (RAE) was introduced (Refs. 1.7-1.8) which, when coupled with digital Fourier analysis techniques, led to a fast, precise instrument which was able to give immediate computer analysis of the measurement. Consequently, if a suitable model was chosen, film thickness could be calculated. It had the advantage of operating at high detected light levels compared to the nulling method. However, it was unable to distinguish between polarisation states, which have opposite handedness (Refs 1.9-1.10).

Hauge and Dill (Ref. 1.10) have shown that rotating compensator ellipsometry, a technique where a rotating retarder is placed before a fixed analyser, is a method of determining the complete polarisation state of a surface by a single measurement.

1.3 Second Harmonic Generation

Optical second harmonic generation (SHG) is the non-linear conversion of two photons of frequency ω to a single photon of frequency 2ω. It can be extremely surface selective, with only a few monolayers on either side of the interface participating in the effect (See Chapter 2). However, SHG is also possible from bulk materials, if the molecule under investigation is asymmetric. Sister techniques, which require two lasers, are SFG and DFG (sum and difference frequency generation). Here the two incident frequencies ω_1, ω_2 combine to give output frequencies $(\omega_1 + \omega_2)$ and $(\omega_1 - \omega_2)$ respectively.

Non - linear optical activity was first reported in 1961 when Franken and co-workers discovered that optical harmonics were measurable from three different cuts of quartz in transmission (Ref. 1.11). They were able to determine that X-cut quartz (surface in the YZ plane) gave no signal, Z-Cut gave a signal which was invariant as the sample was rotated and Y-cut would give a signal that varied with mechanical angle.

SHG in reflection has been developed into a powerful tool for investigating the properties of molecules in surface layers (Refs. 1.12-1.13). Bloembergen and co-workers derived the mathematical model for harmonic generation at the interface between a linear and non-linear medium. (Ref. 1.14)

After Franken's experiments, the Shen and Richmond groups have confirmed that the intensity of the reflected second harmonic varies, as an anisotropic, solid sample is rotated (Ref. 1.15-1.18).

The groups led by Shen, Eisenthal and Corn (Refs. 1.19-1.23) have played a major role in utilising the potential of SHG to investigate both liquid-air and liquid-liquid interfaces. Following their work, the molecular orientation of molecules at the interface can be determined (Ref. 1.23).

Hicks and co-workers (Refs. 1.24-1.29) are among those who have furthered the technique to study chiral molecules using the techniques of SHG-CD, where "CD" reflects the analogous behaviour to circular dichroism and SHG-ORD which exhibits optical rotary dispersion behaviour.

Rhodamine 6G (R6G) has long been considered an optically interesting material. Used in dye lasers to enable tuneable wavelengths (Ref. 1.30), R6G absorbs in the UV and visible regions of the spectrum. With absorptions close to both fundamental (560nm) and harmonic (280nm) wavelengths used in this work, it is ideal for study both by SHG (Refs. 1.31-1.34) and ellipsometry.

Crawford *et. al.* have investigated the dipeptide (t-butyloxycarbonyl)-tryptophan-tryptophan (Boc-Trp-Trp) and discovered that it is an ideal molecule to study optically, as it exhibits both SHG -CD and SHG-ORD (Ref. 1.35). Studies by Crawford (Ref. 1.36) and Fordyce (Ref. 1.37) have indicated that, although SHG intensity is measurable from both water and tryptophan, no SHG-CD or SHG-ORD behaviour was found.

1.4 Aims of the Thesis

The long - term aim of this work was to devise a new method of examining chiral liquid surfaces. A single experiment, which would give ellipsometric parameters at a second harmonic wavelength, was sought. This would enable SHG measurements to be obtained at the variety of incident angles that the ellipsometer facilitates. It would involve use of a pulsed laser, as used in SHG experiments.

This work involved the development of the technique and investigation of solid quartz samples in transmission and reflection. Further refinement of the experiment to accommodate the smaller SHG signals from liquid surfaces in reflection is also reported.

1.5 References

1.1 M. Salmeron *et. al., Science* **243** (1989) 370.

1.2 J. Lekner, *J. Opt. Soc. Am. A*, **5**, (1988) 1044.

1.3 P. Drude, *Wied. Ann.*, **43**, 126 (1891).

1.4 W. Spottiswoode, *Polarisation of Light*, Macmillan & Co., London (1874).

1.5 P. Drude, *Theory of Optics*, Longmans, Green & Co., New York (1901), p258.

1.6 A. Rothen, *Rev. Sci. Instruments*, **16**, 26 (1945).

1.7 P. S. Hauge and F. H. Dill, *IBM J. Res Devel.* **17** (1973) 472.

1.8 D. Aspnes, *Opt.Commun.*, **8** (1973) 22.

1.9 R.M.A. Azzam and N.M. Bashara, *J. Opt. Soc. Am.*, **64** (1974) 1459.

1.10 P. S. Hauge and F. H. Dill, *Opt. Commun.* **14**, 431 (1975).

1.11 P. A. Franken, A. E. Hill, C. W. Peters and G. Weinreich, *Phys. Rev. Lett.*, **7(4)** (1961) 118

1.12 T. L. Mazely and W. M. Hetherington III, *J. Chem. Phys.* **86** (1987) 3640.

1.13 T. F. Heinz, in *Non-linear Surface Electromagnetic Phenomena*, edited by H. E. Ponath and G. I. Stegemen, Elsevier, New York (1991) p353.

1.14 N. Bloembergen and P.S. Pershan, *The Physical Review* **128** (1962) 606-622.

1.15 H.W.K. Tom, T.F. Heinz and Y.R. Shen, Phys.Rev.Lett. 51 (1983) 1983.

1.16 H.W.K. Tom and G.D. Aumiller, *Phys Rev. B*, **33** (1986) 8818.

1.17 V.L. Shannon, D.A. Koos, and G.L. Richmond, J. Phys. Chem., 91 (1987) 5548.

1.18 D.A. Koos, V.L. Shannon, and G.L. Richmond, J. Phys. Chem., 94 (1990) 2091.

1.19 K. B. Eisenthal, *Acc. Chem. Res.* **26** (1993) 636-643.

1.20 Y. R. Shen, *Nature* **337** (1989) 519-525.

1.21 R. M. Corn and D. A. Higgins, *Chem. Rev.* **94** (1994) 107-125.

1.22 K.B. Eisenthal, *Annu. Rev. Phys. Chem.* **43** (1992) 627-661.

1.23 X. Zhuang, P.B. Miranda, D. Kim and Y.R. Shen, *Physical Review B,* **59** (1999) 12632

1.24 J. D. Byers, H. I. Yee and J.M. Hicks, *J. Chem. Phys.* **101** (1994) 6233.

1.25 T. Petralli-Mallow, T. M. Wong, J. D. Byers, H. I. Yee and J. M. Hicks, *J. Phys. Chem.* **97** (1993) 1383.

1.26 H. I. Yee, J. D. Byers, T. Petralli-Mallow and J. M. Hicks, in: *Laser techniques for state-selected and state to state chemistry*, ed. C. Ng, SPIE Conference

Proceedings, Vol. 1858 (Int. Soc. Opt. Eng., Bellingham, WA, 1993) p. 343.

1.27 J. D. Byers, H. I. Yee, T. Petralli-Mallow and J.M. Hicks, *Phys. Rev. B* **49** (1994) 14643.

1.28 J. D. Byers, and J.M. Hicks, *Chem. Phys. Lett.* **231** (1994) 216.

1.29 H. I. Yee, J. D. Byers, and J.M. Hicks, in: *Laser Techniques for surface science*, eds. H.L. Dai and S.J. Sibener, *SPIE Conference Proceedings*, **Vol. 2125** (Int. Soc. Opt. Eng., Bellingham, WA, 1994) p119.

1.30 P.P. Sorokin and J.R. Lankard, *IBM J Res. Dev.*, **11** (1967) 148.

1.31 T.F. Heinz, C.K. Chen, D. Ricard and Y.R. Shen, *Phys. Rev. Lett.*, **48** (1982) 478.

1.32 P. Di Lazzaro, P. Mataloni and F. De Martin, *Chem. Phys. Lett.*, **114** (1985) 103.

1.33 D.C. Nguyen, R.E. Muenchausen, R.A. Keller and N.S. Nogar, *Opt. Commun.*, **60** (1986) 111.

1.34 S.R. Meech and K Yoshihara, *Photochemistry and Photobiology*, **53** (1991) 627.

1.35 M. J. Crawford, S. Haslam, J. M. Probert, Y. A. Gruzdkov and J. G. Frey, *Chem. Phys. Lett.* **229** (1994) 260-264.

1.36 M.J. Crawford,Thesis, University of Southampton (1995).

1.37 A.J.G. Fordyce, Thesis, University of Southampton (1999).

Chapter Two

THEORY

2.1 The Properties of Light

There are two common models for describing the behaviour of light:

(i) it acts as if it were a train of waves;
(ii) it behaves as a random group of tiny particles (photons).

Each is valid for describing many kinds of problems but is incapable of explaining others. Fortunately, the two models complement each other; wave theory is suitable for describing situations involving intense beams of light, but for weak beams or those of short duration, particle theory is a suitable substitute.

2.1.1 Electromagnetic Theory of Light

This model was originally proposed by Maxwell, and is based on wave theory. The following assumptions are central to its application:

(i) Electrical waves are always accompanied by magnetic waves, travelling at $3x10^{10}$ cms^{-1} (usually called c) in free space. In this report, only the electric waves are described, as in most cases a solution valid for them is also valid for magnetic vibrations.
(ii) The waves are transverse, meaning that their electromagnetic displacements are perpendicular to the direction of travel.
(iii) At any point in space the electric and magnetic fields are mutually perpendicular.
(iv) As the waves spread out into any medium their amplitudes decrease steadily.
(v) At any given location, the power of the wave is proportional to the square of its amplitude.
(vi) When two waves are superimposed, the combined displacement at any given location and time is the vector sum of the two individual displacements.

2.1.2. Description of an Electromagnetic Wave

The electric field of a light wave oscillates and can be described by:

$$A = A_0 \sin[-\frac{2\pi}{\lambda}(x - vt) + \xi] \qquad \textbf{Equation 2.1}$$

where A is the amplitude of the electric field strength of the wave at any given time, A_0 is the maximum field strength, x is the distance along the direction of travel, t is time, v is the velocity of the light in the medium, λ is the wavelength and ξ is an arbitrary phase angle, which allows the offset of one wave against another when waves are combined.

The energy density is proportional to the square of the amplitude and the intensity, I is;

$$I = \frac{c\varepsilon_0 A_0^{\,2}}{8\pi} \qquad \textbf{Equation 2.2}$$

where c is the speed of light in the medium.

2.1.3 Reflection and Refraction

When light passes from one medium to another, some is usually reflected from the surface and some may enter the second medium.

In the second medium, the velocity of the light is slowed and refracted. The parameter used to describe the interaction of light with the material is the complex index of refraction, $\tilde{N}$, defined as:

$$\tilde{N} = n - ik \qquad \textbf{Equation 2.3}$$

where n is the index of refraction, k is the extinction coefficient (both quantities are dependent on wavelength) and i is $\sqrt{(-1)}$. For a dielectric material such as glass, k = 0,

in which case $\tilde{N}$ is equal to n. n is defined as the ratio of the velocity of light in free space, c, to the velocity of light in the medium, v:

$$n = c / v \qquad \textbf{Equation 2.4}$$

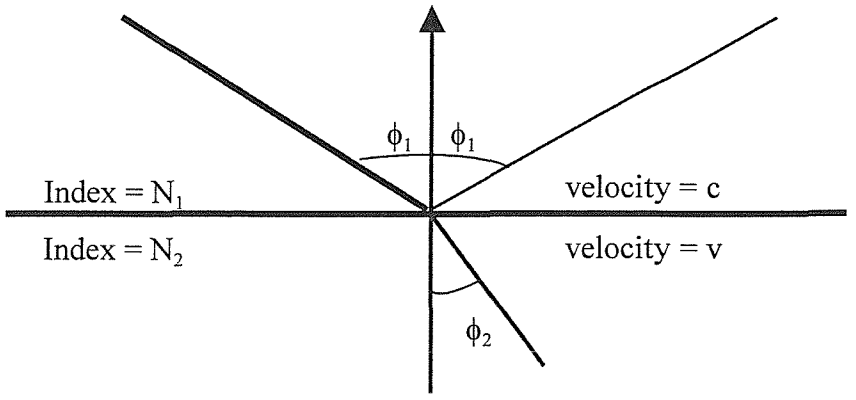

Figure 2.1 Reflection and Refraction at an Interface

k is given by:

$$k = \frac{\lambda}{4\pi}\alpha \qquad \textbf{Equation 2.5}$$

where α is the absorption coefficient of the medium and λ is the wavelength of the incident light. It originates from the relationship between the decrease in intensity per unit length, $\frac{dI(z)}{dz}$, and the intensity, I(z) :

$$\frac{dI(z)}{dz} = -\alpha I(z) \qquad \textbf{Equation 2.6}$$

Integrating gives

$$I(z) = I_0 \exp(-\alpha z) \qquad \textbf{Equation 2.7}$$

where I_0 is the value of the intensity at the surface of the absorbing medium. This relationship is known as the Beer - Lambert law.

The law of reflection states that the angle of reflection must always be equal to the angle of incidence. Both of these angles are measured from the surface normal.

The law of refraction, known as Snell's law, is given by

$$\tilde{N}_1 \sin \phi_1 = \tilde{N}_2 \sin \phi_2 \qquad \textbf{Equation 2.8}$$

with $\tilde{N}$ being replaced by n for dielectric materials (which by definition have k=0).

2.1.4. Polarised Light

Most light sources emit unpolarised light, which has components with electric fields oriented in random directions perpendicular to the direction of travel. Polarised light has a simple transverse vibration and all electric field vectors are oscillating in the same fashion. It is assumed that the light travels along the positive Z - axis of a right - handed co-ordinate system with the source at the origin. If the vibrations are viewed from a point at an infinite distance along the Z - axis from the source, a simple sectional pattern should be viewed.

Polarised light can be obtained by passing a laser beam through an optical element, called a polariser, or by causing the beam to make a specular reflection.

2.1.4.1. Reflection of Polarised Light

A suitable co-ordinate system for reflections is outlined in Figure 2.2 below. Plane polarised waves in the plane of incidence (the plane containing the incident beam, the normal to the surface and the outgoing beam) and those perpendicular to it are defined as p- waves and s- waves respectively.

The Fresnel reflection coefficient, r, is the ratio of the amplitude of the reflected wave to the amplitude of the incident wave for a single interface. The Fresnel reflection coefficients (Ref. 2.1) are given by

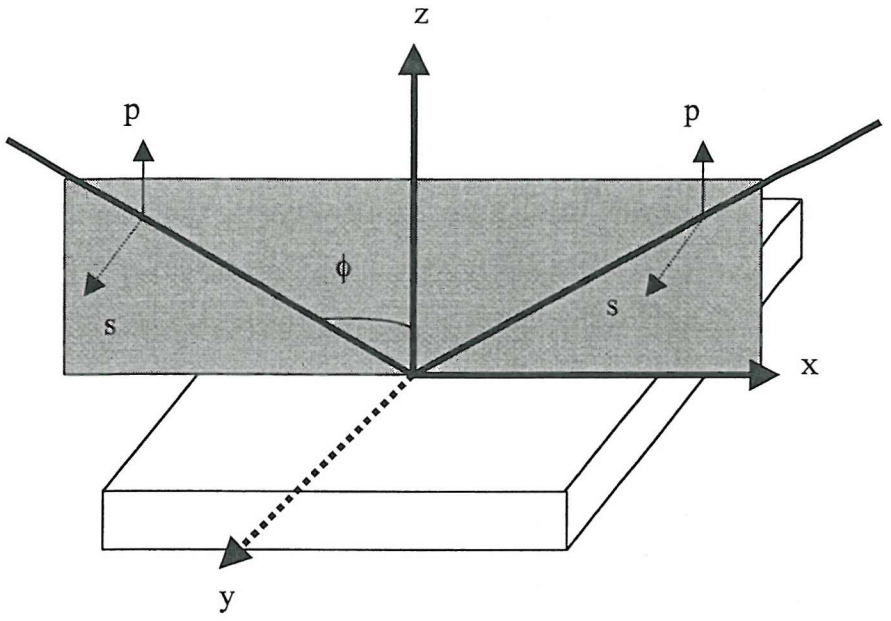

Figure 2.2 Laboratory and Polarisation Axes at a Surface. The grey Box denotes the Plane of Incidence, containing the input Beam, the output Beam and the Surface Normal. Solid Axes Lines are in the Plane of Incidence and dashed lines are perpendicular to it.

$$r_{12}^{p} = \frac{\tilde{N}_2 \cos\phi_1 - \tilde{N}_1 \cos\phi_2}{\tilde{N}_2 \cos\phi_1 + \tilde{N}_1 \cos\phi_2} \qquad r_{12}^{s} = \frac{\tilde{N}_1 \cos\phi_1 - \tilde{N}_2 \cos\phi_2}{\tilde{N}_1 \cos\phi_1 + \tilde{N}_2 \cos\phi_2} \qquad \textbf{Equations 2.9}$$

where the superscript refers to s or p polarised waves and the subscript refers to light going between media 1 and 2. Corresponding equations also exist for transmission (Ref. 2.2):

$$t_{12}^{p} = \frac{2\tilde{N}_1 \cos\phi_2}{\tilde{N}_2 \cos\phi_1 + \tilde{N}_1 \cos\phi_2} \qquad t_{12}^{s} = \frac{2\tilde{N}_1 \cos\phi_2}{\tilde{N}_1 \cos\phi_1 + \tilde{N}_2 \cos\phi_2} \qquad \textbf{Equations 2.10}$$

From Equation 2.2, the intensity of the light is proportional to the square of the amplitude of the reflected light, r. The reflectance, R, is defined as the ratio of the reflected intensity to the incident intensity. For a single interface, this can be written as

$$R^{p}=|r^{p}|^2 \qquad R^{s}=|r^{s}|^2 \qquad \textbf{Equations 2.11}$$

If both media are dielectric (e.g. air and quartz) the Fresnel equations and therefore the reflectances are much simpler.

For normal incidence, the angles ϕ_1 and ϕ_2 in Figure 2.1 are equal to 0 and all cosines in equations 2.9 are equal to unity:

$$r_{12}^{p} = \frac{n_2 - 1}{n_2 + 1} \qquad r_{12}^{s} = \frac{1 - n_2}{1 + n_2} \qquad R^p = R^s = \left(\frac{n_2 - 1}{n_2 + 1}\right)^2 \qquad \textbf{Equation 2.12}$$

For example, at the air / quartz interface ($n_1 = 1.0$; $n_2 = 1.567$ for O - ray (defined in section 2.1.4.2.) of quartz at $\lambda = 340$nm (Ref. 2.3)) R = 0.1309, meaning that over 13% of the initial intensity is reflected back towards the source.

For reflection experiments it can be seen that if $n_2 > n_1$, then, from Snell's law r^s is negative and non - zero. In addition, r^p changes from positive to negative with increasing angle. Therefore, for a certain angle r^p and R^p are both equal to zero, meaning that no light of the p polarisation will be reflected.

One of the simplest reflection type polarisers is a piece of plate glass that is mounted obliquely to the input beam of light (Figure 2.3). If mounted perpendicular to the beam, all components of the light are transmitted equally efficiently and no polarisation results. However, when the plate is tilted, both beams are partially polarised. The polarisation forms of the two beams are orthogonal.

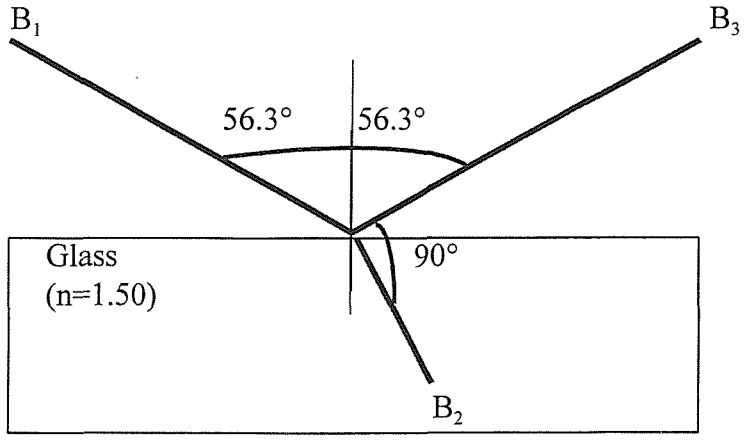

Figure 2.3 Reflection and Refraction at an Air / Glass Interface

When the incident angle is 56.3° and the incident beam is linearly p- polarised, the refracted beam B_2 is exactly perpendicular to the reflected beam, B_3. The vibration direction of B_2 is exactly parallel to B_3. Consequently, no energy is reflected in the B_3 direction.

In the case of unpolarised incident light the s- component is reflected moderately strongly (~15%) and the p - component not at all. The reflected beam is 100% polarised and contains about 8% of the incident energy with the remaining ~92% being transmitted in a partially polarised beam.

This particular angle (56.3° for glass) is known as Brewster's angle and is the only angle at which this phenomenon occurs. At no other angle does the refracted beam have a vibration exactly parallel to the reflected beam. Brewster's angle is $\tan^{-1}(n)$ so, for quartz (n =1.567 for O - ray (defined in section 2.1.4.2) at $\lambda = 340$nm (Ref. 2.3)), Brewster's angle is 57.46°.

2.1.4.2 Birefringence

When a single beam of unpolarised light is aimed at a uniaxial doubly refractive crystal (e.g. calcite), it is found that inside the crystal there are two orthogonal, 100% polarised beams, usually of different propagation speeds and directions. One of the beams usually has a direction of energy flow oblique to the wavefronts.

For a particular crystal and angle of incidence, the incident photons are constrained to one of these two paths which have pre-defined directions, velocities and polarisation forms. No other directions, velocities or polarisation forms are possible. One beam has a fixed speed for a particular material at a given wavelength (e.g. for 589nm light incident upon calcite, the slower beam always has a speed of $1.81 \times 10^8 ms^{-1}$ (Ref. 2.4). The fixed beam is called the ordinary ray (O - ray) and has a refractive index n_O. The other beam's normal speed varies with the particular direction of the vibration in the crystal and is called the extraordinary or E - ray with refractive index n_E. n_E can vary

between n_O and another extreme value n'_E. The difference between these values is the birefringence, J:

$$J = |n'_E - n_O| \qquad \textbf{Equation 2.13}$$

For calcite, $n'_E = 1.486$, $n_O = 1.658$ and $J = 0.172$ (Ref. 2.3), which is a comparatively large value. As $n'_E < n_O$ calcite is said to be a negative crystal. Quartz has $n'_E > n_O$ and is called positive (Ref. 2.3).

These two beams reduce to one when the light travels within a unique direction called the optic axis. If the incident beam is perpendicular to one particular crystal face, the material will act as though it was entering glass and no double refraction will occur.

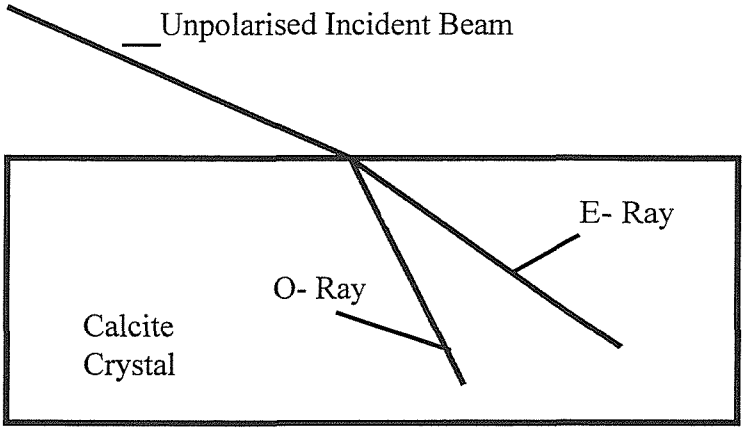

Figure 2.4 Refraction within a birefringent Optical Crystal showing the Ordinary and Extraordinary Ray Paths.

2.2 Ellipsometry

The two parameters sought in an ellipsometric experiment are the change in phase difference that occurs upon reflection, Δ, and the angle whose tangent is the ratio of the magnitudes of the total reflection coefficients, ψ.

Δ is defined as

$$\Delta = \delta_1 - \delta_2 \qquad \textbf{Equation 2.14}$$

where δ_1 and δ_2 are the phase differences between the parallel and perpendicular (p and s) components of the incoming and outgoing waves respectively. Δ can take any value between 0° and 360°. ψ can take values between 0° and 90° and is calculated by:

$$\psi = \tan^{-1} \frac{\left|r^p\right|}{\left|r^s\right|} \qquad \textbf{Equation 2.15}$$

ψ is represented graphically by Figure 2.5.

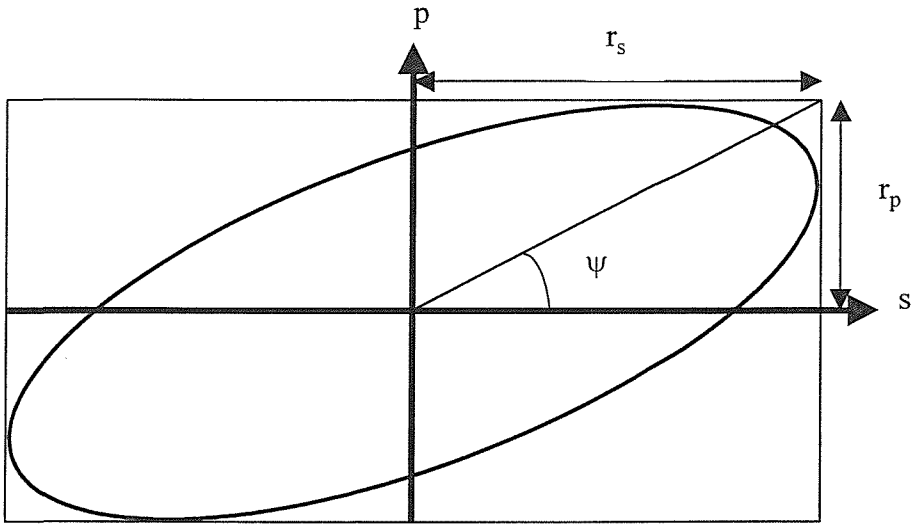

Figure 2.5 Diagrammatic representation of ψ where the ellipse describes the polarisation cross-section

Another quantity, ρ, is defined as the complex ratio of the total reflection coefficients such that

$$\rho = \frac{r^p}{r^s} \qquad \textbf{Equation 2.16}$$

From equations 2.14-2.16:

$$\rho = \frac{r^p}{r^s} = \tan\psi \exp(i\Delta)$$ **Equation 2.17**

where $i = \sqrt{(-1)}$. This equation is known as the fundamental equation of ellipsometry (Ref.2.5). Δ and ψ are measured by the ellipsometer and information about the sample is contained in the total reflection coefficients R^s and R^p.

If the instrument is working correctly, and a correct model is chosen, the thickness of the film and the refractive index of the material can be calculated.

2.2.1 Rotating Compensator Ellipsometry- Theory

The light intensities are recorded and saved, but the data can be analysed only after imperfections in the optical train are compensated for. The quarter wave plate only behaves perfectly at one wavelength (in this case 300nm), but the variation with wavelength is sufficiently manageable for it to be used at a wide range of wavelengths. To do this, the slight discrepancies in its behaviour have to be monitored and compensated for using a series of "defect files". A new defect file is required for each wavelength and is acquired by recording the light intensity, for the optical train described below;

Source - Polariser (45°) – Rotating Compensator - Analyser (0°) - Detector

For continuous defect files (used in the work on quartz), a xenon arc lamp was the source. For pulsed files the source was a second harmonic wave generated in transmission by a 1mm thick Z-cut quartz piece.

One hundred data points were acquired and averaged for each of 100 equally spaced quarter wave plate angles. These average values were saved to a text file for future analysis in a spreadsheet package.

The light must be sent straight through the optical train with no specular reflections. If the quarter wave plate is behaving perfectly, Δ and ψ will be recorded as 0° and 45° respectively. The defect file will consists of six parameters, the static phase angle, q, r, s, Δ_c and ψ_c.

Light of azimuth, P, and ellipticity, tan χ, is incident from the left. The detected light intensity is plotted against the azimuth of the compensator fast axis, with the analyser azimuth A as a reference. As the intensity curves for complementary polarisation states are clearly distinguishable, the degeneracy associated with opposite handed ellipticity in RAE and rotating analyser polarimetry is removed from RCE.

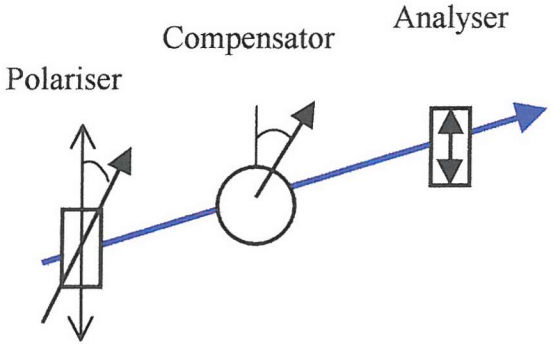

Figure 2.6 Rotating Compensator Polarimetry- arrangement of Polariser (Fixed Azimuth P = 45°), Compensator (Rotating through Angle C to the Fast Axis) and Analyser (Fixed at A = 0°)

Pure linear polarisation ($\chi = 0$) varies with the fourth harmonic and has unity relative amplitude and phase varying linearly with 2P. Pure circular polarisation ($\chi = \pm \pi/4$) is also instantly recognisable as it produces second harmonic polarisation with relative amplitude 2 and phase independent of P. The average value of the intensity has a component which is proportional to the linearly polarised part of the light and which is maximised when P = A and minimised when P = A $\pm \pi/2$. The exact form of the intensity for the ideal rotating compensator polarimeter is

$$I(C) = m\left(A_0 + A_2 \cos 2C + B_2 \sin 2C + A_4 \cos 4C + B_4 \sin 4C\right) \quad \textbf{Equation 2.18}$$

where m is a multiplicative constant and the coefficients $A_0 - B_4$ are given by

$$\begin{aligned} A_0 &= 2 + 2\cos\chi\cos 2(A - P) \\ A_2 &= 2\sin 2\chi \sin 2A \\ B_2 &= -2\sin 2\chi \cos 2A \\ A_4 &= \cos 2\chi \cos 2(A + P) \\ B_4 &= \cos 2\chi \sin 2(A + P) \end{aligned} \quad \textbf{Equations 2.19}$$

In most of this work, with a polariser set to transmit 45° linearly polarised light and an analyser set at 0°, P = 45°, $\chi = 0°$ and A = 0°. Note that for circularly polarised light the ellipticities are $\pi/4$ and $-\pi/4$ respectively and not $\pm \pi/2$. The effect of these values on the harmonic coefficients is shown for selected polarisations in Table 2.1.

In general the Jones matrix (Ref. 2.6) of the compensator will be

$$\begin{pmatrix} 1 & 0 \\ 0 & \rho_c \end{pmatrix} \quad \textbf{Equation 2.20}$$

where

$$\begin{aligned} \rho_c &= \tan\psi_c \exp(-i\Delta_c) \\ \psi_c &\cong \pi/4 \\ \Delta_c &\cong \pi/2 \end{aligned} \quad \textbf{Equations 2.21}$$

The defect parameters, q, r and s are used to express the non-ideal behaviour and are calculated in the following manner with the right hand column of numbers referring to an ideal quarter wave plate:

$$\begin{aligned} q &= 1 + \sin 2\psi_c \cos\Delta_c & &\cong 1 + \cos\Delta_c & &\cong 1 \\ r &= & \sin 2\psi_c \sin\Delta_c & &\cong 1 & \cong 1 \\ s &= & \cos 2\psi_c & &\cong 1 - \tan\psi_c & \cong 0 \end{aligned} \quad \textbf{Equations 2.22}$$

Δ_c describes the change in phase shift with wavelength from the perfect quarter wave (i.e. it is equal to 90° at 300nm) and ψ_c monitors the variation of ψ from the expected 45° with wavelength. In effect, the static phase angle and ψ_c are expected to be constant with wavelength.

Light Type	α	χ	A	A_0	A_2	B_2	A_4	B_4
45 linear in p out	45	0	0	2	0	0	0	1
45 linear in s out	45	0	90	2	0	0	0	-1
p linear in p out	0	0	0	3	0	0	1	0
p linear in s out	0	0	90	1	0	0	-1	0
Right circular in p out	45	45	0	2	0	-2	0	0
Right circular in s out	45	45	90	2	0	2	0	0
Left circular in p out	45	135	0	2	0	2	0	0
Left circular in s out	45	135	90	2	0	-2	0	0

Table 2.1 **The Harmonic Coefficients A_0, A_2, B_2, A_4 and B_4 for selected Values of Polariser Azimuth, P, Incident Light Ellipticity, χ, and Analyser Azimuth, A.**

The RCE has two possible configurations, depending upon whether the compensator is placed before (PCSA configuration) or after (PSCA) reflection from the surface. In each case the polariser and analyser are set at suitable azimuths, P and A respectively, and fixed. The intensity of the light emerging from the analyser is measured using a photomultiplier tube and the data analysed using a digital Fourier method.

For the PSCA case the polariser-sample dependent quantities μ and ν are defined as

$$\mu = (\cos 2P - \cos 2\psi)/(1 - \cos 2P \cos 2\psi)$$
$$\nu = \sin 2P \sin 2\psi \cos \Delta/(1 - \cos 2P \cos 2\psi)$$

Equations 2.23

When cos Δ approaches ± 1, the experimental uncertainty in determining Δ becomes excessive. For this reason, both cos Δ and sin Δ (the product of cos Δ and tan Δ) are

obtained. Thus, Δ may be obtained from whichever of these has the smallest absolute value and the sign of the other will provide the information as to which of the quadrants contains Δ.

Therefore, assuming that the polariser and analyser are perfect, the sample parameters Δ and ψ can be obtained after observing the corresponding Fourier coefficients:

$$
\begin{aligned}
A_0 &= 2 + q(\nu \sin 2A + \mu \cos 2A) \\
A_2 &= -2r(\nu \tan \Delta) \sin 2A + 2s(\cos 2A + \mu) \\
B_2 &= 2r(\nu \tan \Delta) \cos 2A + 2s(\sin 2A + \mu) \\
A_4 &= (2 - q)(\mu \cos 2A - \nu \sin 2A) \\
B_4 &= (2 - q)(\mu \sin 2A + \nu \cos 2A)
\end{aligned}
$$

Equations 2.24

For the PCSA configuration, the coefficients are obtained by switching P and A in equations 2.22 and 2.23.

If $P = \pi/4$ and $A = 0$ then $\mu = -\cos 2\psi$ and $\nu = \sin 2\psi \cos\Delta$, leading to the following coefficients:

$$
\begin{aligned}
A_0 &= 2 - q \cos 2\psi \\
A_2 &= 2s(1 - \cos 2\psi) \\
B_2 &= 2 \sin 2\psi (r \sin \Delta + 2s \cos \Delta) \\
A_4 &= (q - 2) \cos 2\psi \\
B_4 &= (2 - q) \sin 2\psi \cos \Delta
\end{aligned}
$$

Equations 2.25

The compensator can be calibrated by evaluating defect parameters at each wavelength to be used in measurements in the PCA configuration. Here, provided the polarisers are not crossed ($P \neq A \pm \pi/2$), we can use equations 2.24 with

$$
\begin{aligned}
\mu &= \cos 2P \\
\nu &= \sin 2P \\
\Delta &= 0
\end{aligned}
$$

Equations 2.26

A final parameter should be introduced to ensure full calibration. The static phase angle compensates for any difference between the fast axis of the quarter wave plate and the 0° point on its mount. Ignoring this value will lead to confusion in assigning the values of Δ and ψ.

Once calibrated, PSCA measurements yield μ and ν, and hence $\cos 2\psi$ and $\cos\Delta$, from the fourth harmonic coefficients. The coefficients A_2 and B_2 then are used to eliminate the ambiguity (present in RAE) in obtaining Δ from its cosine, by giving the sign of $\tan\Delta$. Hence ψ and Δ are unambiguously determined.

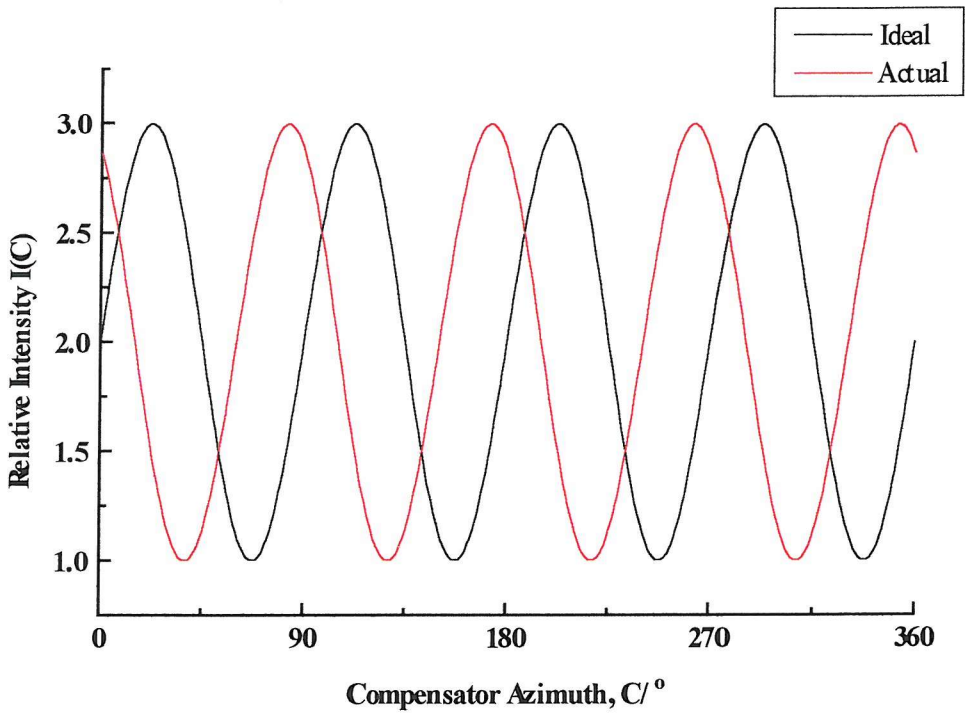

Figure 2.7 **Graph illustrating the static phase angle. The measured intensity curve is 120° out of phase with the ideal one. This would give a static phase angle of -60°**

2.2.2 Dispersion

The refractive index of a material will be dependent on the wavelength of the irradiating source, a property known as dispersion.

In a dielectric material, an atom can scatter incoming radiation without otherwise altering it, or it can absorb it. If the photon's energy is equal to that of one of the excited states of the molecule, the molecule will absorb the light, making a quantum jump to that higher energy level. In a liquid sample, this energy will quickly be converted to thermal energy, before a photon is emitted.

Ground state or non-resonant scattering occurs at other frequencies when low energy photons cause the electron cloud of the molecule, which is in its ground state, to oscillate. This oscillating negative charge will vibrate with respect to the positive nucleus, forming an oscillating dipole, which should radiate elastically at the same frequency.

When a material is illuminated with white light, non-resonant scattering occurs at frequencies well away from an absorption. However, as the irradiating light moves closer to the wavelength of the absorption, the thermal dissipative process will become significant.

Lorentz introduced a model basing the molecule as a dipole oscillator. The contributions of large numbers of molecules can then be averaged to represent the behaviour of an isotropic dielectric medium.

At frequencies increasingly above resonance, the oscillator undergoes displacements, which are about 180° out of phase with the driving force. The resulting electric polarisation will be out of phase with electric field. Therefore, the permittivity and the refractive index will both be less than 1. At frequencies below resonance the electric field will be nearly in phase with the applied electric field and the permittivity and refractive index will be greater than unity.

In the dispersion equation, the medium is viewed as a collection of driven damped oscillators, some of which correspond to free electrons and will therefore have zero restoring force, whereas others will be bound to the atom.

$$n^2(\omega) = 1 + \frac{Nq_e^2}{\varepsilon_0 m_e}\left[\frac{f_e}{-\omega^2 + i\gamma_e\omega} + \sum_j\left(\frac{f_j}{\omega_{0j}^2 - \omega^2 + i\gamma_j\omega}\right)\right] \qquad \textbf{Equation 2.27}$$

ε_0 is the permittivity of a vacuum and N is the number of molecules per unit volume. f_e is the force exerted on the free electron of mass m_e and charge q_e by the applied field E(t) of a harmonic wave of frequency ω. f_j oscillators have natural frequencies ω_{0j} (j = 1,2,3...);

The f_j terms must satisfy the constraint $\sum_j f_j = 1$. They are known as transition probabilities.

To avoid the situation when ω is equal to any of the characteristic frequencies and n is discontinuous, a damping factor (γ_e and γ_j for the free and bound electrons respectively) must be introduced to the denominators of the right hand side of the equation. This damping is due to the energy lost when the forced oscillators re-radiate. In solid and liquid samples, inter-atomic distances are much greater than for a gas at standard temperature and pressure. Consequently, these atoms will be subject to strong interactions and a resulting frictional force. This will lead to a damping of the oscillators and a dissipation of their energy as heat, in the form of random molecular motion.

2.2.3 Determining Thickness of Films

To investigate the properties of films, we first need to be able to know the refractive index $\tilde{N}_3$ of the underlying substrate. The model is for the system shown in Figure 2.8 below.

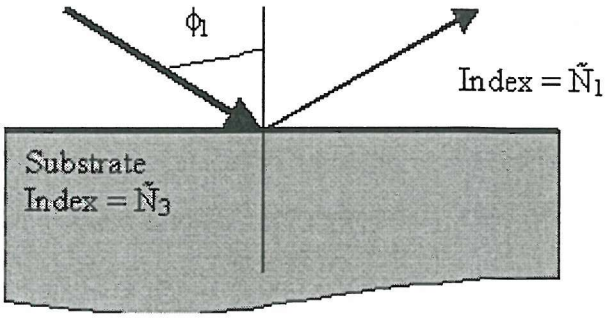

Figure 2.8 Schematic diagram of a light beam reflecting from a substrate

$$\tilde{N}_3 = \tilde{N}_1 \tan\phi_1 \sqrt{1 - \frac{4\rho \sin^2 \phi_1}{(\rho+1)^2}} \qquad \textbf{Equation 2.28}$$

This can be separated into the following equations (Ref. 2.7)

$$n_3^2 - k_3^2 = n_1^2 \sin^2 \phi_1 \left[1 + \frac{\tan^2 \phi_1 (\cos^2 2\psi - \sin^2 \Delta \sin^2 2\psi)}{(1 + \sin 2\psi \cos \Delta)^2} \right] \qquad \textbf{Equation 2.29}$$

$$2n_3 k_3 = \frac{n_1^2 \sin^2 \phi_1 \tan^2 \phi_1 \sin 4\psi \sin \Delta}{(1 + \sin 2\psi \cos \Delta)^2} \qquad \textbf{Equation 2.30}$$

As the right hand sides of Equations 2.29 and 2.30 must be positive, the following conclusions can be drawn for bare substrates:

Δ is 0° or 180° for dielectrics (k = 0) and between 0° and 180° for absorbing media ($\sin\Delta>0$, $k>0$).

ψ is between 0° and 45° for all substrates as in Equation 2.30 $\sin 4\psi$ must be positive.

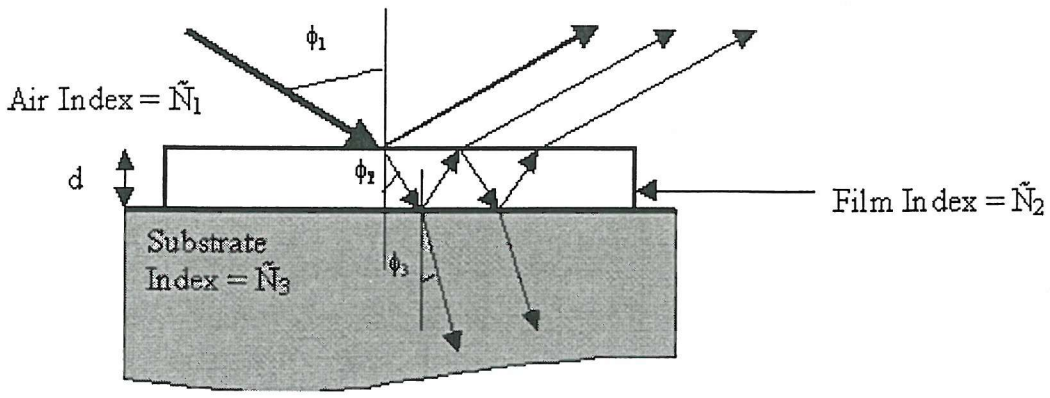

Figure 2.9 Schematic diagram of a light beam reflecting from a film on a substrate

For a single film model, the resultant reflected wave returning to the detector consists of light reflected by the film/air and the film/substrate interfaces. The wave travels in

$$R^p = \frac{r_{12}^p + r_{23}^p \exp(j2\beta)}{r_{12}^p r_{23}^p (j2\beta)} \qquad R^s = \frac{r_{12}^s + r_{23}^s \exp(j2\beta)}{r_{12}^s r_{23}^s (j2\beta)} \qquad \textbf{Equations 2.31}$$

where the 23 subscript denotes the Fresnel reflection coefficients between medium 2 and medium 3. β is the film phase thickness and is related to the film thickness, d, by

$$\beta = 2\pi\left(\frac{d}{\lambda}\right)\tilde{N}_2 \cos\phi_2 \qquad \textbf{Equation 2.32}$$

As d→0, then Rp and Rs become equal to the Fresnel coefficient between medium 1 and medium 3.

The reflectance $\Re$ is given by

$$\Re^p = |R^p|^2 \qquad \Re^s = |R^s|^2 \qquad \textbf{Equations 2.33}$$

For the one film model, zero thickness corresponds to the Δ/ψ points of the substrate, whereas very thick films will give the Δ/ψ point of the bulk film material. Intermediate thicknesses will give intermediate values of the Δ/ψ point.

2.3 Second Harmonic Generation

Optical second harmonic generation (SHG) is the non-linear conversion of two photons of frequency ω to a single photon of frequency 2ω. It can be extremely surface selective, with only a few monolayers on either side of the interface participating in the effect, because of the symmetry of the surface and the bulk. However, it can be obtained from bulk samples, if the molecule under investigation is chiral.

2.3.1 Theory of Second Harmonic Generation

When radiation at frequency, ω, with electric vector, **E**, passes through a medium, a polarisation **P** is induced:

$$\mathbf{P} = \mu + \varepsilon_0(\chi_1\mathbf{E} + \chi_2\mathbf{EE} + \chi_3\mathbf{EEE} + ...) \qquad \textbf{Equation 2.34}$$

μ is the permanent dipole, ε_0 is the permittivity of free space and χ_n is the nth order susceptibility, corresponding to frequency $n\omega$ in the case of SHG or $(\omega_1 + \omega_2)$ in the case of SFG. χ_1 is the linear susceptibility of the medium, and χ_2 and higher order susceptibilities correspond to non-linear properties. Each of these terms gives rise to a polarisation, which is much smaller for the non-linear terms (for reflection from 4-nitrophenol (PNP) at the air/water interface, $\chi_1/\chi_2 = 5\text{x}10^6\,\text{Vm}^{-1}$-Ref. 2.8). For low intensity light ($<1\text{MWcm}^{-2}$) and most substances, **P** is dominated by the χ_1 term in Equation 2.34. However, for highly intense laser radiation ($>1\text{MWcm}^{-2}$) and suitable materials, the second and subsequent terms become significant.

SHG arises from the non-linear polarisation $\mathbf{P}_2$, induced in the bulk or at the interface:

$$\mathbf{P}_2 = \varepsilon_0 \chi_2 \mathbf{E}\mathbf{E} \qquad \textbf{Equation 2.35}$$

Substituting the equation for an electromagnetic wave:

$$\mathbf{E} = E^0 \cos(\omega t).\underline{\hat{e}} \qquad \textbf{Equation 2.36}$$

into equation 2.35,

$$\mathbf{P_2} = \varepsilon_0 \chi_2 \left(E^0\right)^2 (1 + \cos 2\omega t)\underline{\hat{e}}.\underline{\hat{e}} \qquad \textbf{Equation 2.37}$$

The first term is a static polarisation, which produces a DC electric field in the medium. This is known as an optical rectification (Refs. 2.9-2.10). The second term produces a polarisation, which oscillates at twice the frequency of the fundamental and thus may radiate at the second harmonic wavelength.

The SHG intensity therefore depends on the square of the intensity of the fundamental radiation and the second order macroscopic susceptibility, χ_2. This is discussed in more detail in section 2.3.1.2.

2.3.1.1 Origin of Surface Specificity

In an isotropic medium, if an electric field, **E**, induces a second harmonic polarisation $\mathbf{P}_2$, an electric field in the opposite direction **–E**, will induce a polarisation $-\mathbf{P}_2$ in the opposite direction. Equation 2.35 becomes:

$$-\mathbf{P}_2 = \varepsilon_0 \chi_2 \mathbf{E}\mathbf{E} \qquad \textbf{Equation 2.38}$$

As the medium is centrosymmetric, equations 2.35 and 2.38 are equal, which can only occur if $\chi_2 = 0$ and therefore no second harmonic is produced.

However, all anisotropic media will produce a second harmonic. Optically active crystals such as lithium niobate, $LiNbO_3$ and quartz can therefore produce easily detectable beams. This requires a large χ_2 and phase matching between the fundamental and second harmonic beams. As gases and liquids are by definition isotropic, there may seem to be a problem in examining them. However, at an interface, inversion symmetry is broken and SHG is possible.

On a microscopic level $\chi^{(2)}$ can also be described as:

$$\chi^{(2)} = -\zeta \frac{Ne^3}{2m^2} \frac{1}{(\omega_0{}^2 - \omega^2)^2(\omega_0{}^2 - 4\omega^2)} \qquad \textbf{Equation 2.39}$$

N is the number of electrons, with mass m and charge e, per unit volume. $\chi^{(2)}$ is directly proportional to the potential field anharmonicity, ζ, meaning that a molecule must have an asymmetric electron density distribution for $\chi^{(2)}$ to be non zero and for SHG to occur. Consequently, SHG is observed only in a solid non-centrosymmetric system or at an interface.

When $\omega = \omega_0$ or $0.5\omega_0$, where ω_0 is the resonant frequency, the bottom line in Equation 3.39 becomes zero and resonance occurs for $\chi^{(2)}$. When resonant with an electronic transition in an adsorbed molecule (for harmonic generation at a surface), adsorbate contributions to $\chi^{(2)}$ may dominate the SHG from the surface, leading to resonant SHG.

2.3.1.2 The Non-linear Susceptibility Tensor, $\vec{\chi}^{(2)}$

χ_2 is a third rank tensor, $\vec{\chi}^{(2)}$, defined in general by a set of 27 elements ($\chi^{(2)}_{ijk}$ where i, j and k can be any of the laboratory x, y and z co-ordinate axes). Here, i refers to the beam oscillating at 2ω, and j and k to the photons oscillating at the fundamental frequency. The incident field components E_j and E_k can induce a second harmonic surface polarisation component:

$$P_i = \varepsilon_0 \sum_j \sum_k \chi^{(2)}_{ijk} E_j E_k \qquad \textbf{Equation 2.40}$$

This component is responsible for the generation of the i-component of the second harmonic field. The symmetry of the system restricts the number of independent components of $\chi^{(2)}_{ijk}$.

2.3.1.3 Second Harmonic Intensity

The intensity of the reflected second harmonic wave, I(2ω), is described by Equation 2.41 (Refs. 2.11-2.12):

$$I(2\omega) = \frac{32\pi^3 \omega^2 \sec^2 \phi}{c^3} \left| \underline{e}(2\omega).\chi^{(2)}.\underline{e}(\omega)\underline{e}(\omega) \right|^2 I^2(\omega) \qquad \textbf{Equation 2.41}$$

ϕ is the angle of incidence relative to the surface normal, I(ω) is the intensity of the input radiation, $\underline{e}(\omega)$ and $\underline{e}(2\omega)$ are polarisation vectors describing the electric field at the interface at frequencies ω and 2ω, and c is the speed of light in a vacuum.

The intensity is dependent upon the following factors:

1) The average molecular orientation at the surface,
2) The proximity of either the fundamental or second harmonic frequency to an absorption in the molecule and,
3) The non-linear optical response of the molecules.

2.3.1.4 Macroscopic to Molecular

The SHG process can be described mathematically using the third rank tensor χ_2 and simplified by ignoring molecule - molecule interactions and by considering any symmetry that exists on the surface. For molecular surfaces, the effective tensor is a geometric average of the molecular hyperpolarisability, α_2, of the surface molecules.

$$\vec{\chi}^{(2)} \propto N_D \vec{\alpha}^{(2)} \qquad \textbf{Equation 2.42}$$

where N_D is the number density of surface molecules. The $\vec{\chi}^{(2)}$ tensor is thus a function of the molecular hyperpolarisability and the molecular orientation at the surface. At liquid surfaces, the molecular orientation is usually random with respect to rotations in the plane. The net macroscopic non-linear susceptibility must also be invariant to rotation about the perpendicular z-axis.

The elements of the macroscopic tensor $\chi^{(2)}_{ijk}$ and the microscopic polarisability tensor $\alpha^{(2)}$ can be reduced to 4 non-zero and independent elements:

$$\chi_1 = \chi_{zzz} \qquad \chi_3 = \chi_{xzx} = \chi_{yzy} = \chi_{xxz} = \chi_{yyz} \qquad \textbf{Equations 2.43}$$

$$\chi_2 = \chi_{zxx} = \chi_{zyy} \qquad \chi_4 = \chi_{xyz} = -\chi_{yxz} = \chi_{xzy} = -\chi_{yzx}$$

For achiral molecules, χ_4 elements vanish, as there is an infinite number of mirror planes of symmetry perpendicular to the surface. For chiral molecular surfaces, mirror planes of symmetry do not exist and χ_1, χ_2 and χ_3 are the achiral elements, while χ_4 is the chiral element.

χ_4 is non-zero either for bulk chiral materials, or surfaces of chiral molecules. It changes sign upon going from one enantiomer to the other. The 27 elements of $\vec{\alpha}^{(2)}$,which are symmetry-allowed for SHG, vary with frequency and for different molecules.

With various combinations of input and output beam polarisations, the independent non-vanishing elements of $\vec{\chi}^{(2)}$ can be deduced from SHG experiments. In special cases, this also allows the average molecular orientation to be determined.

If a molecule has a well defined long molecular axis, its hyperpolarisability tensor $\vec{\alpha}^{(2)}$ is dominated by the tensor element $\alpha^{(2)}_{z'z'z'}$ with z' along the molecular axis;

$\alpha^{(2)}_{z'z'z'}$ can be related to the elements of $\vec{\vec{\chi}}^{(2)}$ in the laboratory co-ordinates (x,y,z) by a co-ordinate transformation. If θ is the angle between z' and the surface normal z and the molecules have a random azimuthal distribution (Equations 2.44)

$$\chi^{(2)}_{zzz} = N\alpha^{(2)}_{z'z'z'}\left\langle \cos^3\theta \right\rangle$$
$$\chi^{(2)}_{zxx} = \chi^{(2)}_{zyy} = (1/2)N\alpha^{(2)}_{z'z'z'}\left\langle \sin^2\theta\cos\theta \right\rangle$$

Equations 2.44

where N is the surface density of the molecules and the angular brackets refer to an orientational average. From equations 2.44 the measurements of $\chi^{(2)}_{zzz}$ and $\chi^{(2)}_{zxx}$ allow the deduction of both $\alpha^{(2)}_{z'z'z'}$ and θ.

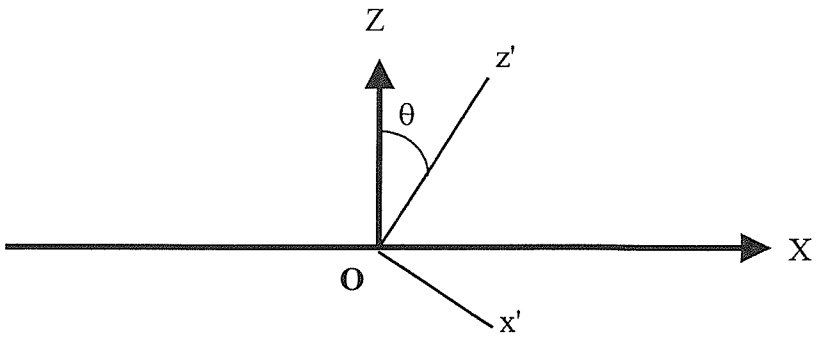

Figure 2.10 Orientation of a Rod - like Molecule at an Interface. The molecular axes x'y'z' can be related to the laboratory axes XYZ by the Eulerian angles. Oz' represents the dipole moment of the molecule and Z is the surface normal.

$$I_s = \left| a_1\chi_{xxz}\sin 2\alpha + a_6\chi_{xyz}e^{i\delta}\cos^2\gamma \right|^2$$

Equations 2.45

$$I_p = \left| e^{2i\delta}(a_2\chi_{xxz} + a_3\chi_{zxx} + a_4\chi_{zzz}) + a_5\chi_{zxx}\sin 2\gamma - a_7\chi_{xyz}e^{i\delta}\sin 2\gamma \right|^2$$

With,

$$a_1 = e_y(\omega)e_z(\omega)e_y(2\omega)$$
$$a_2 = 2e_x(\omega)e_z(\omega)e_x(2\omega)$$
$$a_3 = e_x{}^2(\omega)e_z(2\omega)$$
$$a_4 = e_z{}^2(\omega)e_z(2\omega) \qquad \textbf{Equations 2.46}$$
$$a_5 = e_y{}^2(\omega)e_z(2\omega)$$
$$a_6 = 2e_x(\omega)e_z(\omega)e_y(2\omega)$$
$$a_7 = e_y(\omega)e_z(\omega)e_x(2\omega)$$

$e_x(\omega)$, $e_y(\omega)$, $e_x(2\omega)$, $e_y(2\omega)$ are all independent of the refractive index of the surface layer, which is given by $n_3(\omega)$ and $n_3(2\omega)$ at the fundamental and second harmonic wavelengths respectively.

$$e_z(\omega) \propto \frac{1}{n_3(\omega)^2}$$
$$e_z(2\omega) \propto \frac{1}{n_3(2\omega)^2} \qquad \textbf{Equations 2.47}$$

I_s and I_p are related to ψ through E_s and E_p by the following equations:

$$Is = |E_s|^2 \qquad Ip = |E_p|^2 \qquad \textbf{Equations 2.48}$$

Giving

$$\tan\psi = |E_p|/|E_s| \qquad \textbf{Equation 2.49}$$

or,

$$\tan^2\psi = I_p/I_s \qquad \textbf{Equation 2.50}$$

2.4 References

2.1 F. A. Jenkins and H.E. White, *Fundamentals of Optics* (4th Edition), McGraw-Hill, New York (1981).

2.2 M. Born and B. Wolf, *Principles of Optics* (4th edition), Pergamon Press, New York (1969).

2.3 *Handbook of Chemistry and Physics* (72nd edition) Chemical Rubber Company Press (1991-92).

2.4 W. A. Shurcliff and S. S. Ballard, *Polarised Light*, Van Nostrand Co.Inc, Princeton, New Jersey (1964).

2.5 R. M. A. Azzam and N. M. Bashara, *Ellipsometry and Polarised Light*, North Holland Publishing Co., Amsterdam (1977).

2.6 R.C. Jones, *J. Opt. Soc. Am.*, **31,** (1941) 488.

2.7 A.N. Saxena, *J. Opt. Soc. Am.*, **55**, (1965) 1061.

2.8 L. T. Cheng, W. Tam, S. H. Stevenson, G. R. Meredith, G. Rikken and S. R. Marder, *J. Phys. Chem.* **95** (1991) 10631.

2.9 J.A. Armstrong, N. Bloembergen, J. Ducuing and P.s. Pershan, *Phys. Rev.* **127** (1962) 1918.

2.10 J.F Ward and P.A. Franken, *Phys. Rev.*, **143** (1964) 183A.

2.11 T. F. Heinz, *Non-linear Optics of Surfaces and Adsorbates,* thesis, Department of Physics, University of California, Berkeley (1982).

2.12 V. Mizrahi and J. E. Sipe, *J. Opt. Soc. Am. B* **5** (1988) 660.

Chapter 3

EXPERIMENTAL

3.1 Surface Tension

Measurements were made using a type 'OS' surface and interfacial tension torsion balance, which was used in conjunction with a 4cm-circumference platinum ring.

The balance was set up and levelled by means of a spirit level on a firm, flat surface. The extension hook was attached to the beam and the platinum ring, which was cleaned in a roaring Bunsen flame, was connected to the extension hook.

A clean teflon petri-dish was filled to about two thirds level with the liquid under investigation and placed on the platform which was raised until the surface of the liquid was about 1cm below the platinum ring. The platform was slowly raised until the ring just touched the surface of the liquid. The surface was gradually lowered until the ring parted from the surface of the liquid and the surface tension was measured in Nm^{-1}.

3.2 UV Spectroscopy

A wavelength scan in the range 400-700nm was carried out for 0.2, 1, 2, 5, 10 and 20μM solutions of Rhodamine 6G. The samples were placed in a 1cm quartz cell and examined by a UV Spectrometer (Unicam UV1)

3.3 Ellipsometry

3.3.1 The Optical Train

A typical experimental set-up begins with a light source, either a laser (Helium- Neon) at a fixed wavelength or a UV enhanced 75W Xenon arc lamp (Illumination Industries Inc, model LH351Q), used in conjunction with a monochromator.

A polariser will be used to convert unpolarised to polarised light, by only transmitting light of a certain polarisation, which is aligned with its polarising axis. If the angle of polarisation of the wave is not aligned with the axis, it can be split into components parallel to and perpendicular to the axis. The component parallel to the axis is then

transmitted. By convention, the angle P, from the plane of incidence to the transmission axis of the polariser, is the clockwise angle from the vertical when the observer looks along the direction of propagation. The polariser is a high quality, low power, Glan-Thompson prism (Karl Lambrecht) which consists of two triangular prisms (each with an apex angle of about 38.5°), cemented together along the hypotenuse faces.

The sample is either

a) a clean bare surface with a small horizontal polished area, which reflects the incident light specularly (e.g. quartz),
b) a thin film on a glass surface (in this case Rhodamine 6G - (R6G)), or
c) a solution of a partly hydrophobic molecule (again R6G) in water, which approximates to a thin film on a water substrate.

A quarter wave plate or retarder is held in a mount so that its face is perpendicular to the direction of travel of the reflected beam. The angle Q, from the plane of incidence to the fast axis of the QWP is measured in the same sense as P. The QWP's only function is to introduce a relative phase change of 90° between two perpendicular linear components of the light. It can be placed before or after the sample; in this experiment, it is before.

An analysing polariser (Analyser) (Ref. 3.1), a second Glan-Thompson prism, is used to determine the angle of polarisation of the reflected light. The fixed analysing angle, A, is measured in an identical fashion to P. The detected light intensity is plotted vs the angle Q and with the angle A as a reference.

The light passes through a monochromator (Applied Photophysics) which has a bandwidth of $\pm$2nm at 320nm. A photomultiplier tube (red enhanced side looking tube-Hamamatsu) will detect the intensity of the light collect the data and transfer it to a personal computer for analysis.

3.3.2 Alignment

With the arms of the ellipsometer horizontal, the light was directed through a series of high-quality fused silica lenses and mirrors to the input arm of the ellipsometer. Two mirrors were adjusted so that the beam passed through the optical train to the detector.

The correctness of the alignment was confirmed when the arms were raised to the required angle of incidence, and the beam reflected by a flat sample, through the output optics to the detector. As no adjustments were necessary, calibration measurements could then be performed and compared with literature values to ensure the accuracy of the optics (see Section 2.4).

3.3.3 Calibration

With the ellipsometer's arms horizontal, the polariser and analyser were fixed with the optimum values for A and P being determined by a nulling technique. A, Q and P are adjusted until the intensity of light reaching the detector is zero. P is set at 45° and A and Q are adjusted to the nulling positions and A is fixed at 0°. This ensures that the s and p components of the incident light are identical. Any variation in the detected s and p components will be due to the surface and not the incident light.

In the actual experiments, the quarter wave plate is rotated in steps of 3.6° and the signal averaged over 100 points by the acquisition program "e" (R. Greef). Δ and ψ are calculated from this data.

3.4 Second Harmonic Generation

For SHG experiments the apparatus shown schematically in Figure 3.1 is used.

The light source is a pulsed Neodynium :YAG (Continuum; model 661-10) pumped dye laser (Continuum; model TDL60). The YAG produces frequency doubled 532nm radiation, of intensity ~250mJ per pulse, at 10Hz, with a beam diameter of about 1cm. Rhodamine 6G laser dye produced tuneable radiation in the range 556 to 580nm. For the work on quartz, DCM laser dye was also used and a fundamental wavelength of 640nm was selected. After exiting the dye laser, the beam diameter is 5mm and its intensity of the order of 20mJ per pulse. The beam is reflected off a series of 45° mirrors to reach the optical train. At mirror * in Figure 3.1 some radiation is transmitted and its intensity recorded by a photodiode as a measure of the beam intensity before it enters the optical train at the top of the ellipsometer. Except where specified, the ellipsometer arms were set at a constant angle (70°) to the surface normal.

The double Fresnel rhomb is used for power attenuation. It rotates the polarised laser beam to an orientation, which permits suitable transmission through the polariser. The polariser and the analyser are set at suitable fixed azimuths. A Schott glass UV filter (Ealing GG-495) is placed after the polariser to ensure that all UV light reaching the detector comes from the sample. At this point the intensity of fundamental radiation can be measured by inserting a Gentec power meter. The beam is focussed onto the surface in question using a 20cm-focussing lens. After reflection from the surface, two visible, Schott glass filters (EALING UG5) absorb the fundamental beam. The second harmonic beam is recollimated with a 20cm focal length lens and transmitted through a series of irises to the polariser. After transmission through the analyser, the beam is focussed by a 5cm focal length lens, through a third UG5 filter into a 300μm slit at the entrance to the monochromator. The monochromator transmits light at the second harmonic wavelength. The light exits the monochromator through a second 1mm slit and enters the detection system. This consists of a photomultiplier tube (Thorn EMI; model 9828B with housing; QL30F/RFI), a pulse amplifier (Thorn EMI; model A2) and a gated integrator and boxcar averager (Stanford Research Systems; model SR250).

Before measurements commenced, a CG495 filter was inserted in front of the monochromator to block all second harmonic light. This proved that any second harmonic detected was generated by the sample. Furthermore, the monochromator wavelength was moved away from the second harmonic, to check that the intensity returned to zero. This proved that two-photon fluorescence was not contributing to the intensity.

The data was acquired and processed by a Pentium 90 PC using a Visual Basic program (R. Greef and R.D. Spencer-Smith). Sets of 100 data points were recorded and averaged for each of four measurements (SHG intensity, intensity background, laser beam intensity and its background). The backgrounds were subtracted and the adjusted SHG and laser beam intensities saved.

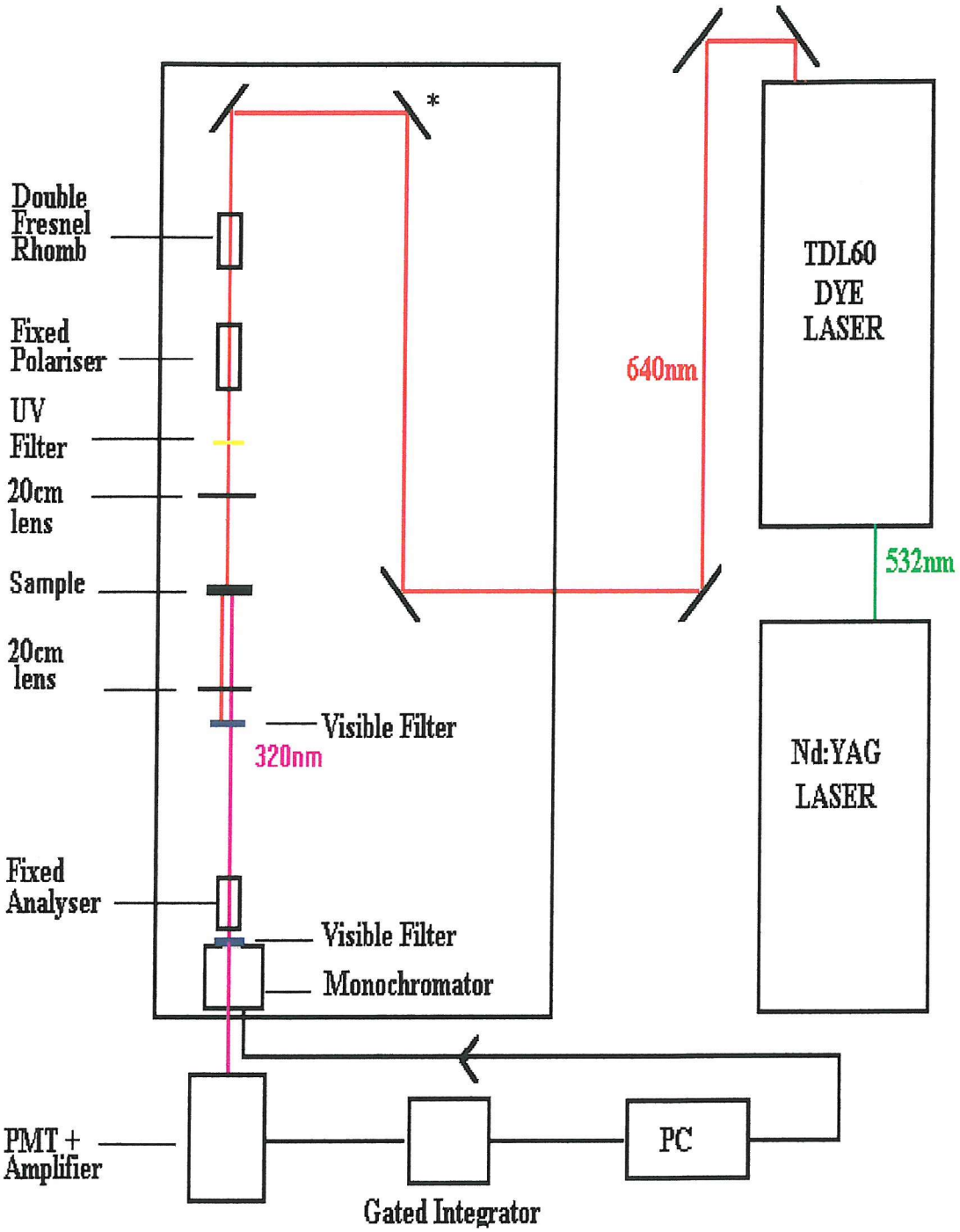

Figure 3.1 **Schematic Plan of the Laboratory Experimental Arrangement for SHG. For SHE, the only change is the insertion of the Quarter Wave Plate on the output arm between the visible filter and the analyser.**

For SHG-CD measurements a Soleil-Babinet compensator was used to produce left and right circularly polarised light. It was calibrated by inserting it between the polariser and the compensator in the optical train shown in Figure 2.5. A measurement was recorded with the monochromator adjusted to a desired fundamental wavelength. The light intensities were recorded for 100 data points at each of 100 QWP angles and the ellipsometric parameters Δ and ψ were calculated in the normal way. The Soleil-Babinet compensator was then adjusted and measurements repeated until satisfactory values of Δ and ψ were recorded in three successive runs for each of the desired input polarisations. These values are shown in Table 3.1. The reading of the compensator was recorded and it was reset to these values for the appropriate run. This procedure was repeated for each of the desired wavelengths.

Polarisation	ψ/°	Δ/°
45° Linear polarised	45 ± 0.5	0 ± 0.5
Right Circular Polarised	45 ± 0.5	90 ± 0.5
-45° linear polarised	45 ± 0.5	180 ± 0.5
Left Circularly polarised	45 ± 0.5	270 ± 0.5

Table 3.1 Values of Δ and ψ for each of the Desired Input Polarisations.

3.5 Calibration

Using the Xenon arc lamp a wavelength scan of the (100) surface of a hyper-pure silicon wafer (Wacker-Chemitronic GMBH) was carried out in the region 250-320nm. The values were compared to those obtained by (Greef et al Ref. 3.3) and gave excellent agreement. This showed that all of the components of the optical train were working satisfactorily.

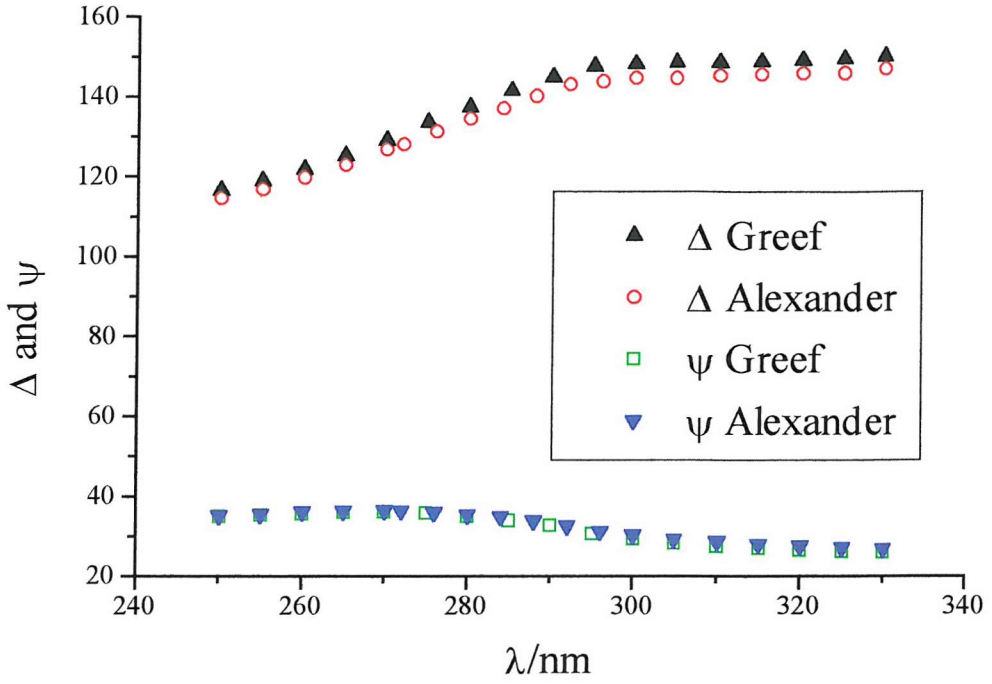

Figure 3.2 **Plots of Δ and ψ Vs Wavelength for a polished (100) Silicon Surface, including a Comparison with Data from the Literature (Ref. 3.3).**

To ensure that the same components worked with the laser, ellipsometric measurements on water and gold were performed using the pulsed ND YAG laser which was to be used for SHE experiments. These provided excellent agreement with literature values (Refs. 3.2-3.3). At 564nm, water has $\Delta = 359.58°$ and $\psi = 24.07°$, and for gold, $\psi = 43.59°$ and $\Delta = 104.61°$. These confirmed that the calibration was correct for both lamp and laser.

3.6 Sample Preparation

All glassware used in liquid sample preparation was cleaned using the following method. The glassware was soaked in a soap solution for one hour, or preferably overnight. It was then rinsed using deionised water (Purite, > 17.5MΩcm^{-1}), which was also filtered for organic impurities. The glassware was then washed in 2M nitric acid and, finally in liberal amounts of deionised water and left to dry.

The quartz samples used were in cut crystal form and were cleaned with lens cleaning tissue and methanol (which removed fingerprints and other UV absorbing grease), and then water. They were regularly sprayed with compressed air to prevent dust particles from settling on the surface.

The R6G was dissolved to the desired concentration in deionised water and added to a clean petri-dish. For the solid film, a drop was placed on a clean microscope slide and the water left to evaporate.

Boc-Trp-Trp was dissolved in 0.2M sodium hydroxide solution and then neutralised with an equal volume of 0.2M hydrochloric acid solution. 10% of the volume of this solution was removed and replaced with an equivalent volume of HCl solution to give a sample at pH 2.

3.7 Sample Environments

3.7.1 Quartz

For transmission experiments, the crystal was mounted on a rotating stage with its surface perpendicular to the beam. The stage was attached to four Microbench (Halbo Optics) rods. Two 1mm irises (Halbo Optics) were mounted at the ends of the rods before and after the beam for alignment purposes. An arbitrary mechanical angle was chosen as zero and measurements were made at equal intervals as the stage was rotated manually.

For reflection experiments, the crystal was mounted on a stepper-motor-controlled turntable and held in position by teflon bars as shown in Figure 3.3. This in turn was mounted on a tilt rotation stage (Newport), the surface of which had previously already set as horizontal using a spirit level. The stepper motor rotation was controlled by an accompanying software package (Scope).

3.7.2 Liquids

These were placed in a glass cell shown in Figure 3.4. They were maintained at constant temperature by a flowing water supply. The lid was designed to minimise the possibility of dust particles settling on the surface. A flowing 0.5 bar supply of nitrogen prevented oxidation of the sample.

The cell was placed on a two-dimensional translation stage, which could be adjusted so that the beam struck the surface at the axis of the ellipsometer.

All measurements were conducted in the dark in order to minimise any extraneous light reaching the detector. Fundamental beam intensity was limited to a maximum of 4mJ per pulse to eliminate any photochemical reactions at the surface.

Difficulties to be overcome in the study of liquid surfaces include the reduction in the second harmonic emitted and, most relevantly, the sensitivity to vibration. A building site within 10 metres of the lab, with heavy drilling and heavy vehicles loading and unloading regularly, seriously disrupted experiments. In addition to the slamming of doors within the building, the only way to minimise vibration was to work overnight. The disturbance caused by any motion of the operator in the lab was damped by the presence of several sheets of thick foam mat interspersed with wooden blocks placed underneath the sample stage. The remote operation of the computer-driven measuring system meant that the sample had time to settle (after any adjustments in wavelength, alignment) before measurements began.

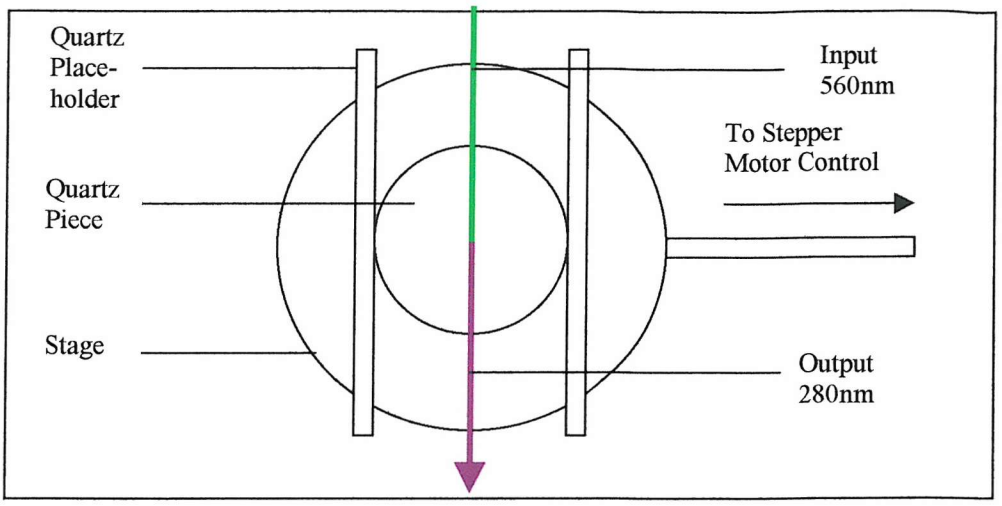

Figure 3.3 Plan view of Quartz Environment for Reflection Experiments.

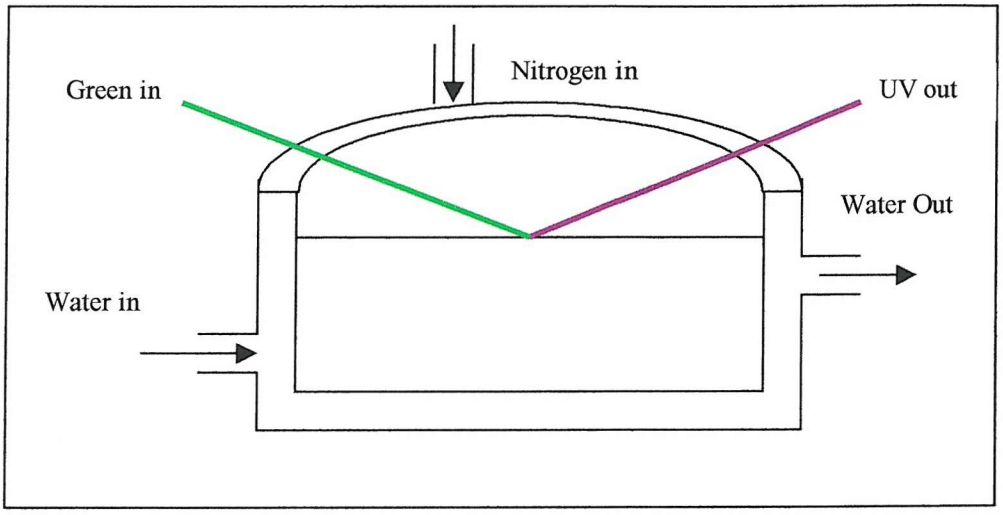

Figure 3.4 Liquid Sample Environment

3.8 Second Harmonic Ellipsometry

The apparatus was exactly the same as for SHG (Figure 3.1) with the exception that the quarter wave plate was inserted on the output arm between the visible filter and the analyser.

For quartz, the intensity measurements were taken by the same method except that the 400 data points were averaged for each of 100 quarter wave plate angles, taken at 3.6° intervals. The background intensities were subtracted to give one SHG intensity for

each QWP angle and these intensities were then subjected to ellipsometric analysis to calculate Δ and ψ.

For liquid samples, the measurements were modified slightly. Instead of one revolution of 100 data points (10 minutes for one revolution), the quarter wave plate was rotated n times ($10<n<40$) measuring 10 data points at each angle. Because the quartz sample was extremely stable in the conditions and it gave a very high second harmonic signal, the signal to noise ratio was excellent and the length of time to measure did not affect the results. With liquid samples, however, the signal to noise ratio was much poorer and a random event such as a door slamming would have less of a drastic effect on one measurement.

It also had the advantage that a run could be stopped after fewer than 40 QWP revolutions if the results were of high enough quality.

3.9 Examples of SHE Experiments

3.9.1 Quartz

A typical file for Y-cut quartz gave the graph in Figure 3.5. The AAAA peak pattern is distinctive of linearly polarised light. As the circular component of the polarisation increases, this will become an ABAB peak pattern (e.g. Figure 3.6). The B peaks disappear completely for circularly polarised light, giving only a twofold AA pattern.

3.9.2 SHE From Water

The sensitivity of SHE can be illustrated by the observation of a significant circular polarisation component ($\Delta = 21.29 \pm 2°$) in the second harmonic generated from deionised water. An example with $\psi = 50.662°$ and $\Delta = 22.03°$ is shown in Figure 3.6. The ABAB pattern is more obvious when the peak minima are observed.

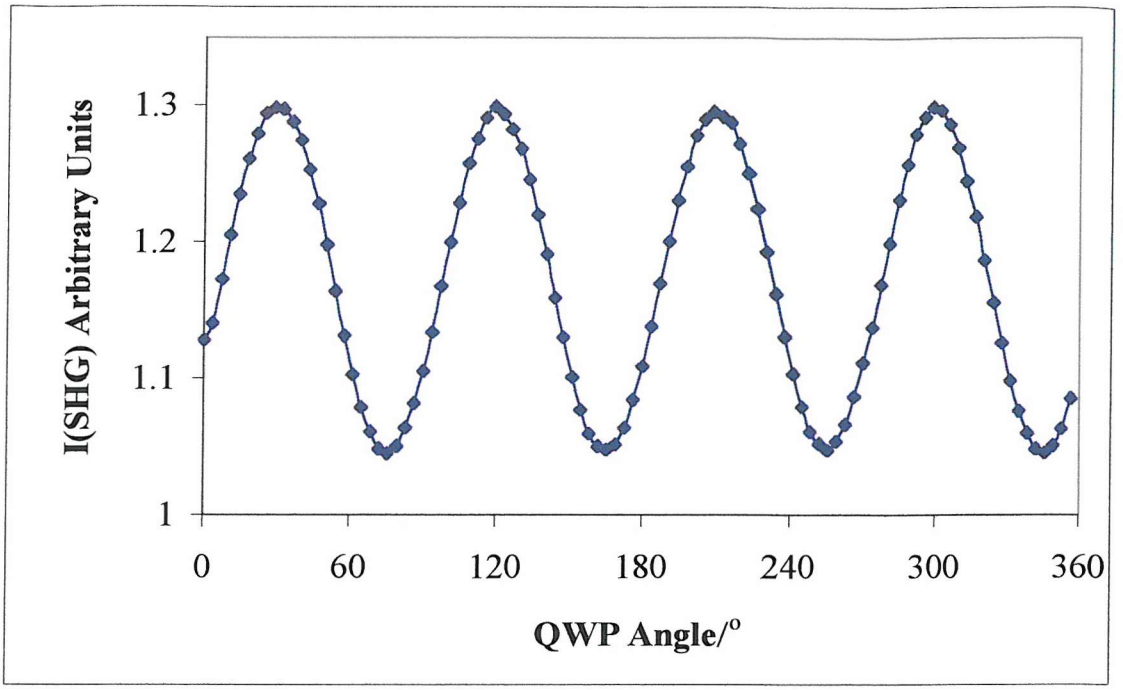

Figure 3.5 **Example of the Variation in SHG Intensity from a Y-Cut Quartz Piece as the Quarter Wave Plate was rotated in a SHE Experiment. This run gave values of Δ=0.538° and ψ= 44.386°.**

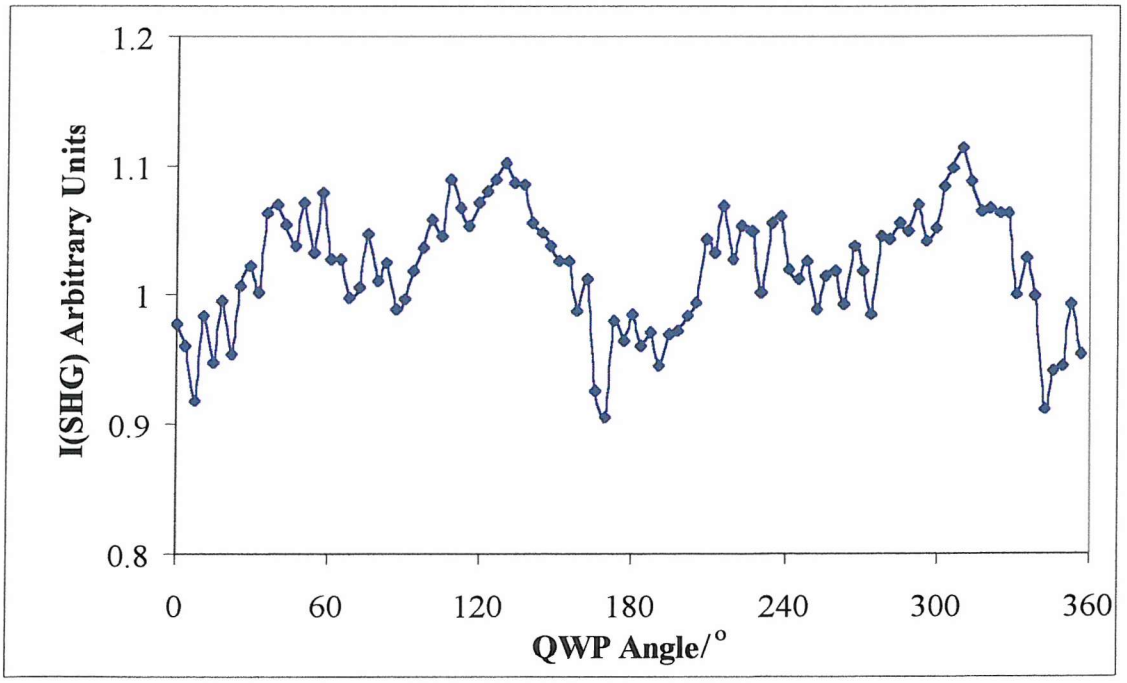

Figure 3.6 **Example of the Variation in SHG Intensity from Water as the QWP was rotated in a SHE Experiment. This run gave values of Δ = 22.03° and ψ = 50.66°**

The calibration experiments outlined in Section 3.5 were successfully repeated in order to confirm that the apparatus was working as expected. The surface tension of the water was measured, but the value of 72.0mNm^{-1} was normal for water. An organic impurity would be expected to lower the surface tension dramatically.

This non-zero value of Δ was eventually determined to be due to the presence of an unidentified organic impurity in the supplied water. Once the filters were replaced, Δ was measured at 0°. However, although the result with water was ultimately misleading, it demonstrated the improved sensitivity of SHE relative to surface tension.

3.10 References

3.1 W. Spottiswoode, *Polarisation of Light*, Macmillan & Co., London (1874).

3.2 I. Thormählen, J. Straub and U. Grigull, *J. Phys. Chem. Ref. Data*, **14**, No 4 (1985) 933-945.

3.3 R. Greef, D. E. Gray, N. J. Dartnell, J. Zhu, S. Lynch and G. M. Crean, *Thin Solid Films*, **233** No 1-2 (1992) 214-217.

Chapter Four

INVESTIGATION OF THE SURFACE AND BULK PROPERTIES OF QUARTZ

4.1 Quartz - An introduction

Quartz, along with cristobalite, is one of two forms of pure silicon dioxide, SiO_2. It has two principal structures known as α– and β– quartz. The transition temperature is 573°C, with the more symmetrical β– form being stable at higher temperatures. Quartz is found in natural crystals which need to be carefully oriented and cut or can be made synthetically. Both forms have their own advantages; natural quartz can be used to form larger crystals whereas synthetic ones may only grow to about 5mm thick. On the other hand, synthetic crystals may have transmission greater than 80% at wavelengths as low as 190nm as opposed to 220nm for the natural crystal (Ref. 4.1).

4.1.1 Optical Properties

This work is done with natural crystals of α- quartz which is a positive uniaxial crystal ($n_e > n_o$) with space group 3m. It is transparent in the range 160-3500nm (Ref. 4.2). The refractive index varies with wavelength as shown in Figure 4.1.

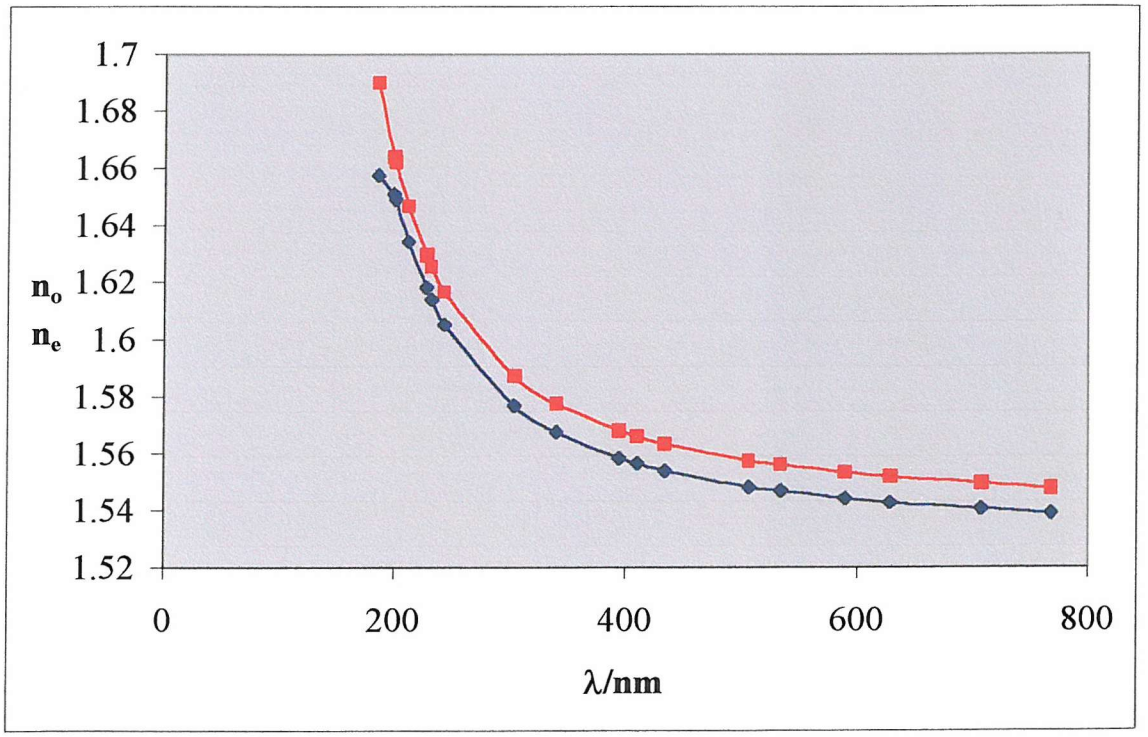

Figure 4.1 Refractive Index of Quartz (O-ray (blue curve) and E-Ray (red curve)) vs. Wavelength (Refs. 4.3-4.4)

Quartz is circularly birefringent, meaning that the ordinary and extraordinary refractive indices never converge as a function of wavelength. The optic axis (defined as the Z-axis) is therefore that for which the two refractive indices are closest in magnitude. The beam will propagate along the Z-axis as two circularly polarised rays of opposite handedness and the incident plane-polarised beam is rotated.

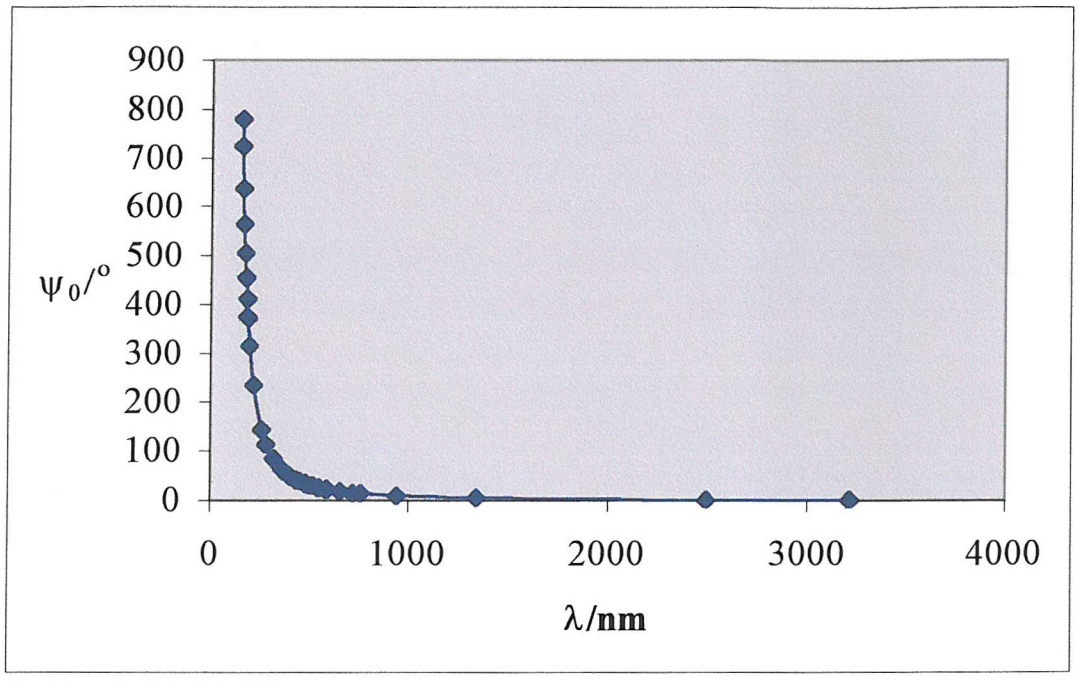

Figure 4.2 Optical Rotatory Power of Quartz expressed in degrees per mm thickness. (Refs. 4.3-4.4)

This work will start by trying to quantify this optical rotatory power.

4.1.2 Structure

At a first glance down the Z-axis of a structural diagram, quartz appears to consist of layers of Si_6O_6 'rings' interlocked with Si_3O_3 'rings'. However, upon closer examination, it can be seen that there are actually helical chains of $(SiO)_n$, with the $(n+1)^{th}$ Si atom appearing directly behind the first one, when viewed along the helical axis. This occurs due to the presence of screw axes, (axes where the structural unit is repeated every 1/n of a revolution, but is each time displaced by m/n of the repeating distance parallel to this axis) which are denoted n_m. The silicon atoms have a co-ordination number of four, with two co-ordinate oxygen atoms found at the vertices of

corner-sharing tetrahedra. As a result, it can be seen that parallel to this axis, quartz has two right handed 6_2 axes and one left handed 3_2 axis.

The co-ordinate system is usually defined in one of two ways:
(i) mutually perpendicular Cartesian (x,y,z) axes (as in the cut pieces in this work);
(ii) crystallographic axes as defined for a helical system ($a=b\neq c$, $\alpha=\beta=90°$ $\gamma=60°$).

Quartz can also be obtained in different 'cuts'. Of particular interest are those cut perpendicular to the Cartesian axes. These are called X- (cut in the YZ plane), Y- (cut in the XZ plane) and Z- (cut in the XY plane) cut quartz.

A further 2_1 axis is visible along the x axis (X-cut quartz). Because of its helical chains, quartz, unlike cristobalite, is chiral.

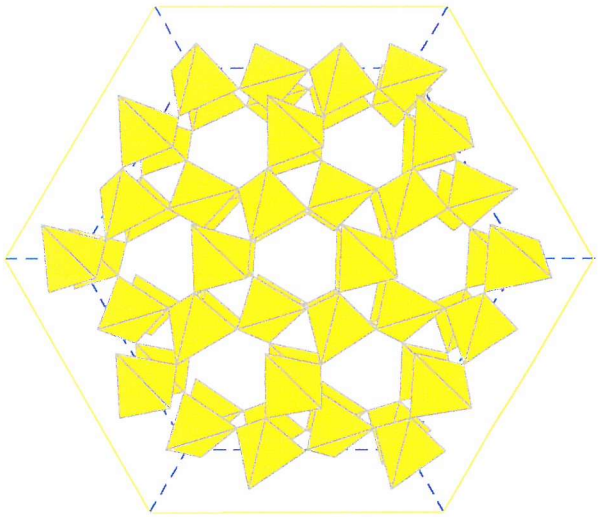

Figure 4.3 **Quartz, viewed along the optic (or Z-) axis. The tetrahedra represent the fragment SiO_4 (Si atoms at the centre and O atoms at the vertices) and are corner-sharing. White hexagons and triangles represent the 6_2 and 3_2 axes (Ref 4.1).**

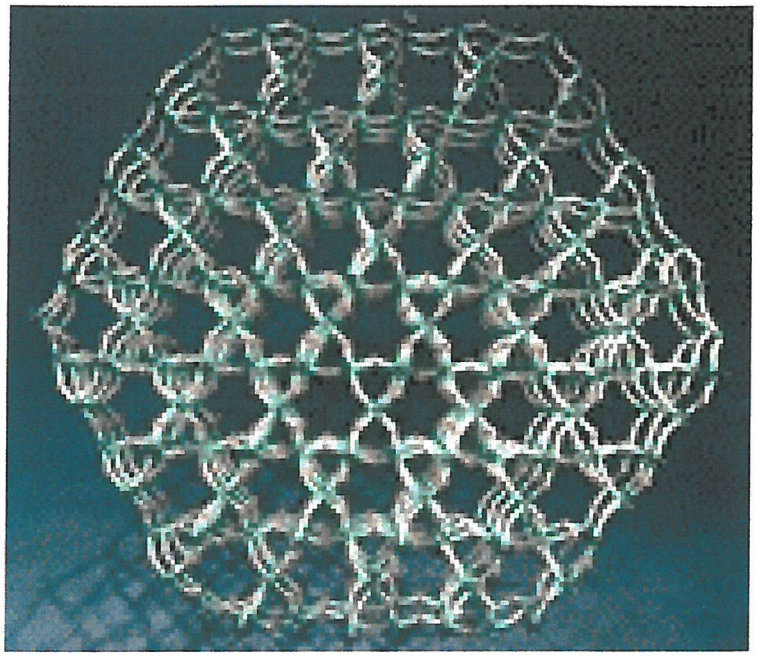

Figure 4.4 Model of Quartz viewed along the Optic (Z-) Axis (Ref 4.5).

4.2 Experimental

The apparatus and experimental methods used are exactly the same as those described in chapter 3.

4.3 Results and Discussion

4.3.1 Ellipsometry

4.3.1.1 Transmission at 632.8nm

As expected for polarimetry measurements of fused silica, no effect was observed. This is because of its disordered structure. The measurements for Z-cut quartz provided no variation as the quartz was rotated, due to the fact that the radiation passed along the optic axis of the material. However there was a constant optical rotation which was due to the spiral nature of the structure. This was related to the thickness of the material.

Cut	Δ/°	ψ/°
Thin Z-Cut: 1mm	359.883 ± 0.884 (2σ)	64.933 ± 0.081 (2σ)
Thick Z-Cut: 10mm	0 ± 3.3	54.39 ± 0.08
Fused Silica	0.125 ± 1.81 (2σ)	45.021 ± 0.042 (2σ)

Table 4.1 Δ and ψ Measurements for Z-Cut Quartz and Fused Silica

However, the X- and Y-Cut crystals, both cut in the plane of the optic axis showed variation in both Δ and ψ as the quartz flat was rotated. Figures 4.5 to 4.8 show that there is regular variation for both Δ and ψ.

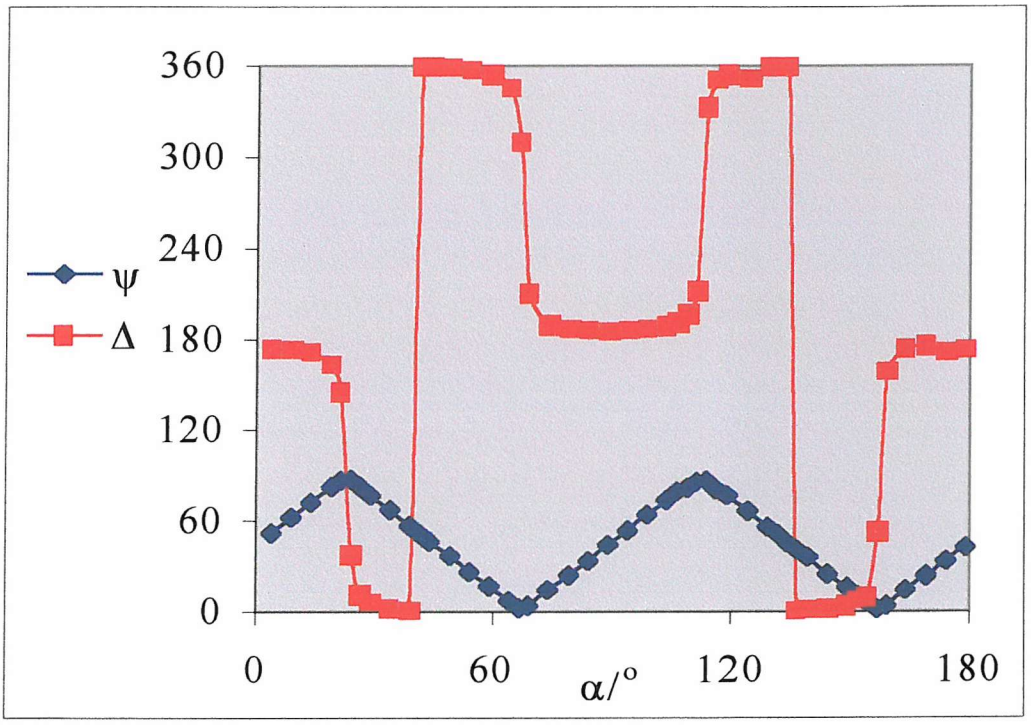

Figure 4.5 Transmission Ellipsometry from Y-Cut Quartz- 632.8nm, 45° Linear Polarised Input Radiation; Δ, ψ v Quartz Mechanical Angle α.

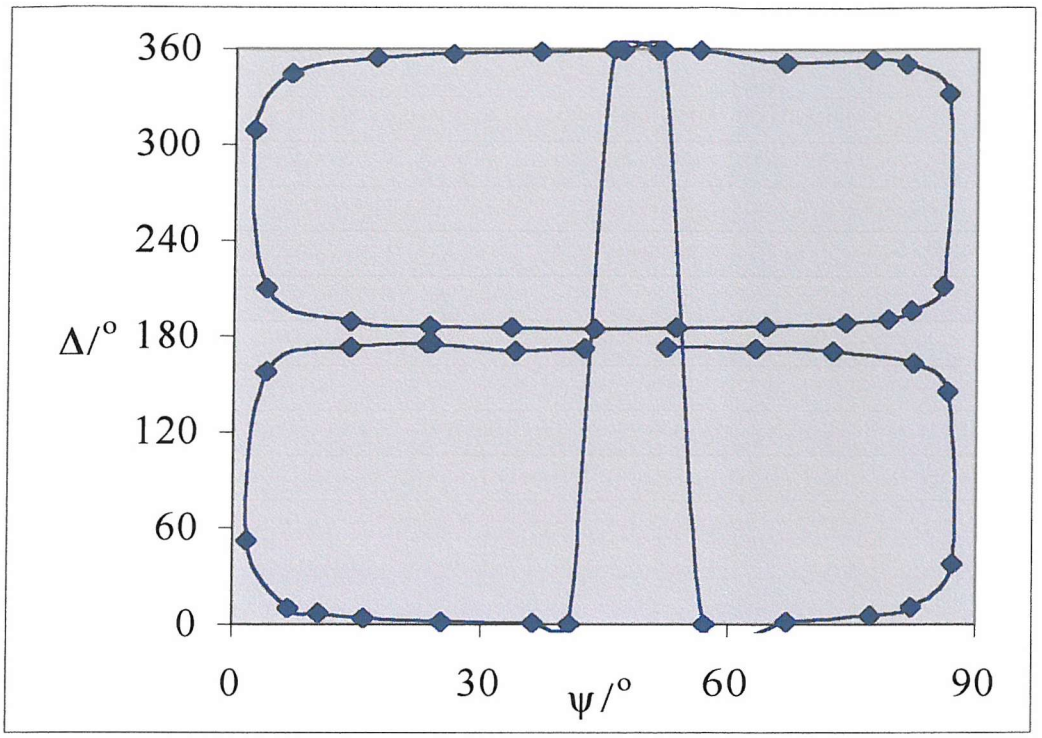

Figure 4.6 **Transmission Ellipsometry from Y-Cut Quartz - 632.8nm, 45° Linear Polarised Input Radiation: Δ vs ψ.**

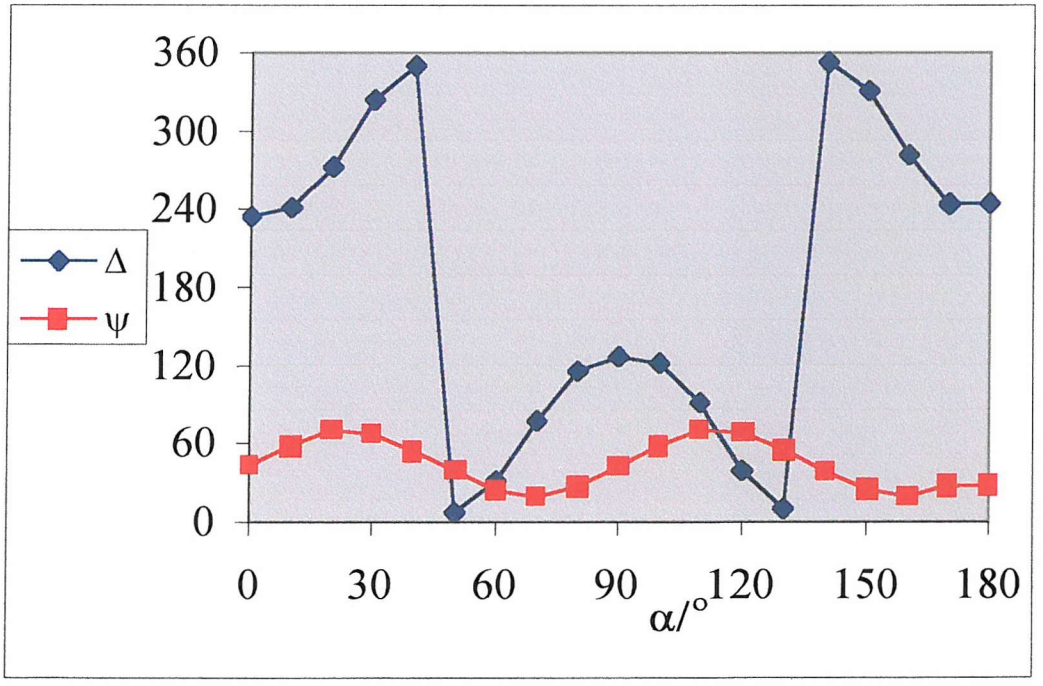

Figure 4.7 **Transmission Ellipsometry from X-Cut Quartz - 632.8nm, 45° Linear Polarised Input Radiation: Δ, ψ vs Quartz Mechanical Angle α.**

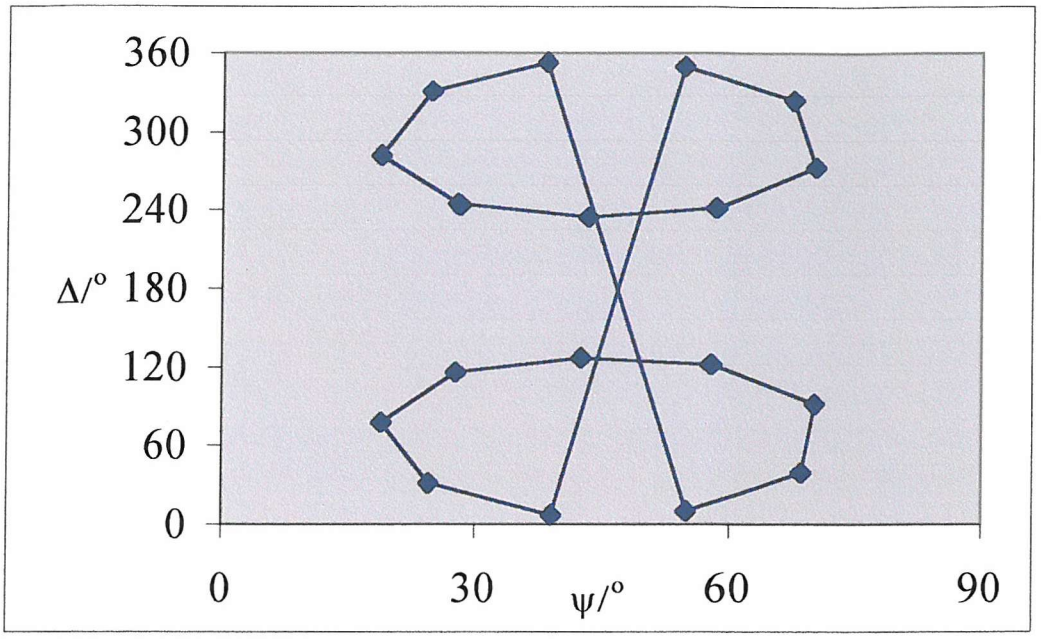

Figure 4.8 Transmission Ellipsometry from X-Cut Quartz - 632.8nm, 45° Linear Polarised Input Radiation: Δ vs ψ

In both cases, the graphs could not be fitted using normal spreadsheet software. However, they could be simulated using a Mathcad template (R. Greef) and the results are displayed in boxes 4.1 and 4.2. The simulation calculates ψ and Δ for each value of t_k, which represents the mechanical angle α. The source radiation (45° linear polarised) is described in terms of a 2x1 matrix, and this is multiplied by the matrix for the quartz plate ($Quartz_k$). The two variables, Δ_{qu} and ψ_{qu}, are properties of the quartz plate and estimates are given in table 4.2 below:

Cut	ψ_{qu}	Δ_{qu}	Rotation
X	90	$\pi/1.30 \pm 0.02$	Anticlockwise
Y	90	$\pi/1.05 \pm 0.02$	Anticlockwise

Table 4.2 Parameters for fits in boxes 4.1 and 4.2: Transmission Ellipsometry from X- and Y-cut Quartz at 632.8nm.

Finally ρ_k and then ps_k (ψ) and $delpos_k$ (Δ where $0° < \Delta < 360°$) are calculated and presented in graphs in the boxes on the following pages.

Box 4.1 10mm thick X-Cut Quartz Plate, 45° Linear Polarisation Incident.

Define number of points and theta interval for computation

$i := \sqrt{-1}$ $n := 99$ $k := 0..n$ $t_k := \frac{\pi}{n+1} \cdot k$

Define characteristics of quartz plate. Delta will be proportional to thickness.

$\psi_{qu} := \frac{\pi}{4}$ $\Delta_{qu} := \frac{\pi}{-1.3}$ $\rho_{qu} := \tan(\psi_{qu}) \cdot e^{\Delta_{qu} \cdot i}$

Define rotation matrix, and vector of incident light source$_4$ (linearly polarised, 45° azimuth.) Note that as rotation is anti-clockwise, the rotation matrix is

$S(\alpha) := \begin{pmatrix} \cos(\alpha) & -\sin(\alpha) \\ \sin(\alpha) & \cos(\alpha) \end{pmatrix}$ $\psi_4 := \frac{\pi}{4}$ $\Delta_4 := 0$ $source4 := \begin{pmatrix} \cos(\psi_4) \\ \sin(\psi_4) \cdot e^{i \cdot \Delta_4} \end{pmatrix}$

$Quartz_k$ is the matrix for the plate at an arbitrary angle k. vec_k is the vector of the outgoing light.

$Quartz_k := S(-t_k) \cdot \begin{pmatrix} 1 & 0 \\ 0 & \rho_{qu} \end{pmatrix} \cdot S(t_k)$ $vec_k := Quartz_k \cdot source4$ $rho_k := \frac{(vec_k)_1}{(vec_k)_0}$

$ps_k := atan(|rho_k|)$ $del_k := arg(rho_k)$ $delpos_k := if(del_k < 0, del_k + 2 \cdot \pi, del_k)$

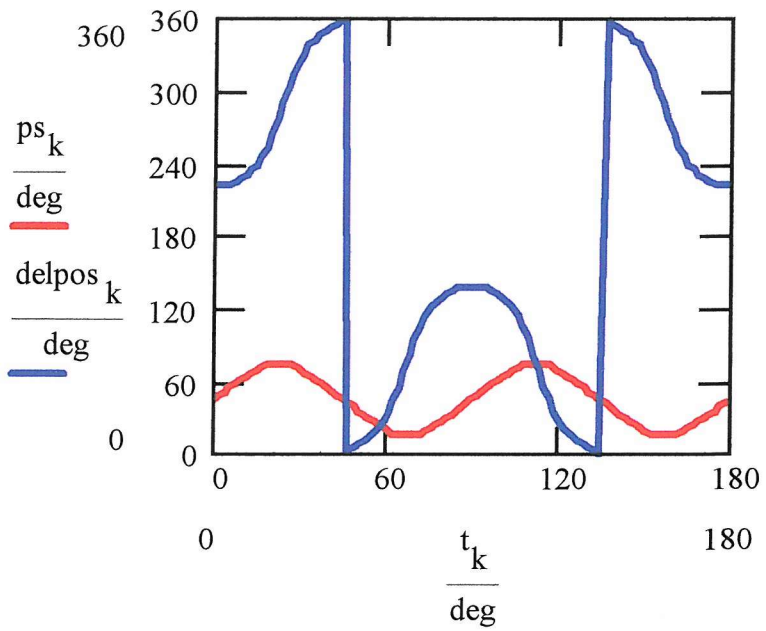

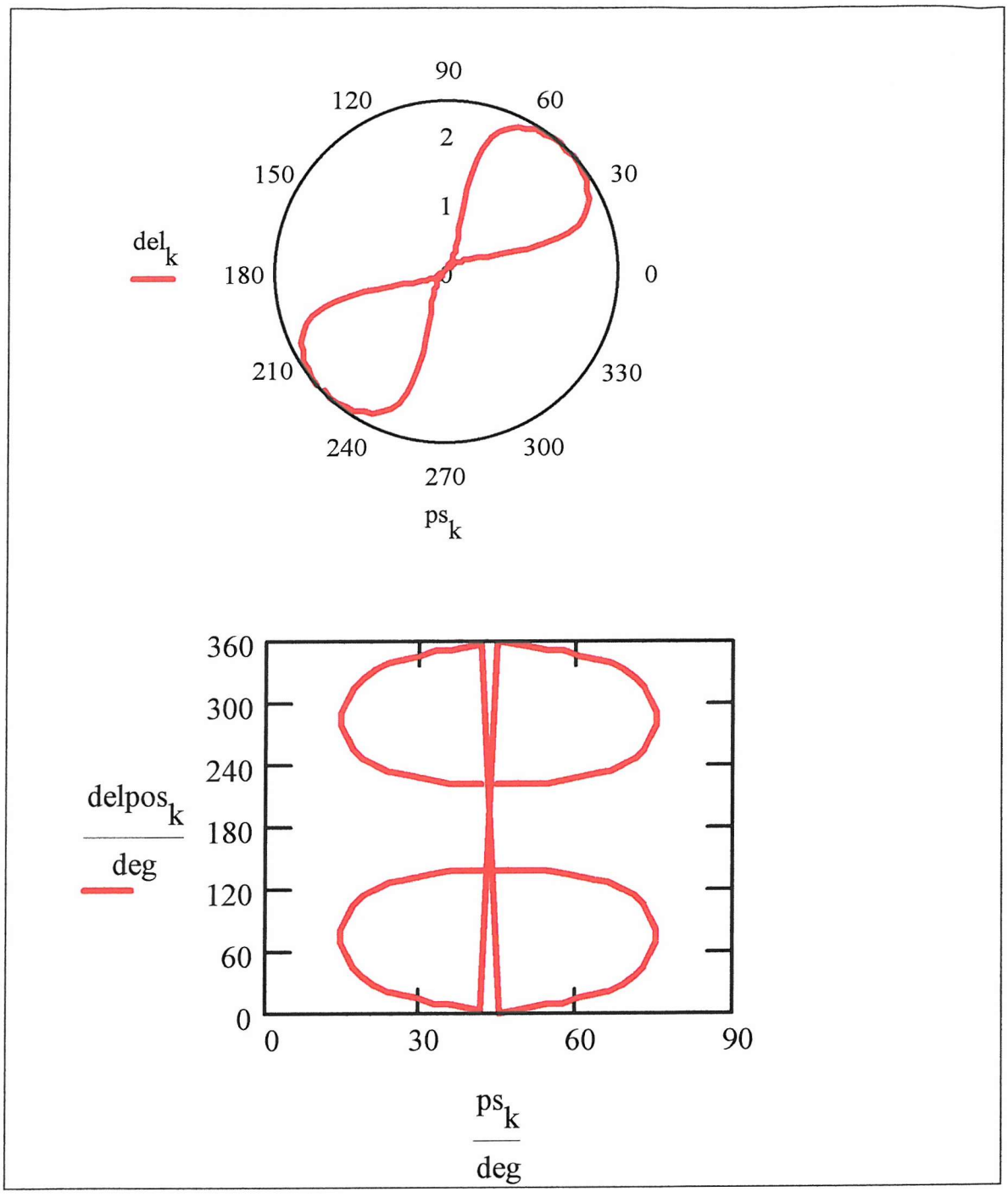

Pages 61-62
Box 4.1 **Mathcad Worksheet for X-Cut Quartz (R.Greef), including graphs:**

4.1.1 Polar graph of Δ vs ψ

4.1.2 Graph of Δ and ψ vs α

4.1.3 Graph of Δ vs ψ

Box 4.2 10mm thick Y-Cut Quartz Plate, 45⁰ Polarisation Incident.

Define number of points and theta interval for computation

$i := \sqrt{-1}$ $n := 99$ $k := 0..n$ $t_k := \frac{\pi}{n+1} \cdot k$

Define characteristics of quartz plate. Delta will be proportional to thickness.

$\psi_{qu} := \frac{\pi}{4}$ $\Delta_{qu} := \frac{\pi}{1.05}$ $\rho_{qu} := \tan(\psi_{qu}) \cdot e^{\Delta_{qu} \cdot i}$

Define rotation matrix, and vector of incident light source$_4$ (linearly polarised, 45° azimuth.) Note that as rotation is anti-clockwise, the rotation matrix is

$S(\alpha) := \begin{pmatrix} \cos(\alpha) & -\sin(\alpha) \\ \sin(\alpha) & \cos(\alpha) \end{pmatrix}$ $\psi_4 := \frac{\pi}{4}$ $\Delta_4 := 0$ $source4 := \begin{pmatrix} \cos(\psi_4) \\ \sin(\psi_4) \cdot e^{i \cdot \Delta_4} \end{pmatrix}$

$Quartz_k$ is the matrix for the plate at an arbitrary angle k; vec_k is the vector of the out-going light.

$Quartz_k := S(-t_k) \cdot \begin{pmatrix} 1 & 0 \\ 0 & \rho_{qu} \end{pmatrix} \cdot S(t_k)$ $vec_k := Quartz_k \cdot source4$ $rho_k := \frac{(vec_k)_1}{(vec_k)_0}$

$ps_k := atan(|rho_k|)$ $del_k := arg(rho_k)$ $delpos_k := if(del_k < 0, del_k + 2 \cdot \pi, del_k)$

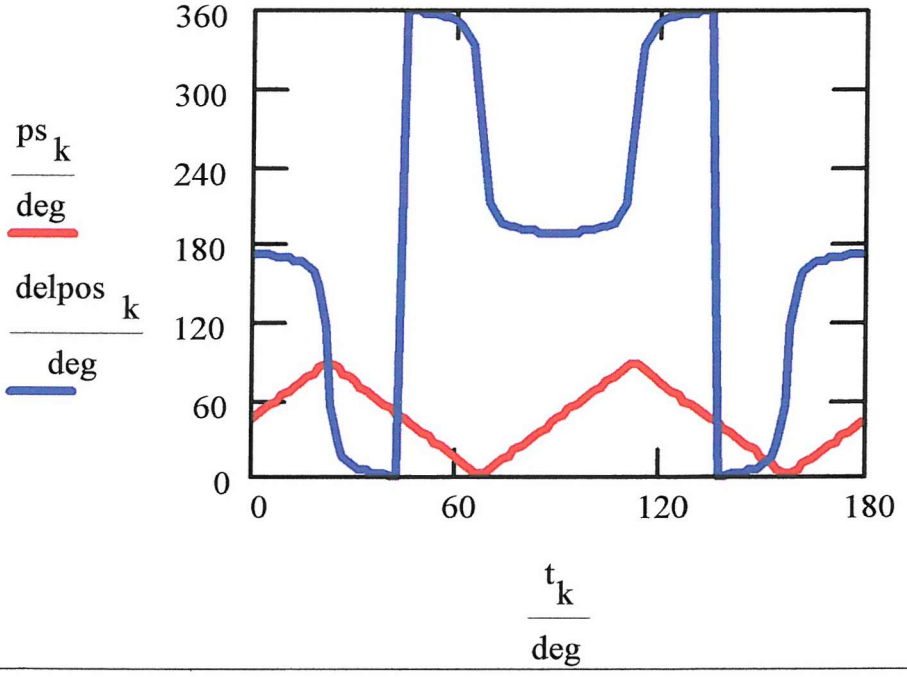

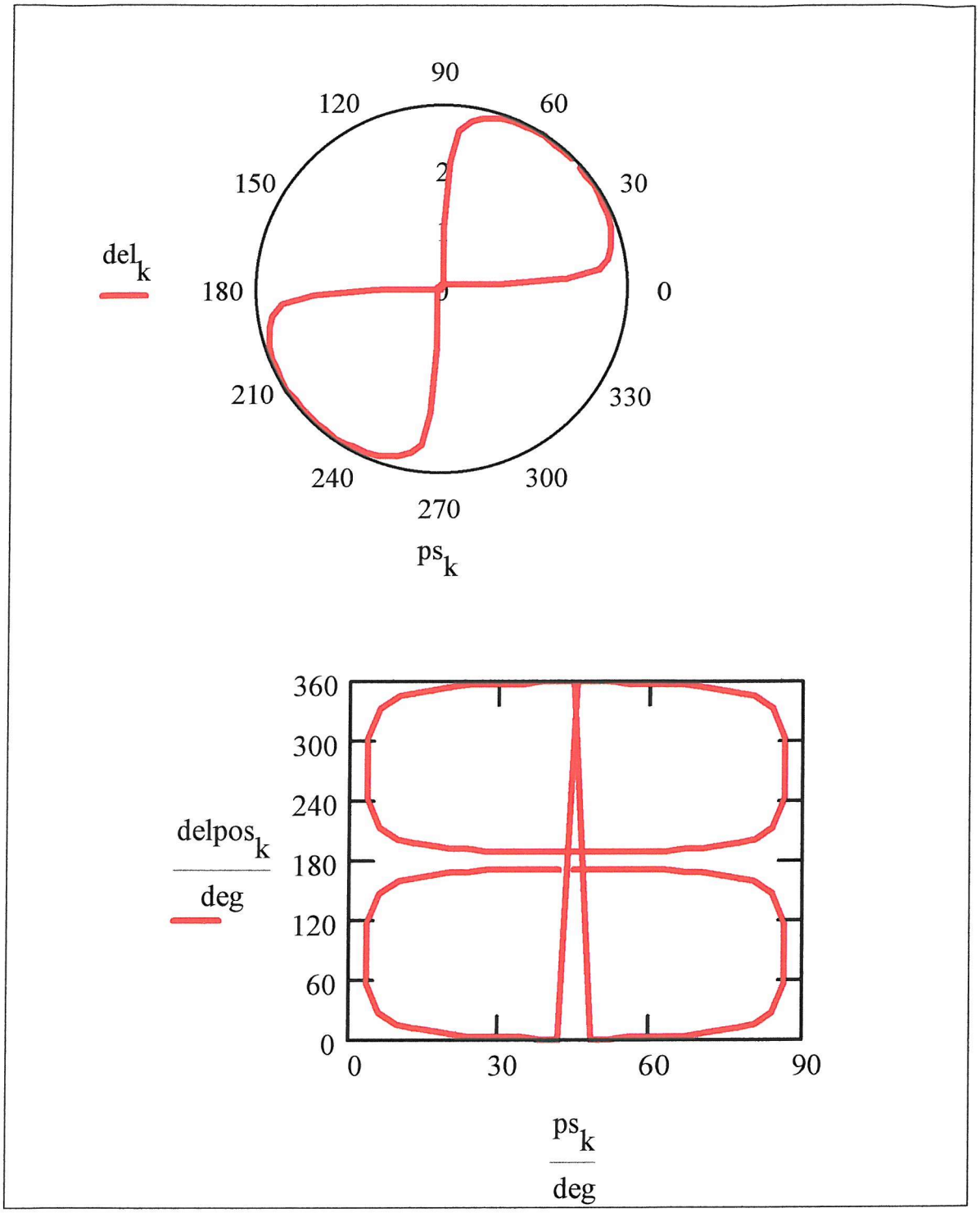

Pages 63-64
Box 4.2 **Mathcad Worksheet for Y-Cut Quartz (R.Greef), including graphs:**

4.2.1 Polar graph of Δ vs ψ

4.2.2 Graph of Δ and ψ vs α

4.2.3 Graph of Δ vs ψ

4.3.1.2 Transmission at 320nm

These experiments were carried out using a Xenon lamp as the source and as a result the incident intensity was much reduced. The reflected signal was correspondingly smaller and consequently the margin of error was much greater. Also the lamp has a bandwidth of 4nm which means the monochromator can allow light at $\lambda \pm 2$nm.

Cut	Δ/°	ψ/°
X	0.18 ± 1.5 (2σ)	Variable - see graph
Y	359.65 ± 3.0 (2σ)	Variable - see graph
Z (1mm)	181.53 ± 6.9 (2σ)	71.74 ± 1.16 (2σ)
Z (10mm)	3.05 ± 13.25 (2σ)	13.93 ± 4.18 (2σ)
Fused silica	0 ± 2.5	45.0 ± 0.2

Table 4.3 Polarimetry at 320nm; Δ and ψ values of Quartz Pieces

One of the most interesting features of the transmission behaviour of X- and Y- Cut quartz is the changeover in the ψ vs. α graphs between a regular inverted V shape at 632.8nm (Blue curves in figures 4.5, 4.7) and the saw-tooth appearance in the UV (Figures 4.9-4.10). There is still room for two complete cycles of data in the 180° range, but the negative gradient (decreasing ψ) is twice as large and the positive gradient is almost vertical. This behaviour can be mapped by the equation

$$\psi = \gamma - \tfrac{1}{2} \tan^{-1}|\tan 2(\alpha+\mu)| \qquad \textbf{Equation 4.1}$$

where y is the intercept on the y axis and μ is the offset from the crystal axis. The calculated values are given in table 4.4 below. The error calculated is

$$\text{Error} = \sqrt{\frac{\sum \left|\psi_{calc} - \psi_{obs}\right|^2}{n}} \qquad \textbf{Equation 4.2}$$

This is smaller than the actual size of the points in the Figures 4.9-4.10, except at points near to ψ=0° and ψ = 90° where discontinuities exist.

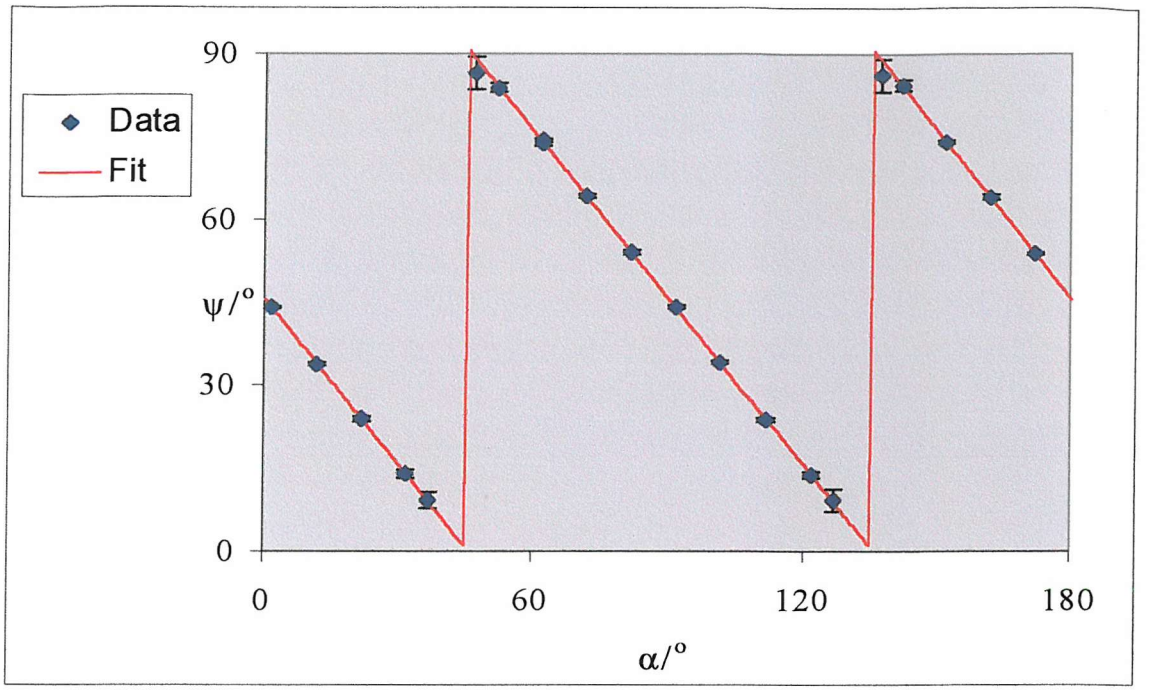

Figure 4.9 **Transmission Ellipsometry from 10mm thick Y-Cut Quartz - 322nm, 45° Linear Polarised Input Radiation: ψ vs α (Δ is invariant with α)**

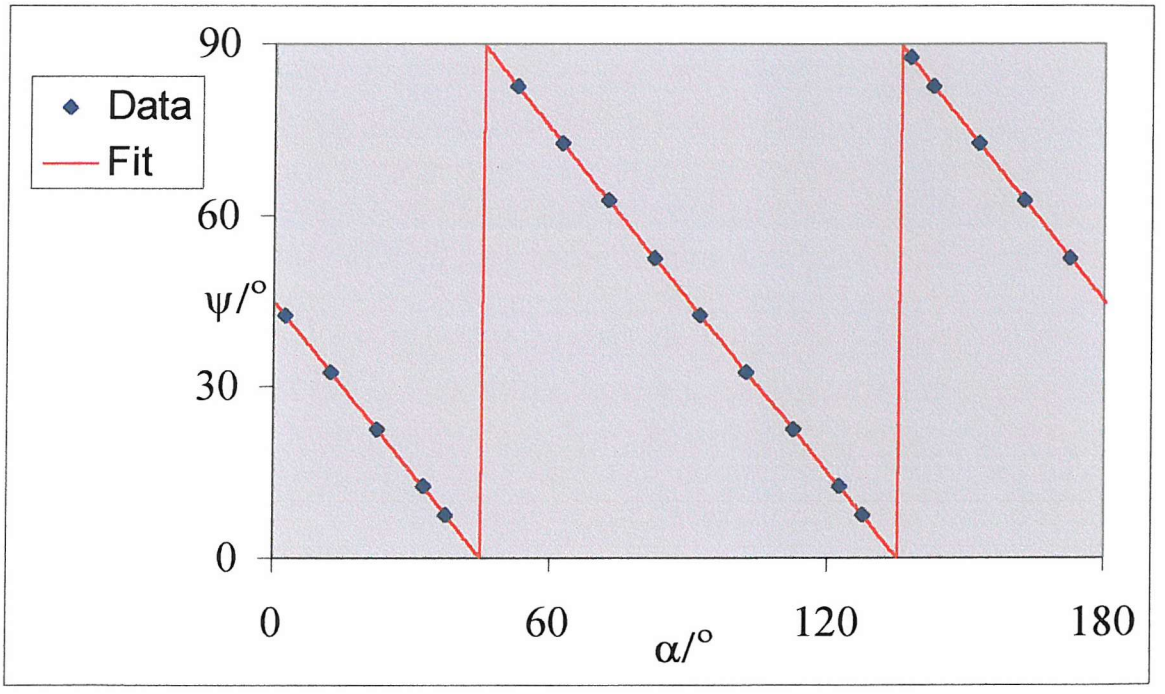

Figure 4.10 **Transmission Ellipsometry from 10mm thick X-Cut Quartz - 322nm, 45° linear polarised input radiation: ψ vs α (Δ is invariant with α). All error bars are smaller than the markers.**

Cut	γ/°	μ/°	Error/°
X	122.45	45.046	±0.602
Y	61.739	112.45	±0.694

Table 4.4 Constants for Transmission Ellipsometry at 320nm for X-and Y-Cut Quartz

The data presented for Z-Cut quartz above has been compared with calculations from specific optical rotatory power values, which are presented in Figure 4.11. Two sets of data have been referred to (Kaye and Laby (Ref. 4.3) and Panov (Ref. 4.4)).

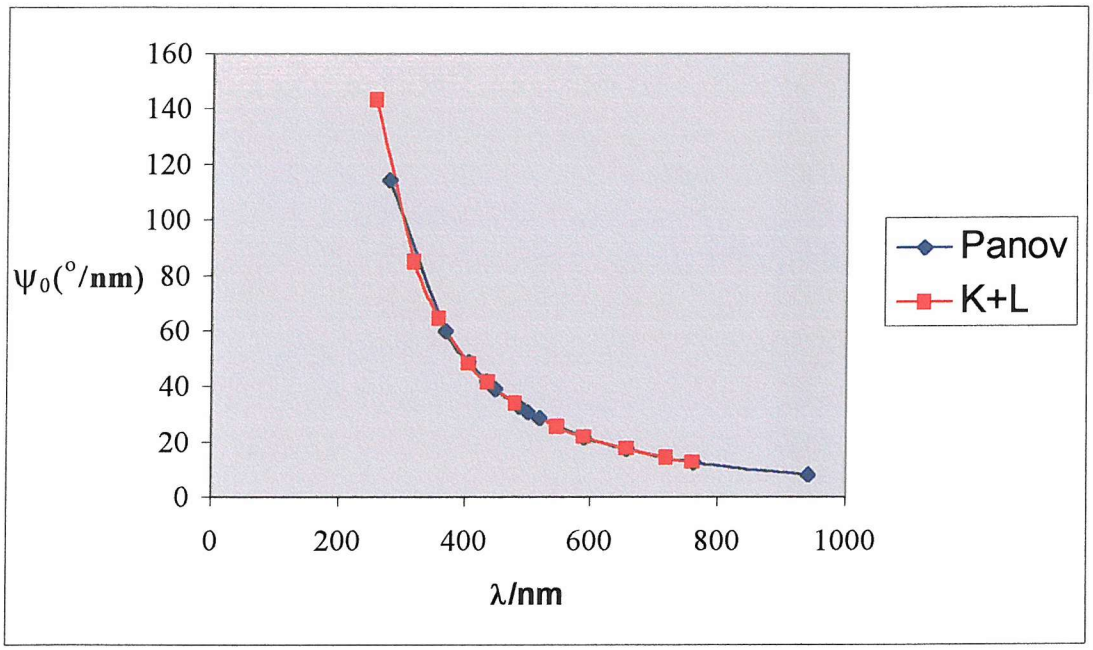

Figure 4.11 Optical Rotatory Power, ψ_0, vs Wavelength for Z-cut Quartz. Data from Kaye and Laby (Ref. 4.3) and Panov (Ref. 4.4).

This data was fitted to the following curves with high R^2 values

Panov: $\psi_0 = (2x10^7)\lambda^{-2.1675}$ $R^2 = 0.9995$

Kaye and Laby $\psi_0 = (3x10^7)\lambda^{-2.2101}$ $R^2 = 0.999$

which after interpolation, gave the following values of ψ_0, at the wavelengths studied:

	ψ_0 (°/mm)	
λ/nm	**Kaye & Laby**	**Panov**
632.8	19.322	16.955
322	86.002	73.325

Table 4.5 **Optical Rotatory Power at the wavelengths studied, calculated by interpolation in the results from Kaye and Laby (Ref. 4.3) and Panov (Ref. 4.4).**

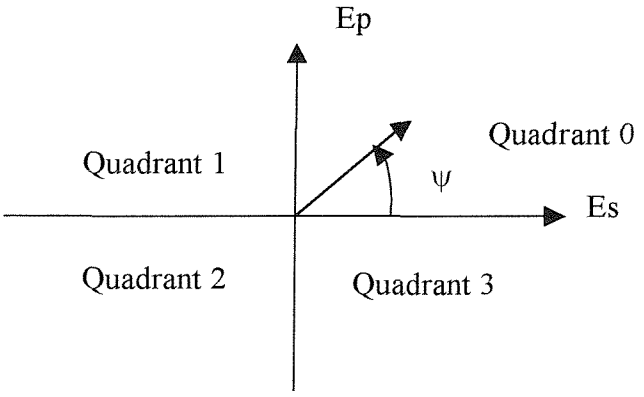

Figure 4.12 **Quadrant definitions used in fitting Z-cut quartz transmission data**

Source	ψ (°)	
	632.8nm	322nm
Experimental	**64.93 ± 0.081 [0]**	**71.74 ± 1.16 [1]**
Kaye and Laby (anti-clockwise)	**64.32 [0]**	48.98 [1]
Kaye and Laby (clockwise)	25.68 [0]	41.02 [3]
Panov (anti-clockwise)	61.95 [0]	**61.67 [1]**
Panov (clockwise)	28.05 [0]	28.33 [3]

Table 4.6 **Measured and Calculated values of ψ and [the Quadrant they are in] for the 1mm Piece of Z-cut Quartz. Assumes that Δ = 0/180°. Best-fit values are in bold.**

Source	ψ_0 (°/mm)	
	632.8nm	322nm
Experimental (anticlockwise)	**19.93 ± 0.081**	**63.26 ± 1.16**
Experimental (clockwise)	160.07	116.74
Kaye and Laby	**19.32**	86
Panov	16.95	**73.33**

Table 4.7 **Calculated values of the Optical Rotatory Power, ψ_0, for the 1mm Piece of Z-cut Quartz. Assumes that Δ = 0/180°. Best-fit values are in bold.**

The following conclusions can be drawn from this data:

1) The results are very close to those predicted in Kaye and Laby in the visible.

2) However they are closer to Panov in the UV.

3) The rotation is definitely anticlockwise.

Source	ψ(°)	
	632.8nm	**322nm**
Experimental	**54.39 [2]**	**13.93 + 4.18 [0]/[2]**
Kaye and Laby Anticlockwise	58.22 [2]	**5.02 [2]**
Kaye and Laby clockwise	31.78 [2]	84.98 [2]
Panov anti-clockwise	34.5 [2]	58.25 [0]
Panov clockwise	**56.5 [2]**	31.75 [0]
From 1mm Experimental	64.93 [2]	47.6 + 11.6 [3]

Table 4.8 **Measured and Calculated values of ψ and [the Quadrant they are in] for the 10mm Piece of Z-cut Quartz. Assumes that Δ = 0/180°**

Source	$d\psi_0$(°)	
	632.8nm	322nm
Experimental anticlockwise	**189.39**	688.93/**868.93**
Experimental clockwise	170.61	751.07
Kaye and Laby	**193.2**	**860**
Panov	169.5	733
From 1mm Experimental	199.3	632.6 ± 11.6

Table 4.9 **Calculated values of the Total Optical Rotation, $d\psi_0$, where d is the thickness of the plate, for the 10mm Piece of Z-cut Quartz. Assumes that Δ = 0/180°**

For the 10mm piece, the interpretation is more difficult. In the UV the data is closer to that obtained by Kaye and Laby in an anticlockwise direction, but in the visible Panov clockwise is the best fit.

The results from the 1mm and the 10mm pieces are not internally consistent in the UV. This may be attributed to the exponential rise in the optical rotary power with decreasing wavelength, leading to a significant change as wavelength increases by each 1nm. Also, the Kaye and Laby and Panov measurements were made using lasers, which provide a more intense and more coherent light source, leading to more accurate results. However, the measurements made are useful in a qualitative sense, in establishing the handedness of the 1mm piece and providing two potential models for the 10mm piece.

4.3.1.3 Reflection at 632.8nm

For the X and Y-Cut pieces Δ was virtually 0 and ψ was invariant with α. They had identical values which gave a rotation of the linearly polarised light of $25.5 \pm 180n°$ for the 10mm piece. After considering the values for transmission, the most realistic value is n=1 leading to a specific rotation of 20.55° per mm thickness. The Z-cut quartz also had a zero value of Δ and a slightly higher value of ψ, leading to a specific rotation of 23.2°/mm.

Cut	Δ /°	ψ/°
X (10mm)	0.74 ± 0.4	19.51 ± 0.03
Y (10mm)	0.41 ± 0.3	19.50 ± 0.04
Z (1mm)	0.00 ± 0.4[1]	21.80 ± 0.03

Table 4.10 Reflection Ellipsometry at 632.8nm. ϕ=70° - Δ and ψ values

[1]Value measured was $359.60 \pm 0.8°$, but as Δ must be > 0, the value above is presented

4.3.1.4 Ellipsometry Conclusion

The polarimetric behaviour of X and Y cut quartz has been mapped at two wavelengths, one in the visible and one in the UV, giving expected Δ-ψ trajectory for a crystalline optical rotator. For reflection ellipsometry, the Δ–ψ trajectories are represented by a single point. The 'saw-tooth' repetition pattern in the ψ vs. α plots for X- and Y- cut quartz is an interesting feature of this experiment. It has been successfully mapped, but a physical explanation is yet to be found.

For Z cut quartz, the optical rotation of the crystal was clearly visible in the shift in ψ from the expected 45°. From comparison of the results obtained experimentally with literature values, the conclusion is that the rotation along the optic axis is definitely anticlockwise (i.e. left-handed) for the 1mm piece and inconclusive for the 10mm piece. However no rotational anisotropy is detectable in the Δ and ψ values, so the next step is to investigate at the microscopic level.

4.3.2 Second Harmonic Generation

4.3.2.1 Transmission at 640/320nm

Measurements were recorded for all three flats in transmission using an oscilloscope for signal averaging, with the peak to peak signal averaged over 100 sweeps.

The results for bulk transmission without the analyser or QWP were qualitatively as predicted by Franken and co-workers (Ref. 4.6):

- Neither the fused silica nor the X-cut sample generated a second harmonic beam.
- The SHG Intensity from Y-cut quartz varied as the quartz piece was rotated.
- The Z-cut piece produced a harmonic, which was constant with mechanical angle.

The focus of this work was to investigate Z-Cut quartz to establish whether the quartz took the α or β form. Franken's work was done without an analysing polariser, so the first step was to measure the intensity generated in the presence of an analyser set to transmit P polarised light (A=0°)

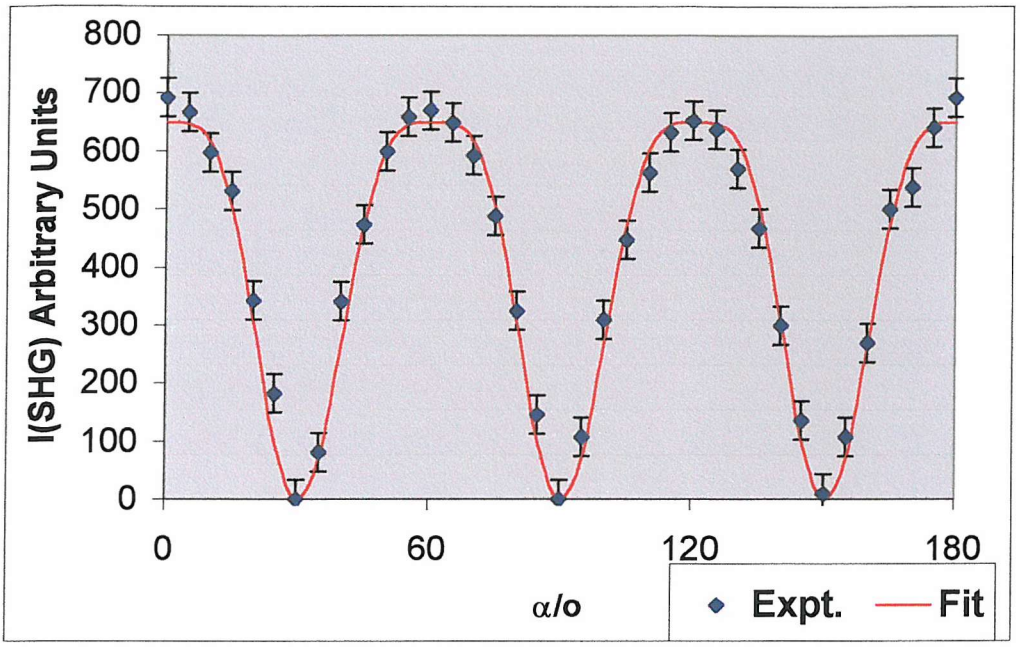

Figure 4.13 Transmission SHG (320nm) from the 1mm thick Z- cut Quartz; no QWP, A = 0°.

The results for the Z-cut piece showed a pattern that could be modelled by a function of the form;

$$I = A + B\cos^2(3\alpha + \mu) + C\cos^4(3\alpha + \mu) \qquad \textbf{Equation 4.3}$$

Where I is the signal intensity, A is a constant due to a dark current, B is a constant function of signal magnitude, α is the mechanical angle and μ is an arbitrary phase angle. As the graph went down to zero within experimental error, A was assigned the value zero.

The best fit gave

$A = 0$; $B = 1313.081$; $C = -663.684$; $\mu = -0.44053°$

A common feature with all of this work with quartz is that the pattern of the graphs appear to suggest 2N- fold repetition (N=1 for Y-cut, 2 for X-cut, 3 for Z-cut). However, it should be noted that the intensity is a sum of the squares of the E_p and E_s electric fields, which can be either positive or negative. Therefore the E values follow a

sin wave pattern which goes through N cycles per full rotation of the quartz plate. This is in agreement with the trigonal symmetry model for Z-Cut quartz.

The mechanical angle dependence of SHG intensity for Y-cut quartz is described in Figure 4.14. First results are given for an experiment without the QWP or the analyser.

$$I = A + B\cos^2(\alpha + \mu) \qquad \textbf{Equation 4.4}$$

The best fit gave

$A = 0.280854$; $B = 2301.348$; $\mu = 37.09058°$

Again A can be considered as 0 within experimental error.

If an analyser was inserted before the detector and set to transmit p-polarised light, the results for Y-cut quartz show zero SHG intensity for angles between 5 and 65°.

The introduction of the analyser removes the s-component of the intensity before the light reaches the detector. This leads to the low signal at mechanical angles of less than 70°.

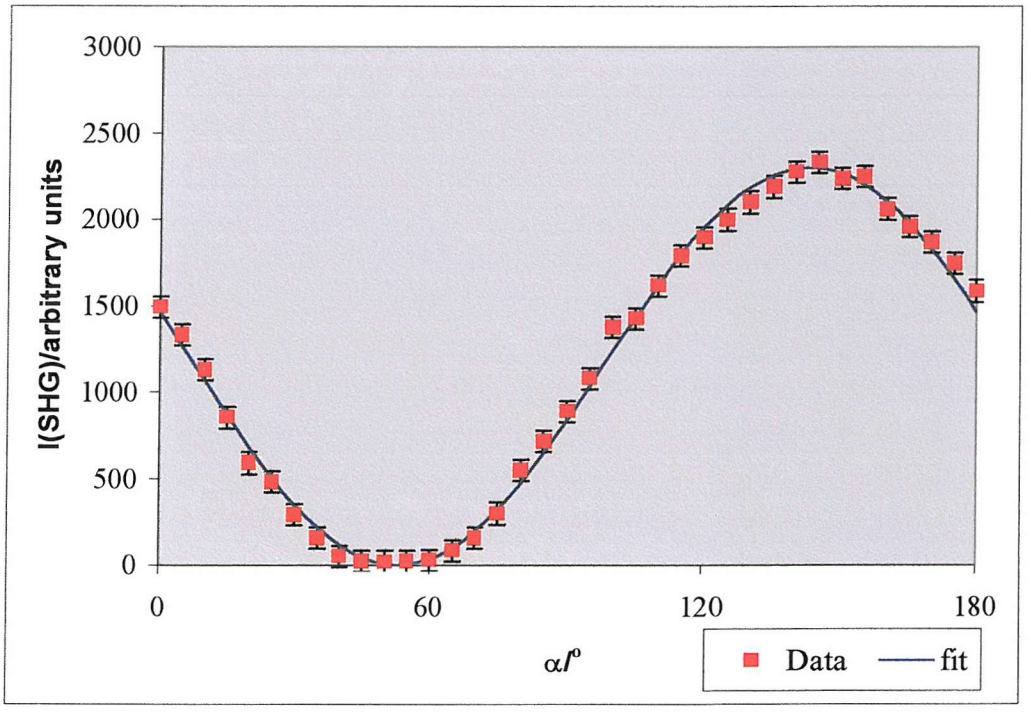

Figure 4.14 Transmission SHG at 640/320nm for 10mm thick Y-cut Quartz; no QWP, no Analyser.

4.3.2.2 Reflection at 640/320nm

4.3.2.2.1 SHG-ORD from Z-cut Quartz

Optical rotation experiments were conducted with p polarised input light. Intensity measurements gave consistent results with both p and s polarised components of the second harmonic repeating in 60° cycles. These were 30° out of phase with one another. The difference in magnitude of the cycles is unexplained.

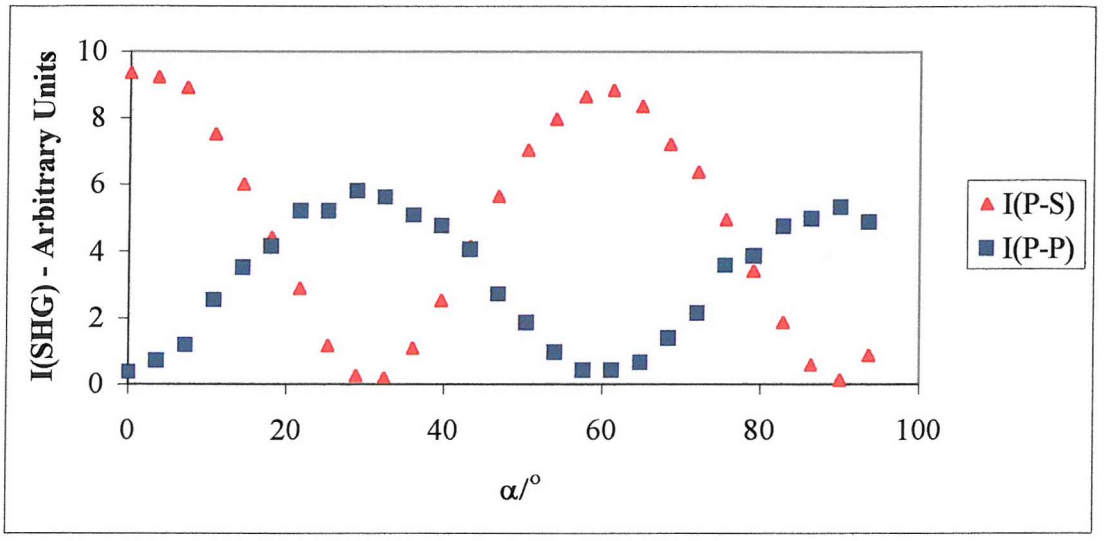

Figure 4.15 SHG from Z-cut quartz ($\phi = 70°$). Graphs of Intensity vs α for Polariser Combinations P in - P out and P in - S out.

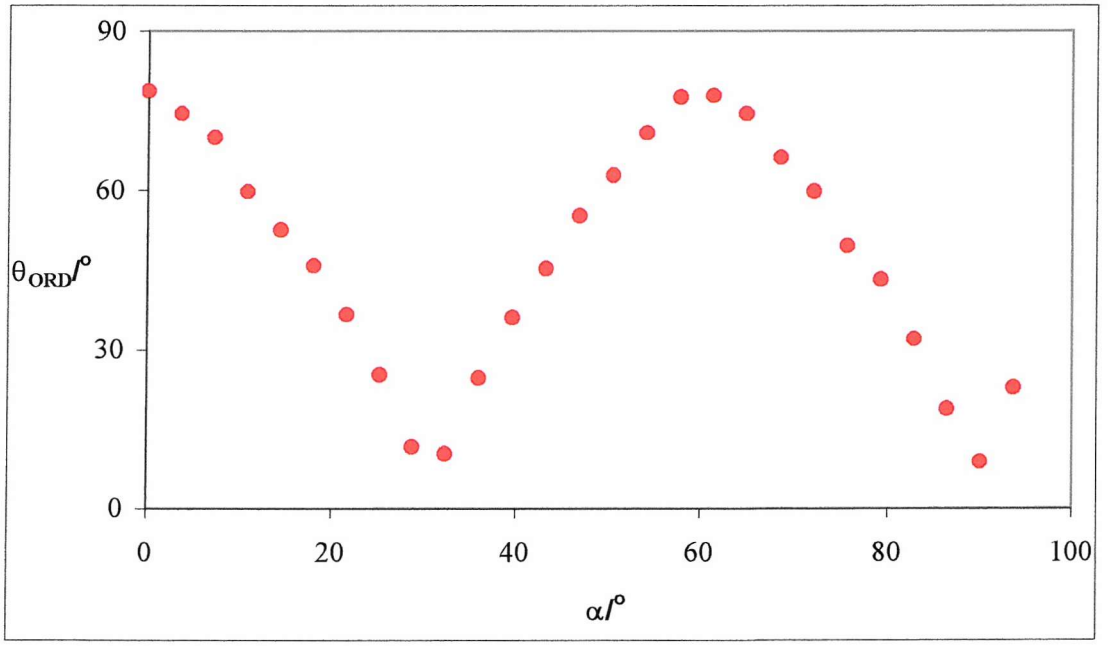

Figure 4.16 Reflection SHG from Z-cut quartz ($\phi = 70°$). θ_{ord} vs α.

As the sample is rotated, θ_{ORD} varies as a function of sin6θ, again reflecting three-fold symmetry again consistent with the structure of α-quartz (Figure 4.16).

4.3.2.2.2 SHG-CD from Z-cut Quartz

Measurements for fused silica showed that all differences between SHG intensities produced by input right and left circularly polarised light were within experimental error (i.e. as expected, I(SHG-CD)=0).

For Z-cut quartz SHG intensity varied with the direction of polarisation of the input radiation. The effect was asymmetric about zero.

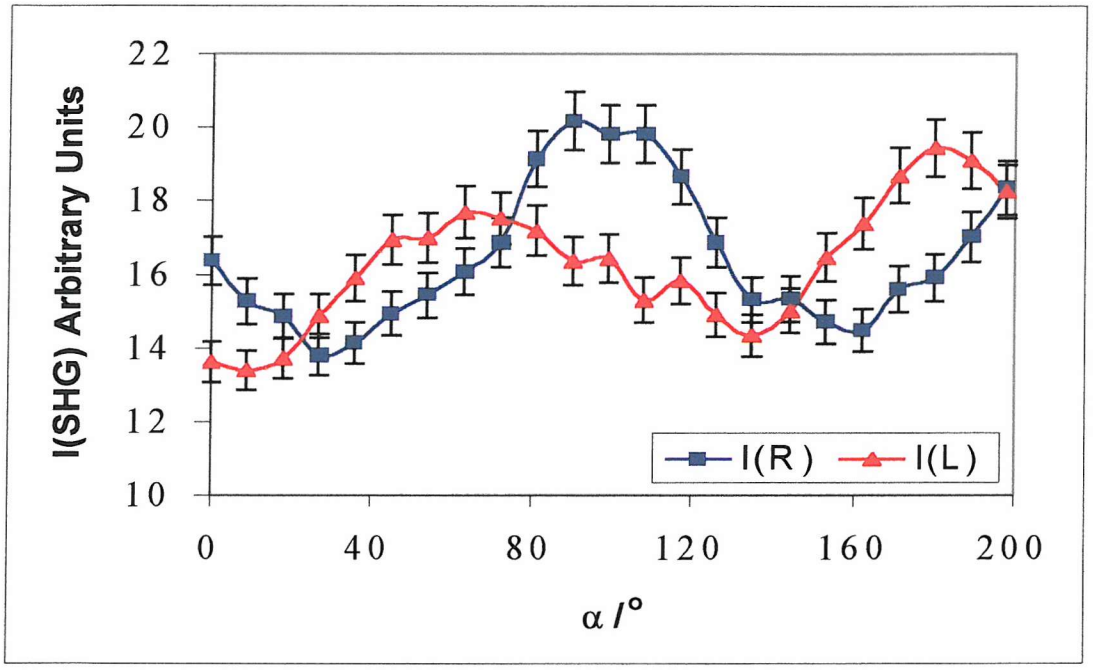

Figure 4.17 SHG Intensity from Z-Cut Quartz (ϕ=70°) with left and right circular polarised input light; A= 0.

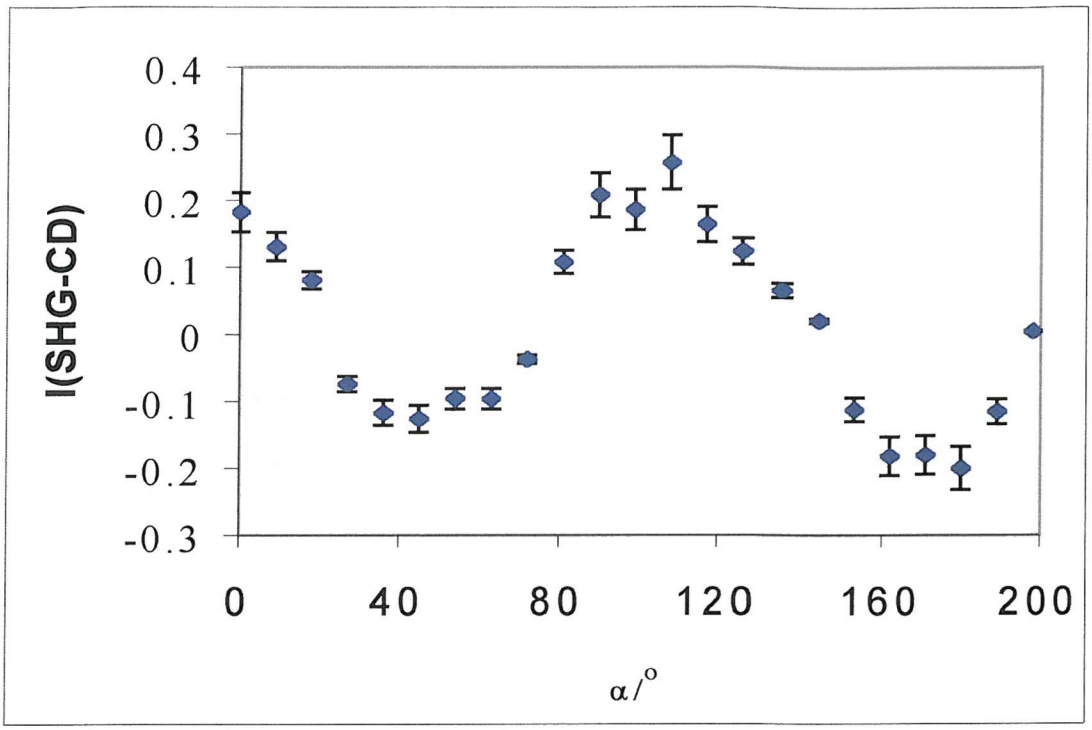

Figure 4.18 SHG-CD from Z-Cut Quartz (ϕ = 70°); A= 0.

4.3.2.2.3 SHG Intensity at 640/320nm and 560/280nm

The curve for SHG from Z-Cut Quartz at 640/320nm is shown in Figure 4.19 below. The behaviour shows the now familiar six-fold repetition representing the trigonal structure. The main feature is that there is an intensity offset of 250 arbitrary units, which accounts for over 50% of the maximum intensity. The curve for 560/280nm (Figure 4.20) however, although it shows the same six-fold pattern, has a minimal offset (< 10% of the maximum intensity).

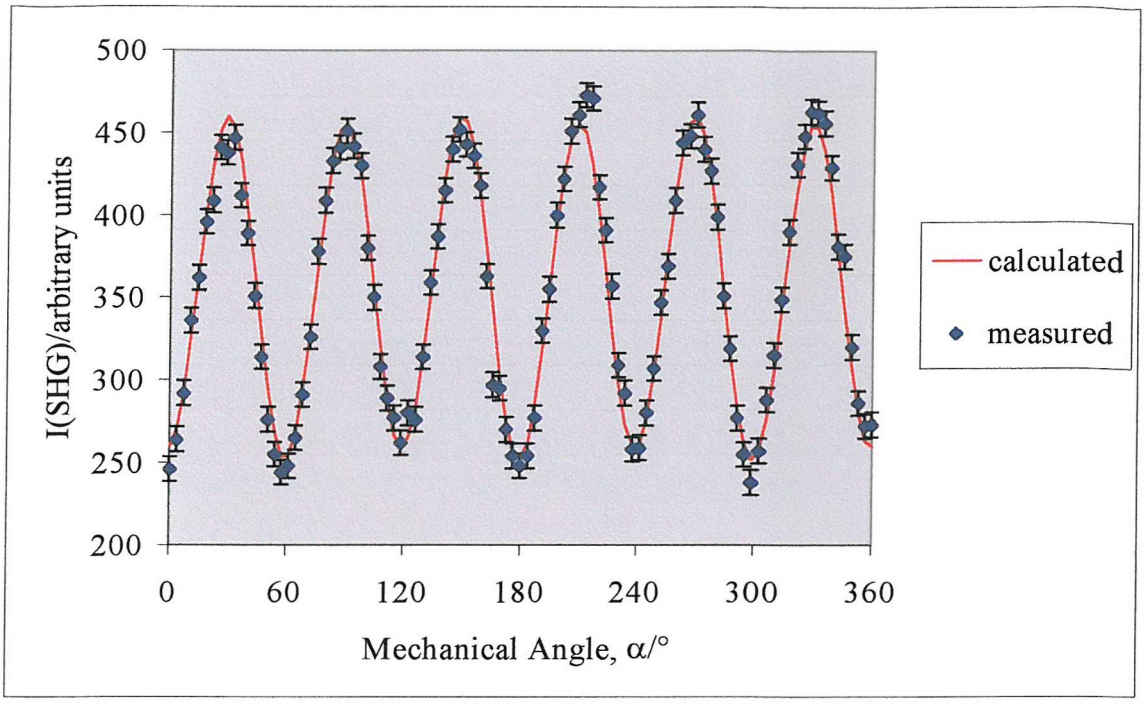

Figure 4.19 SHG from 10mm Z-Cut Quartz: reflection at 640/320nm; $\phi = 70°$

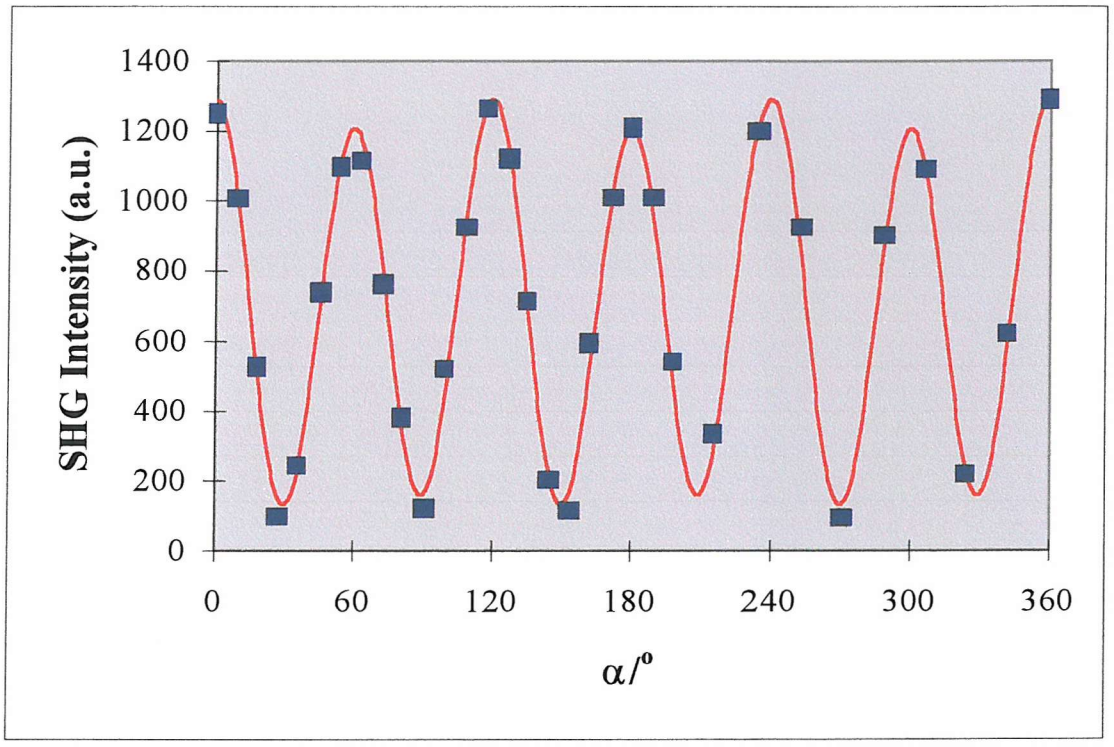

Figure 4.20 SHG from Z- cut Quartz: Reflection at 560/280nm; $\phi = 70°$

4.3.3 Second Harmonic Ellipsometry at 640/320nm (SHE)

This experiment provides more information about the second harmonic behaviour than does SHG, as the complete polarisation state of the second harmonic can be calculated. Previously, data was only collected at discrete polarisation settings and the full picture

was not available. A further advantage is that the direct measurement of the ellipsometric parameters, Δ and ψ, is a much more efficient process as the data is collected in one measurement. The accuracy is also improved because, before the experiment begins, the polariser and analyser are fixed at precisely 45° and 0° respectively (By a nulling technique) and never moved. In a SHG experiment, at least one of the polarisers is rotated between each discrete polarisation setting and this means that random errors are possible.

The experimental set-up is similar to that of SHG (chapter 3), but with two vital exceptions. Firstly, a quarter wave plate is inserted between the sample and the analyser and it is used in the same way as in an ellipsometric experiment. Secondly, although the second harmonic is detected in the same way, the computer program used records a second harmonic intensity (averaged over 100 points) for each quarter wave plate angle as the plate is rotated. The software then provides the values of Δ and ψ in the same manner as the ellipsometric experiment described earlier.

Measurements have been made in transmission for the Y- and Z- cut quartz flats. As there is negligible SHG signal for the X- cut piece, no useful data can be obtained from it. The quarter wave plate was rotated in 100 3.6° steps and intensity values were averaged over 100 points for each QWP angle. From this data, Δ and ψ could be calculated for this particular value of the mechanical angle. This was repeated for mechanical angles in 5° steps between 0 and 180° and in the case of the Y- cut piece, as frequently as possible at angles where Δ was changing rapidly. The results for Z- cut quartz are presented in Figures 4.21-4.25.

SHE measurements confirm the presence of three-fold symmetry in the quartz. For example a graph of ψ vs mechanical angle (α) has a period of 60°. The Δ vs α plot has a period of 120° with few points with significant circular components ($\Delta \neq 0$, 180 or 360°). Further calculations will determine the relevance of these points. A graph of Δ against ψ again shows a plot with a period of 120°.

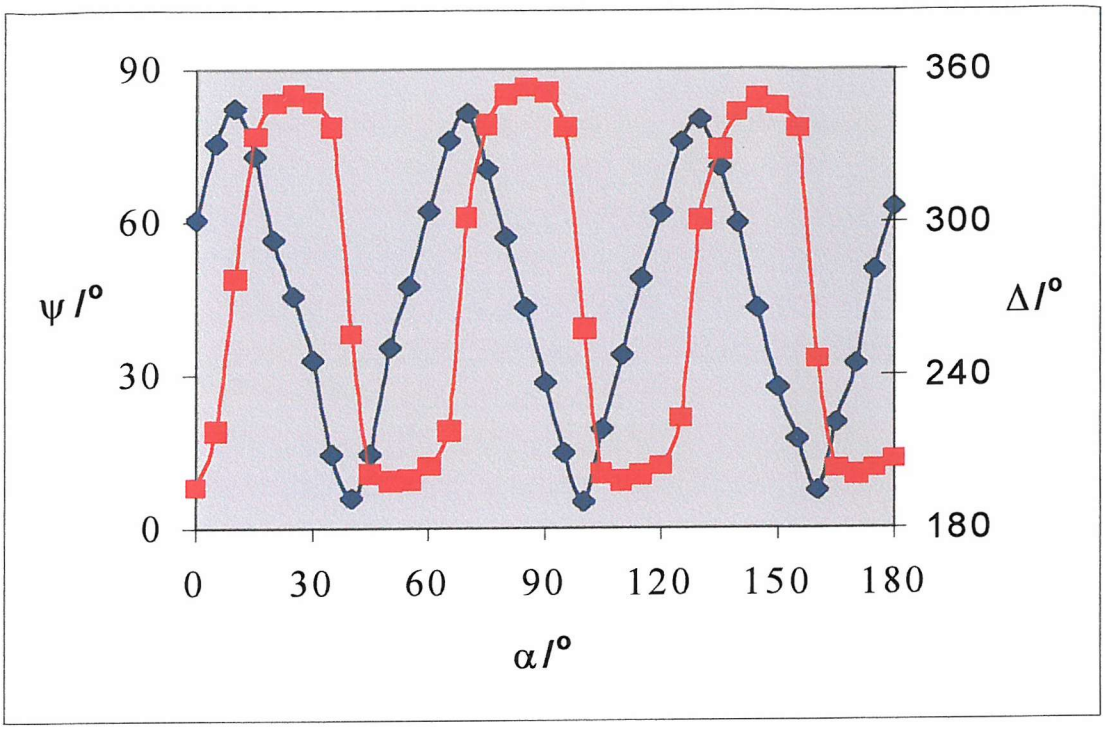

Figure 4.21 **Transmission SHE from Z-Cut Quartz at 640/320nm. ψ and Δ vs Mechanical Angle, α.**

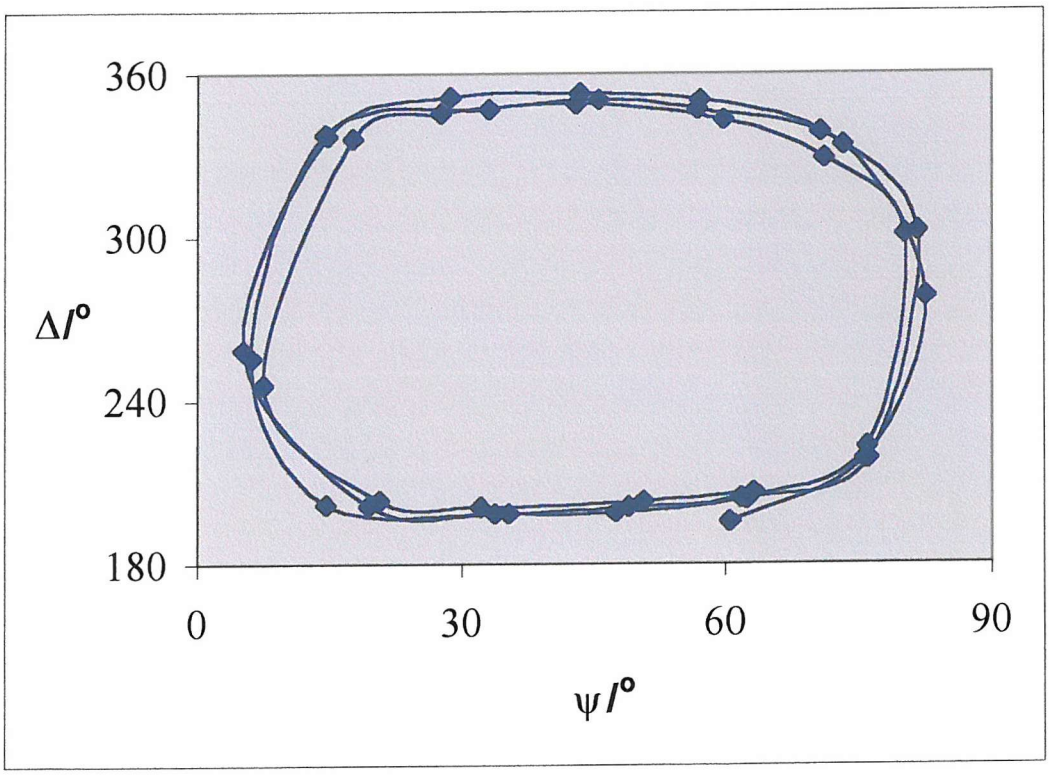

Figure 4.22 **Reflection SHE from Z-Cut Quartz at 640/320nm: Δ vs ψ.**

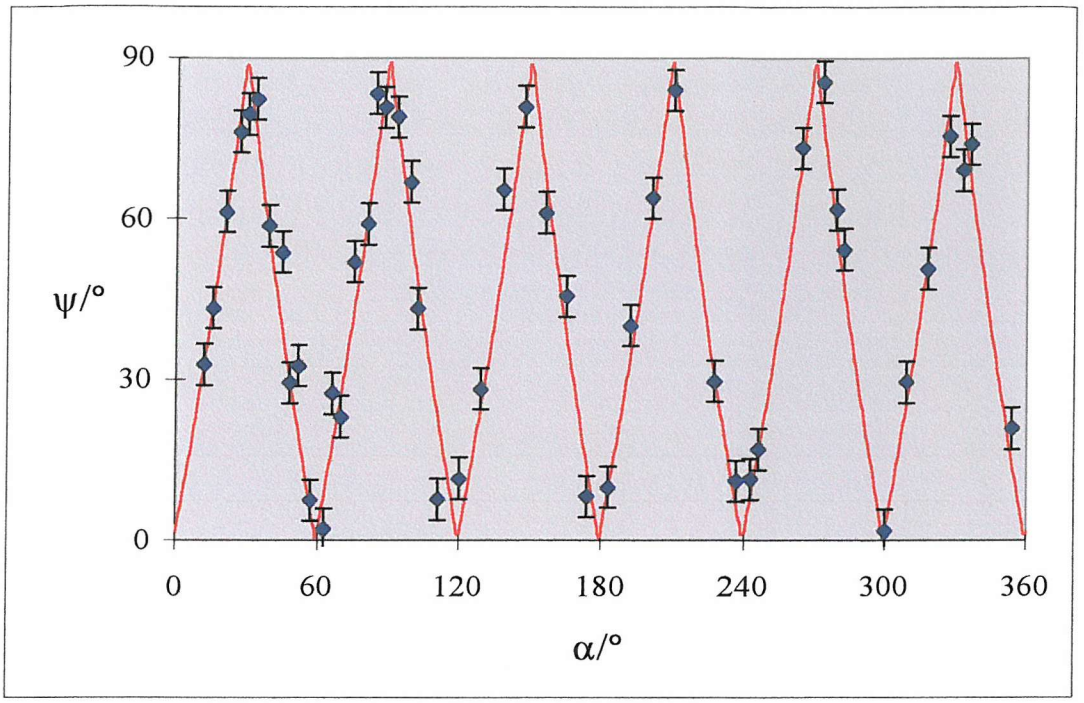

Figure 4.23 **Reflection SHE from Z-Cut Quartz at 640/320nm with ϕ =70°: ψ vs α.**

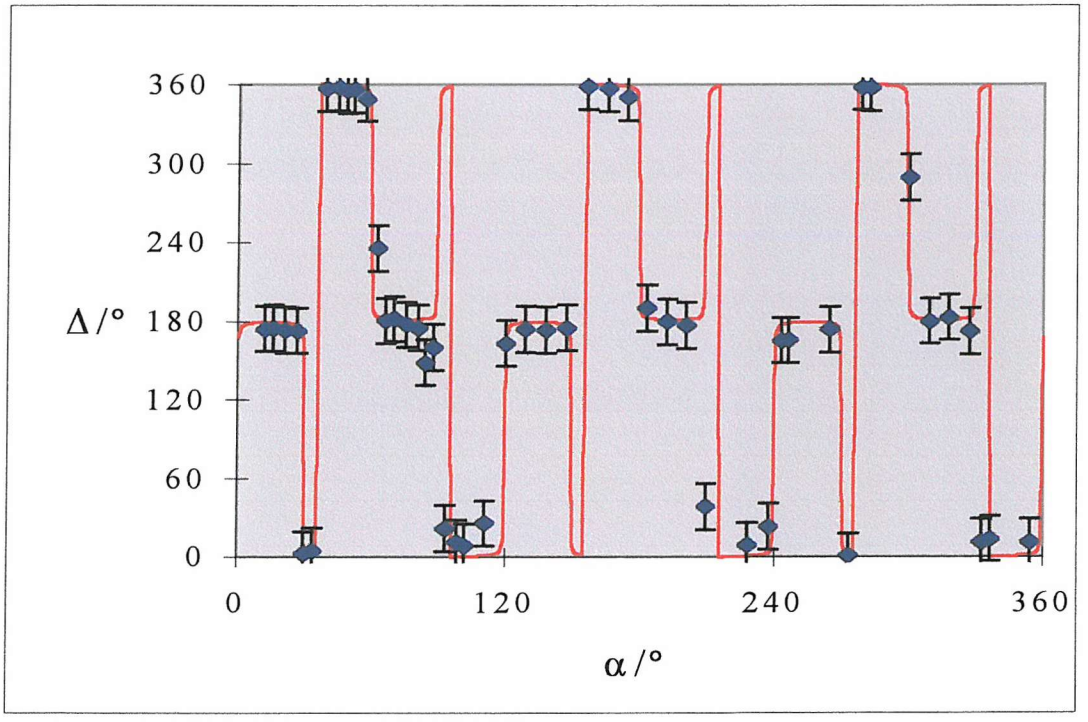

Figure 4.24 **Reflection SHE from Z-Cut Quartz at 640/320nm with ϕ =70°: Δ vs α.**

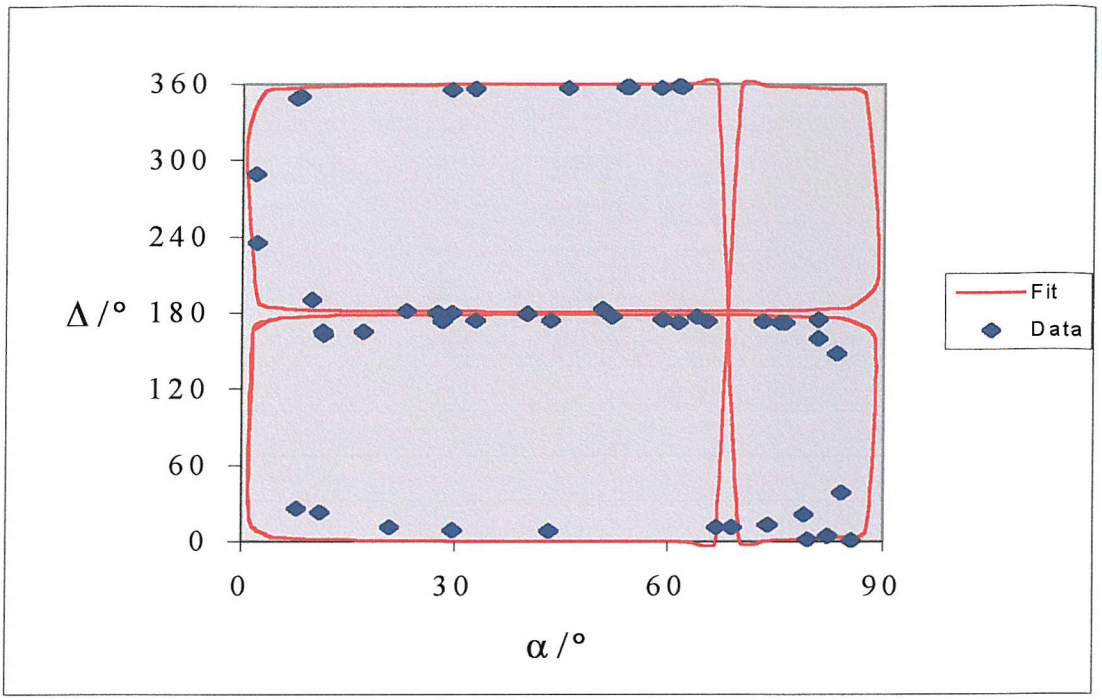

Figure 4.25 Reflection SHE from Z-Cut Quartz at 640/320nm with ϕ =70°: Δ vs ψ.

4.3.3.1 SHG and SHE from Z-Cut Quartz - Fitting

The next objective of this work was to fit the data obtained in a manner that would describe both second harmonic and ellipsometric behaviour of the quartz. The Electric Field strength E can be broken up into its components in 3 dimensions (Ref. 4.7). For 45 input polarisation these are:

$$E_x = -\frac{1}{\sqrt{2}} E \cos\phi$$

$$E_y = \frac{e^{i\delta}}{\sqrt{2}} E \qquad \textbf{Equations 4.5}$$

$$E_z = \frac{1}{\sqrt{2}} E \sin\phi$$

It was assumed that the quartz piece in question is α–quartz and therefore trigonal in symmetry. As a result, only two elements of the $\vec{\chi}^{(2)}$ tensor were non-zero (Ref 4.7):

1) χ_{xxx} which can be present in all molecules

2) χ_{xyz} which is only non-zero for chiral molecules. It may be complex, in this

case due to a tail of a quartz absorption further into the ultraviolet.

These are denoted as χ_1 and χ_2 respectively.

As we are working with the Z-cut piece we are interested in the XY plane and therefore the surface polarisation in the x and y directions ($P_z = 0$). P_x and P_y can be broken down into the following:

$$P_X = \left\{ \chi_1 \cos 3\alpha \frac{(\cos^2 \phi)}{2} - \chi_1 \cos 3\alpha \frac{e^{2i\delta}}{2} + 2\chi_1 \sin 3\alpha \frac{(-\cos\phi)}{\sqrt{2}} \frac{e^{i\delta}}{\sqrt{2}} + 2\chi_2 \frac{e^{i\delta}}{\sqrt{2}} \frac{\sin\phi}{\sqrt{2}} \right\}$$

$$P_y = \left\{ \chi_1 \sin 3\alpha \frac{(\cos^2 \phi)}{2} - \chi_1 \sin 3\alpha \frac{e^{2i\delta}}{2} + 2\chi_1 \cos 3\alpha \frac{(-\cos\phi)}{\sqrt{2}} \frac{e^{i\delta}}{\sqrt{2}} + 2\chi_2 \frac{e^{i\delta}}{\sqrt{2}} \frac{\sin\phi\cos\phi}{\sqrt{2}} \right\}$$

Equations 4.6

Assuming $\delta=0$, these are

$$P_X = -\frac{1}{2}\chi_1 \sin^2 \phi \cos 3\alpha - \chi_1 \cos\phi \sin 3\alpha + \chi_2 (\sin \phi)$$ **Equations 4.7**

$$P_y = -\frac{1}{2}\chi_1 \sin^2 \phi \sin 3\alpha + \chi_1 \cos\phi \cos 3\alpha + \chi_2 (\sin\phi \cos\phi)$$

From this the electric field strengths of the outgoing beams are

$$E_p = P_x \cos\theta$$ **Equations 4.8**
$$E_s = P_y$$

The intensity of the second harmonic wave is then

$$I(SHG) = E_p^2 + E_s^2$$ **Equation 4.9**

This equation was fitted against the data to obtain the best values for χ_1 and χ_2, and these were found to be 63.30 and -1.817 respectively. This fit is shown in Figure 4.26 above. The presence of the non-zero χ_2 is responsible for the asymmetry between the odd and even peaks.

The values of ψ and Δ were calculated using the same values of χ_1 and χ_2 but with the introduction of the imaginary part of χ_2 and the Fresnel reflection coefficients for the quartz. These were combined to form a constant ($r_{tot} = r_s/r_p$) and ψ was calculated by:

$$\tan\psi = \frac{E_p}{r_{tot}E_s} = \frac{P_x\cos\phi}{P_y} \qquad \textbf{Equation 4.10}$$

Δ was given by

$$\Delta = \delta_p - \delta_s \qquad \textbf{Equation 4.11}$$

Where

$$\delta_p = \tan^{-1}\left(\frac{\mathrm{Im}(E_p)}{\mathrm{Re}(E_p)}\right) \qquad \delta_s = \tan^{-1}\left(\frac{\mathrm{Im}(E_s)}{\mathrm{Re}(E_s)}\right) \qquad \textbf{Equations 4.12}$$

δ_p and δ_s are calculated with regard to the quadrant in which they are found. $\Delta = 0$ is taken as the positive real axis in the Argand diagram. The values were calculated for χ_1 =63.30 χ_2 = -1.817 + 0.685i and r_{tot} = 0.4.

The complex value of χ_2 has almost no effect on the intensity fit, but the introduction of r_{tot} does significantly.

4.3.3.2 SHE from Y-Cut Quartz

Data from Y-Cut quartz for transmission is shown in Figures 4.26-4.27 and reflection data is shown in Figures 4.28-4.29. Unlike the Z-Cut quartz the data does not repeat as the quartz is rotated. The absence of screw axes means that the arrangement of atoms in Y-cut quartz is asymmetric. It was impossible to find a fit for this data that had any physical significance.

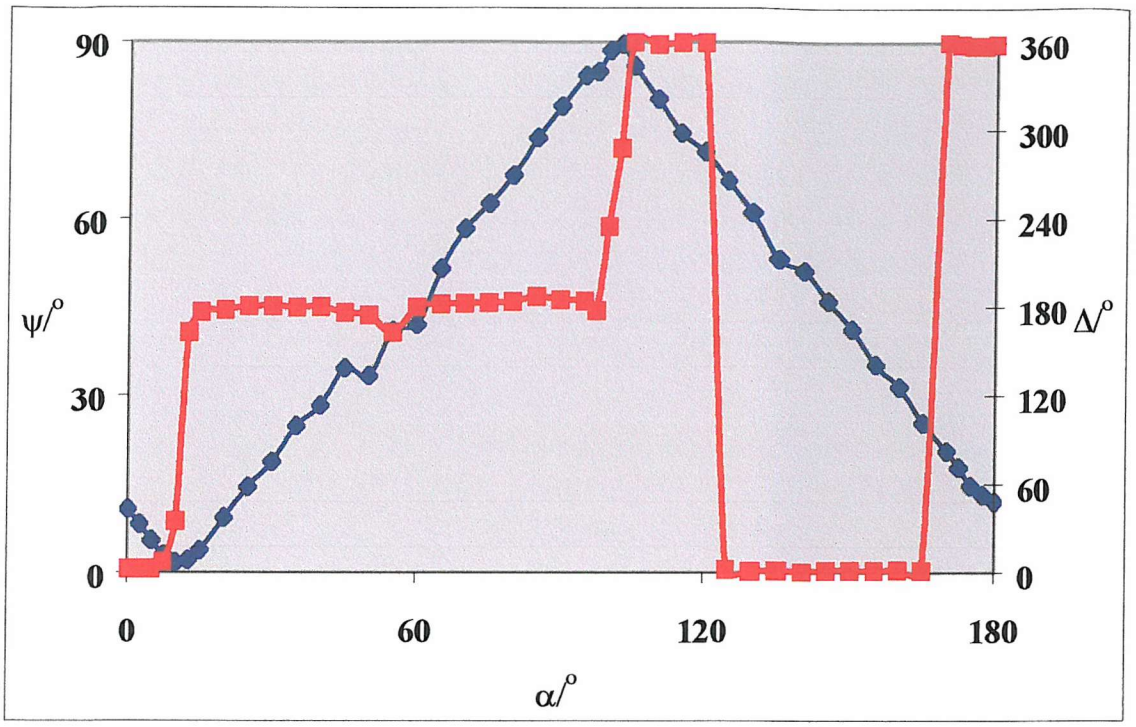

Figure 4.26 **Transmission SHE from Y-Cut Quartz at 640/320nm with ϕ =70°: a) ψ and b) Δ vs α.**

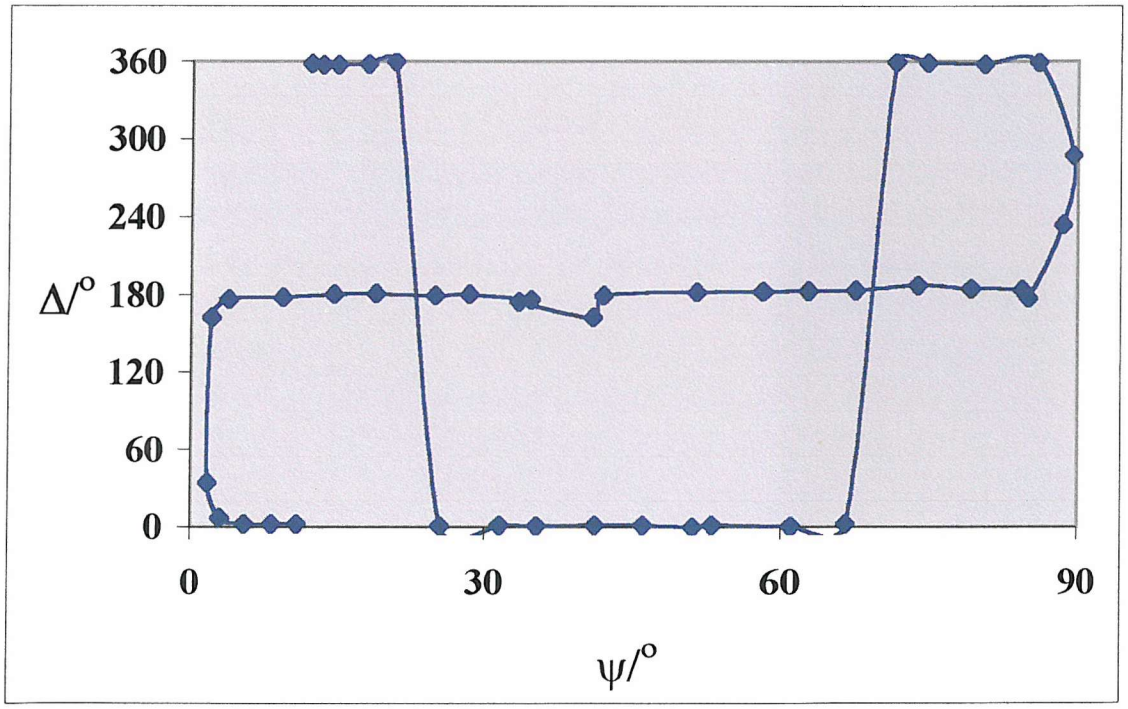

Figure 4.27 **Transmission SHE from Y-Cut Quartz at 640/320nm with ϕ =70°: Δ vs ψ.**

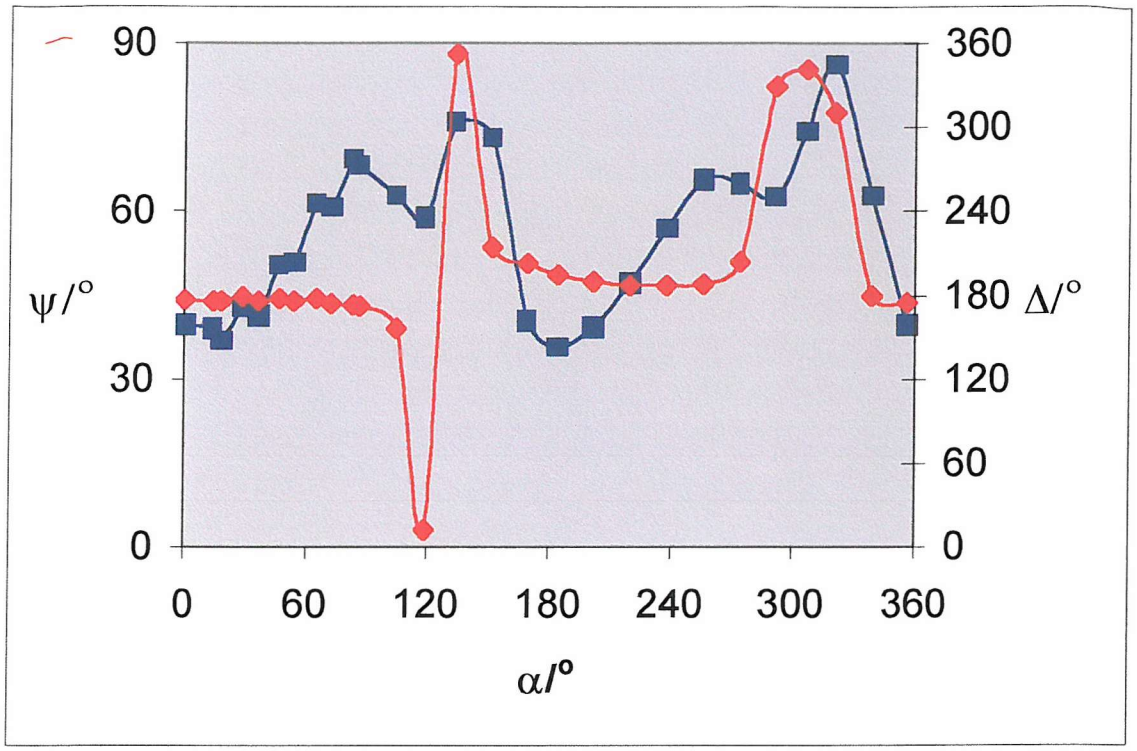

Figure 4.28 **Reflection SHE from Y-Cut Quartz at 640/320nm with ϕ =70°: a) Δ and b) ψ vs α.**

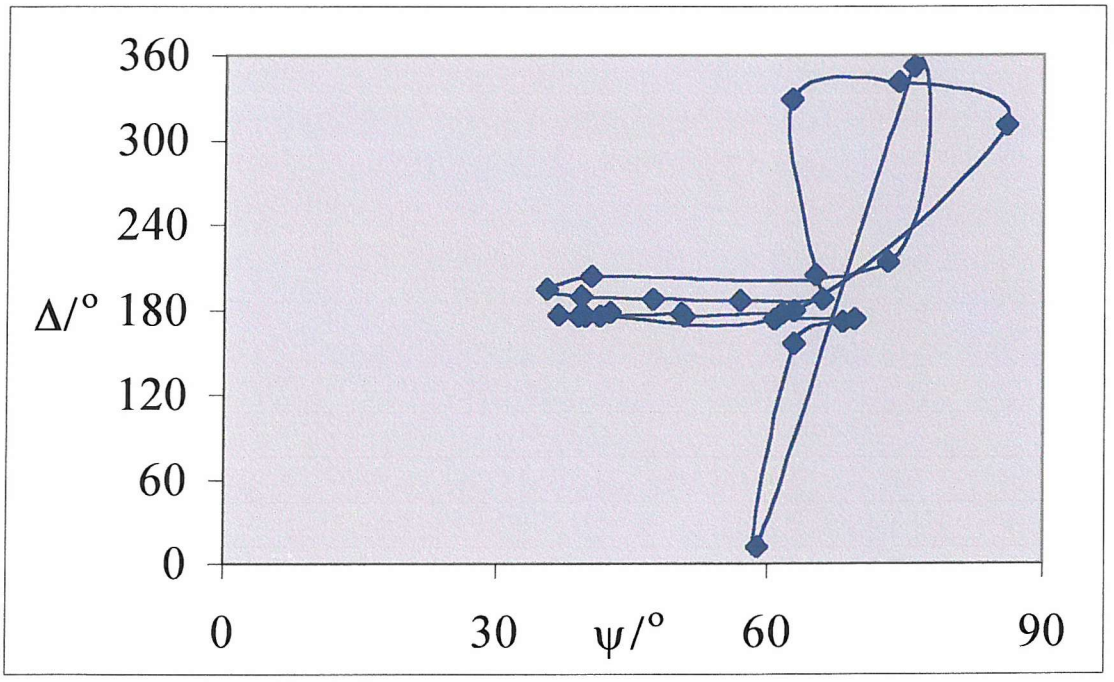

Figure 4.29 **Reflection SHE from Y-Cut Quartz at 640/320nm with ϕ =70°: Δ vs ψ.**

References

4.1 Supplier's Catalogue (Halbo Optics), 1997.

4.2 G Johnson and J Foise, *Encyclopaedia of Applied Physics*, **15** VCH Publishers (1996) 368.

4.3 G.J.C. Kaye and T.H. Laby, *Tables of Physical and Chemical Constants*, 16th Ed. Longman, London and New York (1995).

4.4 V.A. Panov, *Handbook of Designer of Optomechanical Instruments,* Mashinostroenie, Leningrad (1980).

4.5 Supplier's Catalogue (Orbit), 1996.

4.6 P. A. Franken, A. E. Hill, C. W. Peters and G. Weinreich, *Phys. Rev. Lett.*, **7(4)** (1961) 118.

4.7 S.V. Popov, Y.U.P. Surkev and N.I. Zheludev, *Susceptibility Tensors for Nonlinear Optics* (Bristol Institute of Physics and Philadelphia Publisjhing (1995).

Chapter Five

Ellipsometric Studies of Rhodamine 6G

5.1 Introduction

The dye molecule Rhodamine 6G has frequently been studied by SHG, due to the presence of absorptions near the fundamental and second harmonic wavelengths of a Nd- YAG laser in its UV -visible spectrum. This will be covered in greater detail in chapter 6. However, these absorptions are also of interest in ellipsometry, as a wavelength scan of the parameters Δ and ψ, shows markedly changing behaviour in the wavelength range 400 - 700 nm.

Rhodamine 6G (R6G) is a positively charged organic molecule (Figure 5.1). Chloride is the most common counter ion and is used for this work. The molecule has approximate C_{2v} symmetry and the extensive π - electron system forces the molecule to be planar.

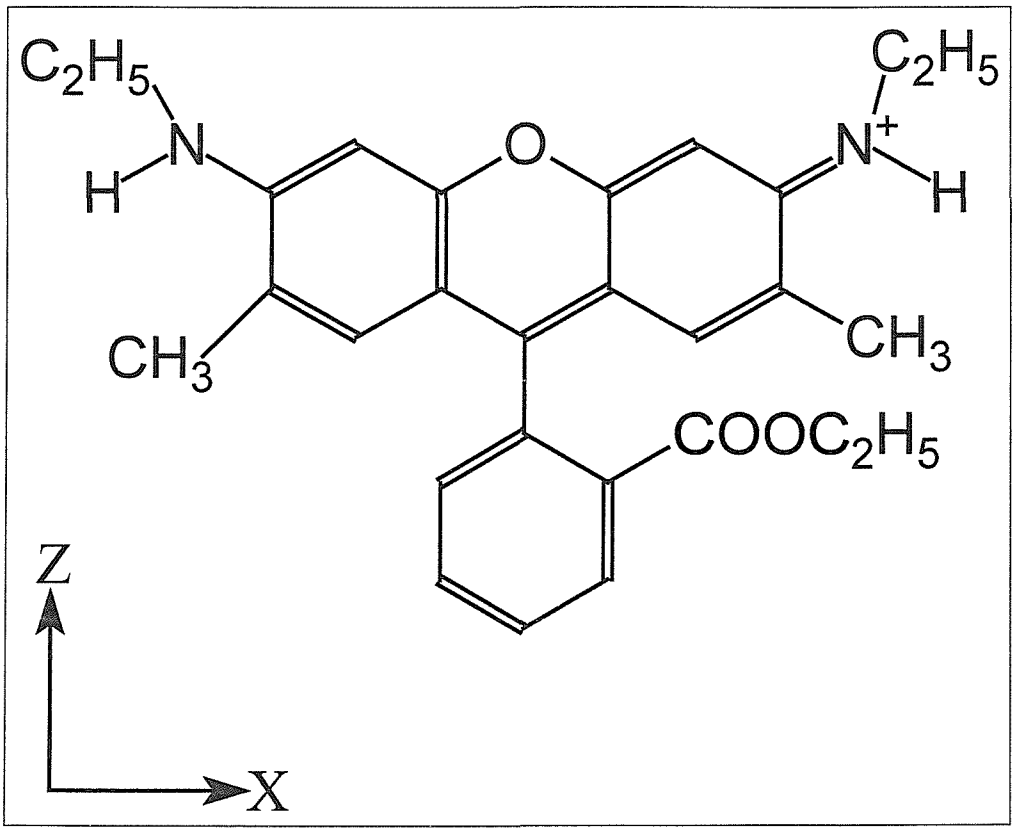

Figure 5.1 The R6G molecule indicating the molecular axis

The main chromophore in R6G is due to the larger of the two aromatic ring systems. These give rise to two sharp peaks in the UV-Vis. spectrum of R6G at 529nm and

347nm (Figure 5.2). The smaller aromatic ring contributes mainly to the broad adsorption band observed below 300nm.

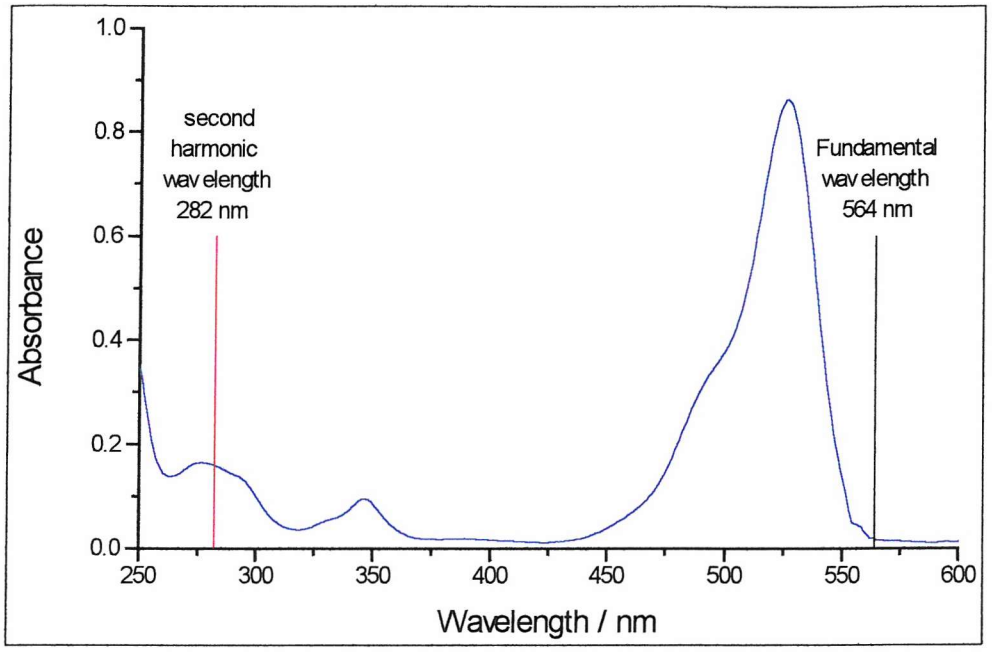

Figure 5.2 **UV-Vis spectrum of 0.87 μM R6G in water (S. Haslam). Also indicated are the fundamental and second harmonic wavelengths used in the experiment.**

The peak at 529nm is identified as an $S_0 \rightarrow S_1$ transition and the 347nm peak is the $S_0 \rightarrow S_2$ transition.

5.2 Experimental

Ellipsometric data were collected for $R6G^+Cl^-$ (BDH Indicators) at incident angles just above and below the Brewster angle of water (53.18° at 529nm), with particular reference paid to the wavelength region around the S_1 absorption peak at 525nm. n and k were calculated for film thicknesses between 50 and 100Å using the Filmfit package (R. Greef).

The ellipsometric measurements were taken using the experimental method given in section 3.2. Δ and ψ were measured in the range 400-700nm and two sets of measurements were taken for the R6G chloride solution:

1) Constant concentration (10μM), at angles of incidence at 1° intervals between 52° and 55° (the Brewster angle for water is 53.7°).

2) Constant angles of incidence (51°, 56°), at concentrations 0.2, 1, 2, 5, 10 and 20μM. UV Spectra were also measured for each of these concentrations in order to obtain the extinction coefficient.

By using a single film model, with water as the substrate, n and k were calculated using a Fortran program (R. Greef) for films with thicknesses varying between 10 and 150Å.

The refractive index of R6G as a substrate was obtained by measuring Δ and ψ for a splash of concentrated chloride solution, which dried on a microscope slide.

5.3 Results

5.3.1 UV Spectroscopy

The UV spectra of solutions of R6G, with concentrations varying between 0.2 and 20μM are shown in figure 5.3

The data were internally consistent, leading to a Beer-Lambert graph of absorbance against wavelength; the extinction coefficient for the S_1 peak at 525nm after a linear regression fit was $74671 M^{-1}cm^{-1} \pm 540$ ($r^2 = 0.9995$). This is high compared to literature values of $1\text{-}2X10^4 M^{-1}cm^{-1}$

The extinction coefficient α is linked to k by the formula:

$$k = \frac{\lambda}{4\pi}\alpha \qquad \textbf{Equation 5.1}$$

where λ is the wavelength of the incident light and $\alpha = [R6G]\varepsilon$.

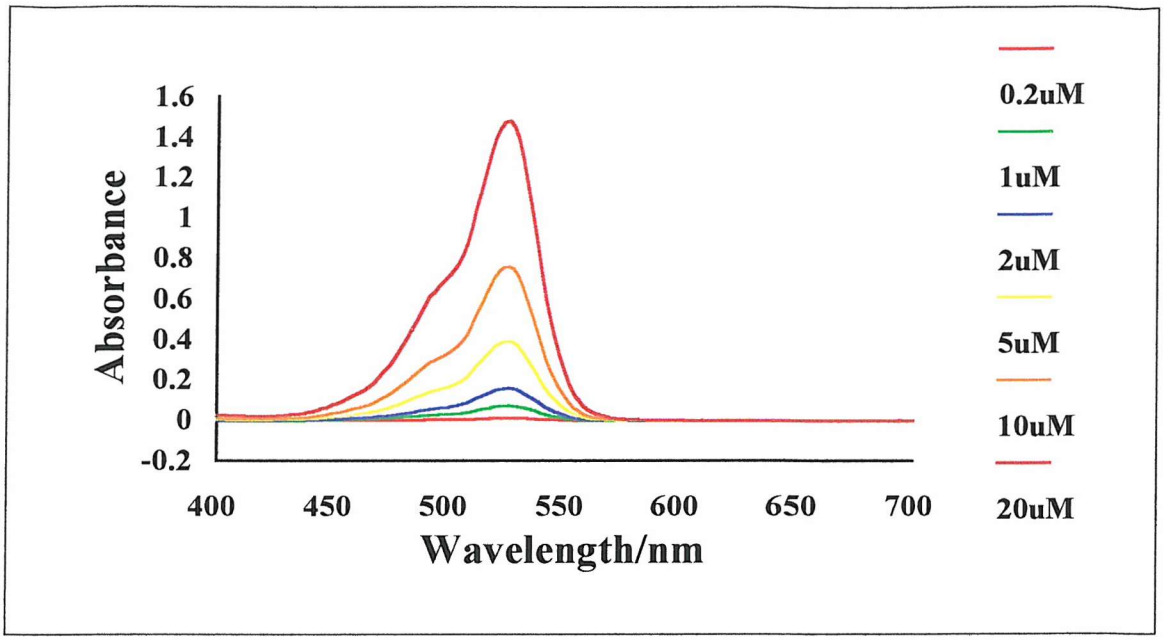

Figure 5.3 UV Absorption Spectra for R6G for concentrations from 0.2 to 20μM

5.3.2 Ellipsometry

The refractive index of concentrated R6G solution was measured using an Abbye refractometer, giving a value of n of 1.342, compared to that of water, which was 1.333. However, this fails to give a value for k, which is significant in regions where the absorbance is non-zero (i.e.330-580nm).

Constant concentration data are presented in Figures 5.4-5.5 with fits in Figures 5.6-5.11. Constant angle data are shown in Figures 5.12-5.13 for $\phi = 51°$ and Figures 5.14-5.15 for $\phi = 56°$. The solid substrate on the microscope slide is given in for $\phi = 51°$ and Figure 5.14-5.15 for $\phi = 56°$.

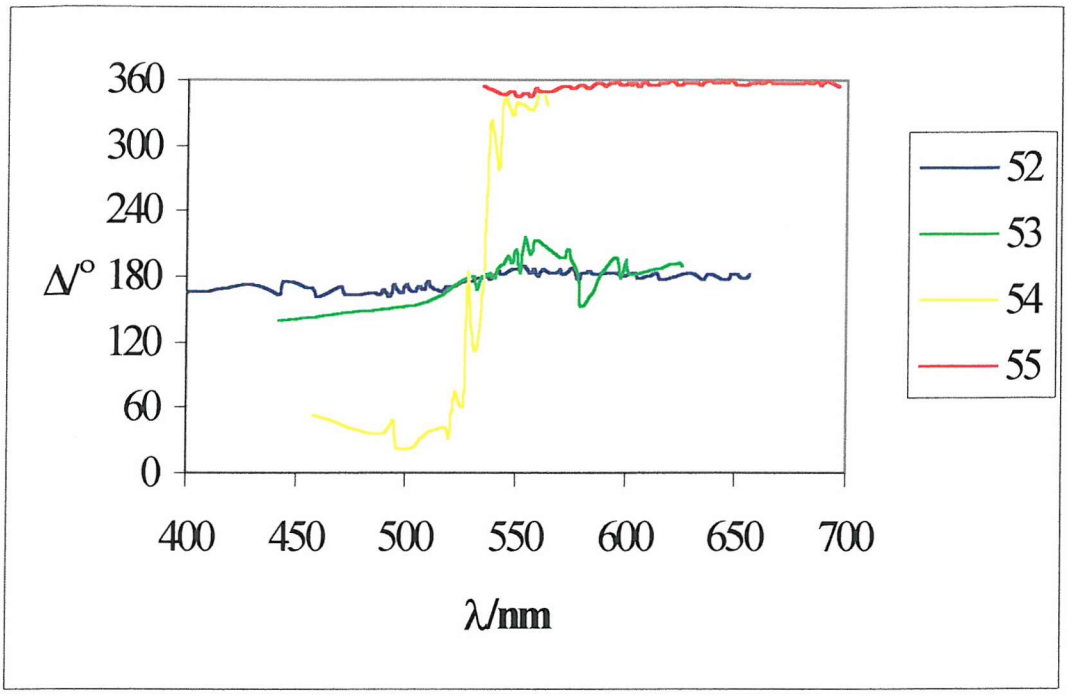

Figure 5.4 **Ellipsometry of 20μM R6G near the Brewster Angle: Graph of Δ against wavelength for angles of incidence 52°, 53°, 54° and 55°.**

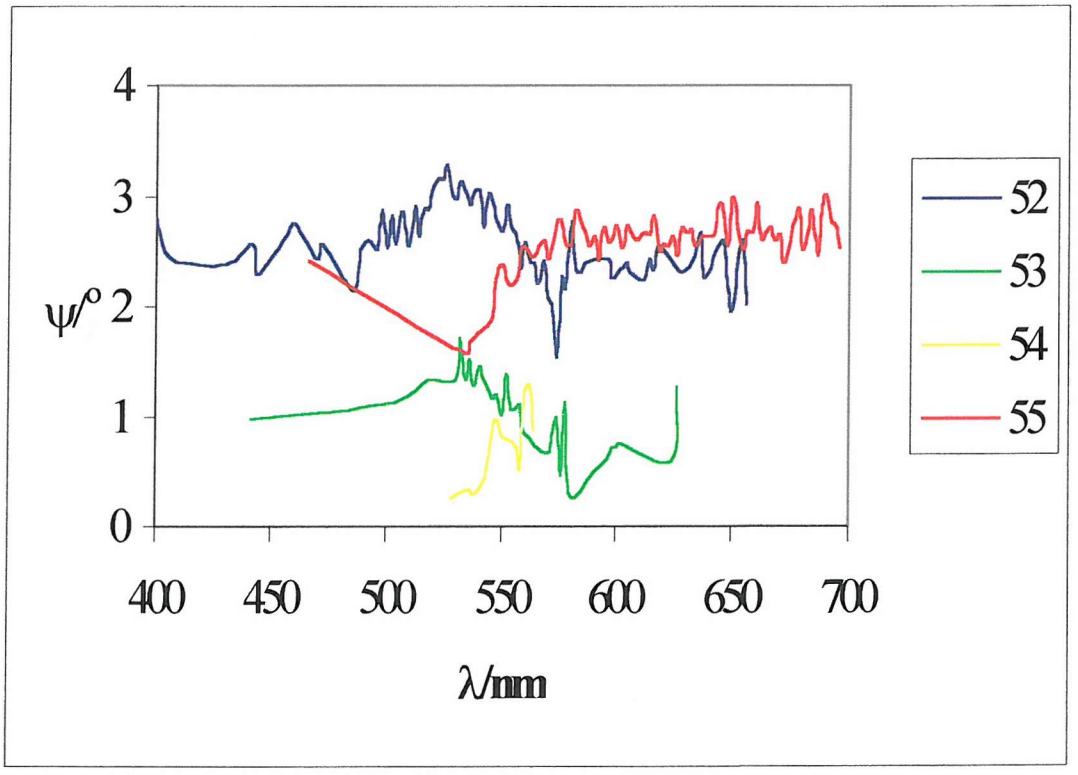

Figure 5.5 **Ellipsometry of 20μM R6G near the Brewster Angle: Graph of ψ against wavelength for angles of incidence 52°, 53°, 54° and 55°.**

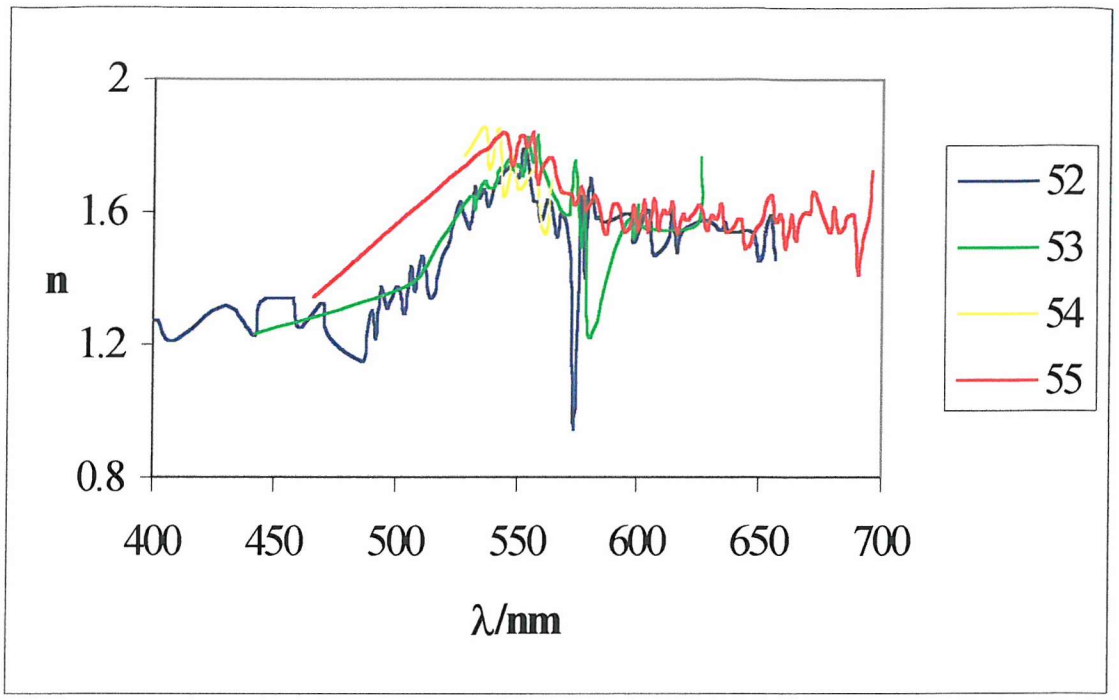

Figure 5.6 **Ellipsometry from 20μM R6G, for angles of incidence, ϕ = 52–55°. n calculated for a film 10Å thick.**

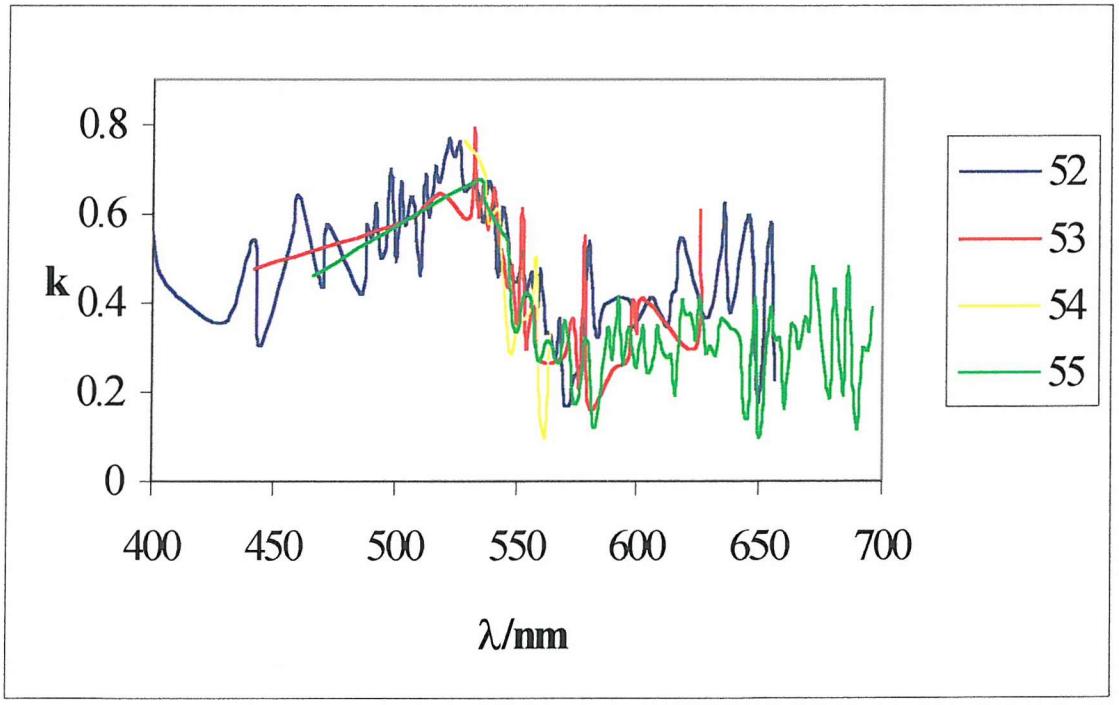

Figure 5.7 **Ellipsometry from 20μM R6G, for angles of incidence, ϕ = 52–55°. k calculated for a film 10Å thick**

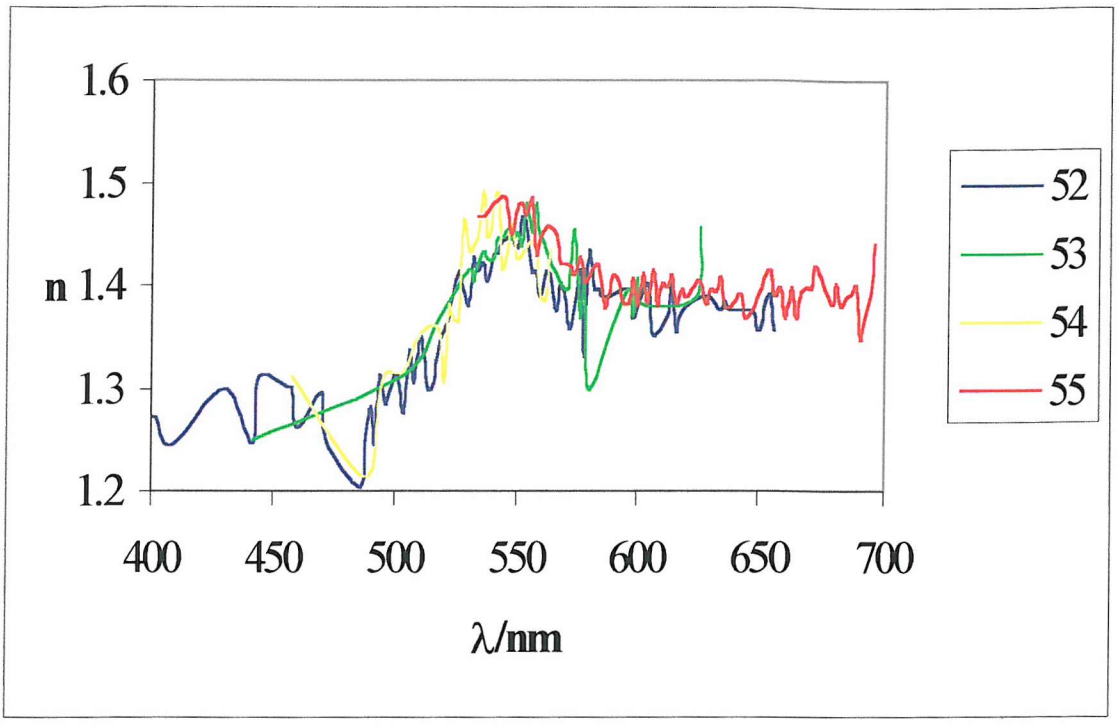

Figure 5.8 **Ellipsometry from 10μM R6G, for angles of incidence, ϕ = 52–55°. n calculated for a film 50Å thick**

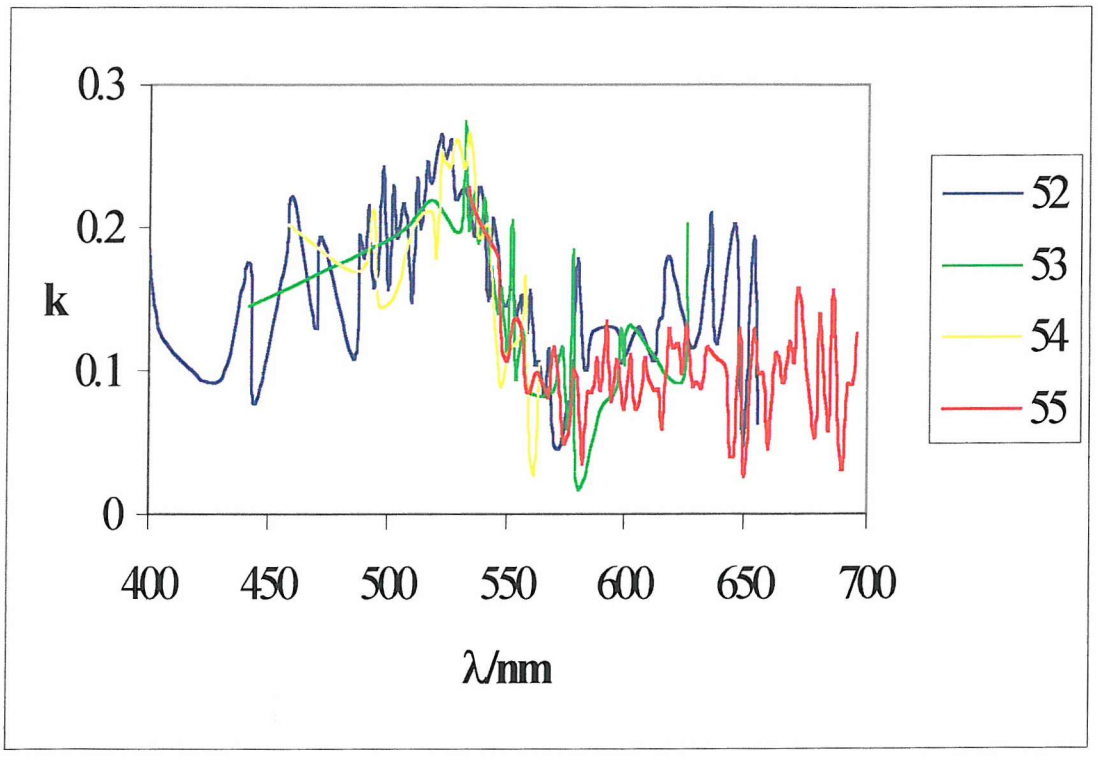

Figure 5.9 **Ellipsometry from 10μM R6G, for angles of incidence, ϕ = 52–55°. k calculated for a film 50Å thick**

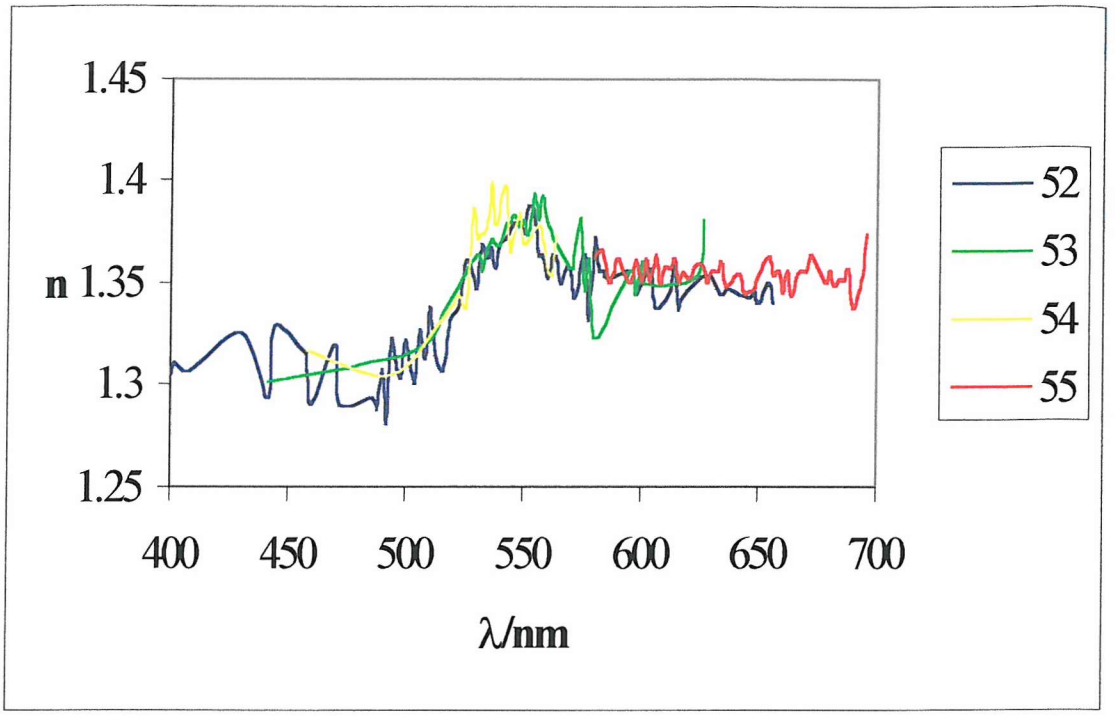

Figure 5.10 **Ellipsometry from 10μM R6G, for angles of incidence, ϕ = 52–55°. n calculated for a film 150Å thick**

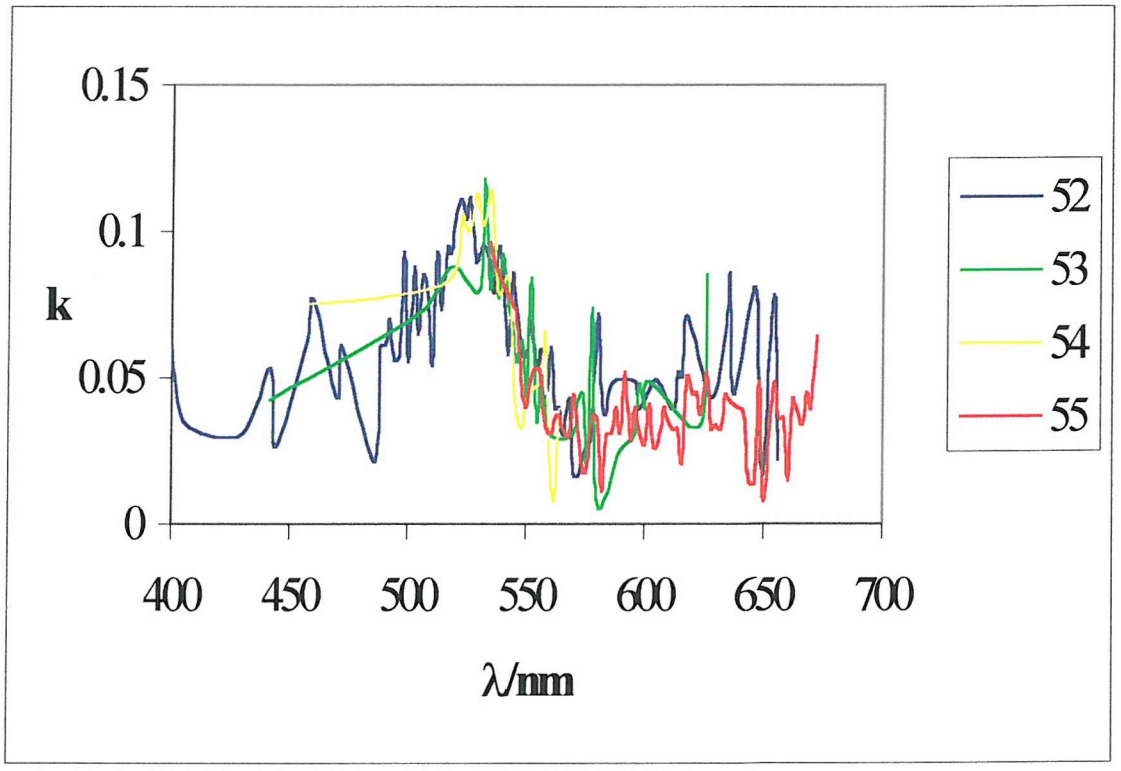

Figure 5.11 **Ellipsometry from 10μM R6G, for angles of incidence, ϕ = 52–55°. k calculated for a film 150Å thick**

5.3.2.1 Constant Concentration

The plots of Δ and ψ vs. λ change dramatically as the angle of incidence passes through the Brewster angle. As expected, Δ varies from close to 180° at angles below the Brewster angle to 0° or 360° above the Brewster angle. Below 53.7°, Δ changes from just below 180° to just above as the wavelength passes through the S_1 absorption at 525nm. Similarly in the plots for 54° and 55°, Δ changes from just above 0° below the S_1 absorption to just below 360° at higher wavelengths.

However, when the values for n and k are calculated, within experimental error they are constant with angle of incidence for all thicknesses above 10Å. We would expect this as n and k are physical properties of the material, whereas Δ and ψ are merely experimental measurements, which are susceptible to change as the angle of incidence changes relative to the Brewster angle.

Very few values of n and k are calculated for wavelengths below the absorption peak. This is because the fitting package is unable to accept values of n less than 1. We would expect such values because of the presence of anomalous dispersion which leads to a large discontinuity in refractive index as the wavelength passes through an absorption band.

As the proposed thickness of the film increased, the variation in the values of n and k decreased and the value of n tended towards the value of 1.342 measured by the Abbe Refractometer. This corresponds to behaviour of R6G alone, with minimal contribution from the water beneath.

So, the constant values of n and k at film thicknesses support the following conclusion:

> *In solution, R6G successfully supports an ellipsometric model of a single film on a water substrate, with a film thickness of not less than 10 Å.*

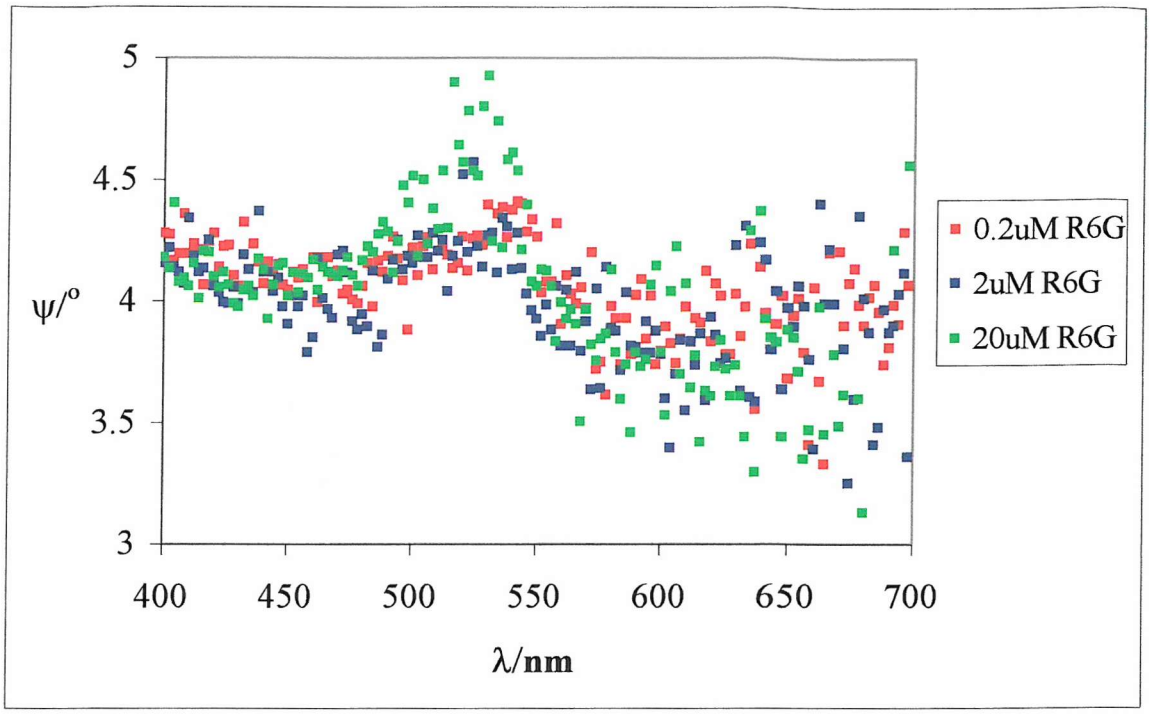

Figure 5.12 Ellipsometry from R6G at $\phi = 51°$. ψ vs λ for concentrations 0.2, 2 and 20μM.

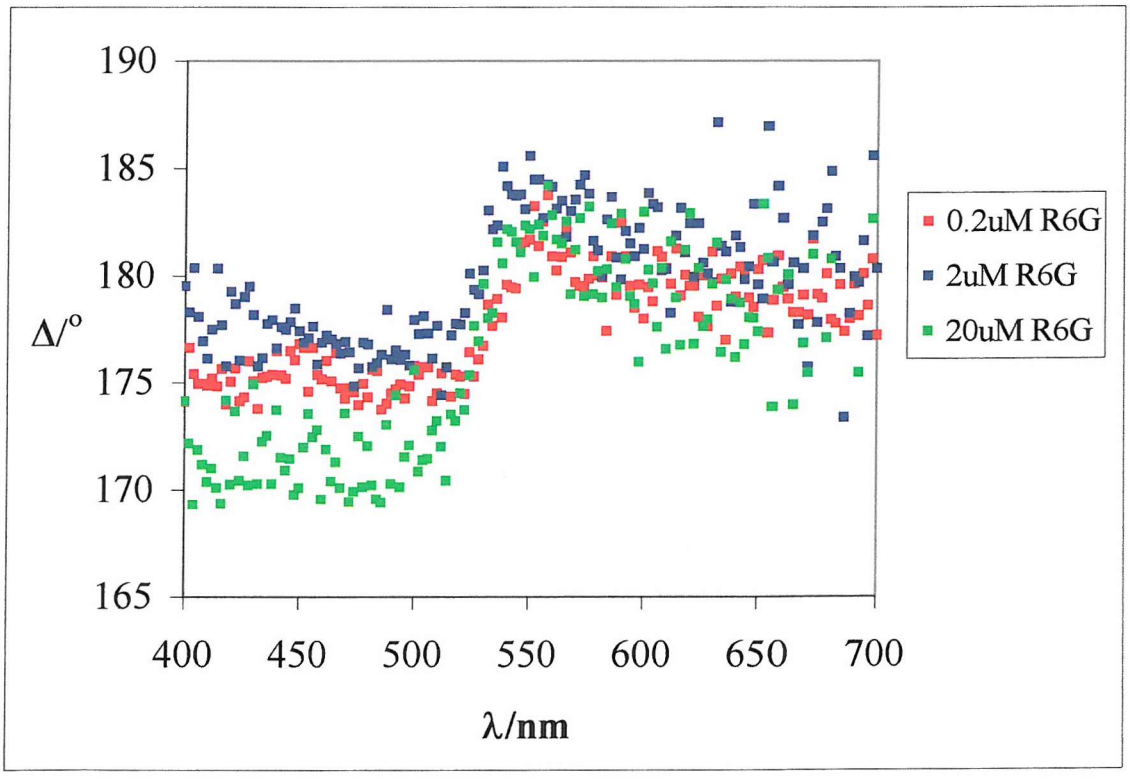

Figure 5.13 Ellipsometry from R6G at $\phi = 51°$. Δ vs λ for concentrations 0.2, 2 and 20μM.

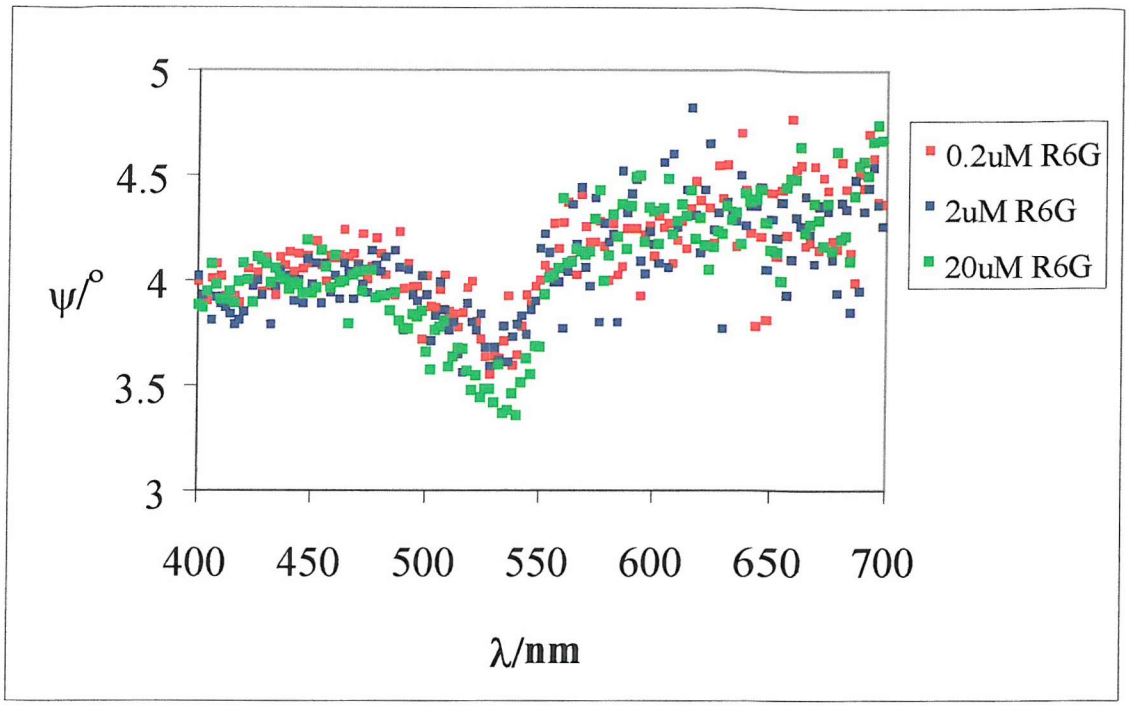

Figure 5.14 **Ellipsometry from R6G at $\phi = 56°$. ψ vs λ for concentrations 0.2, 2 and 20μM.**

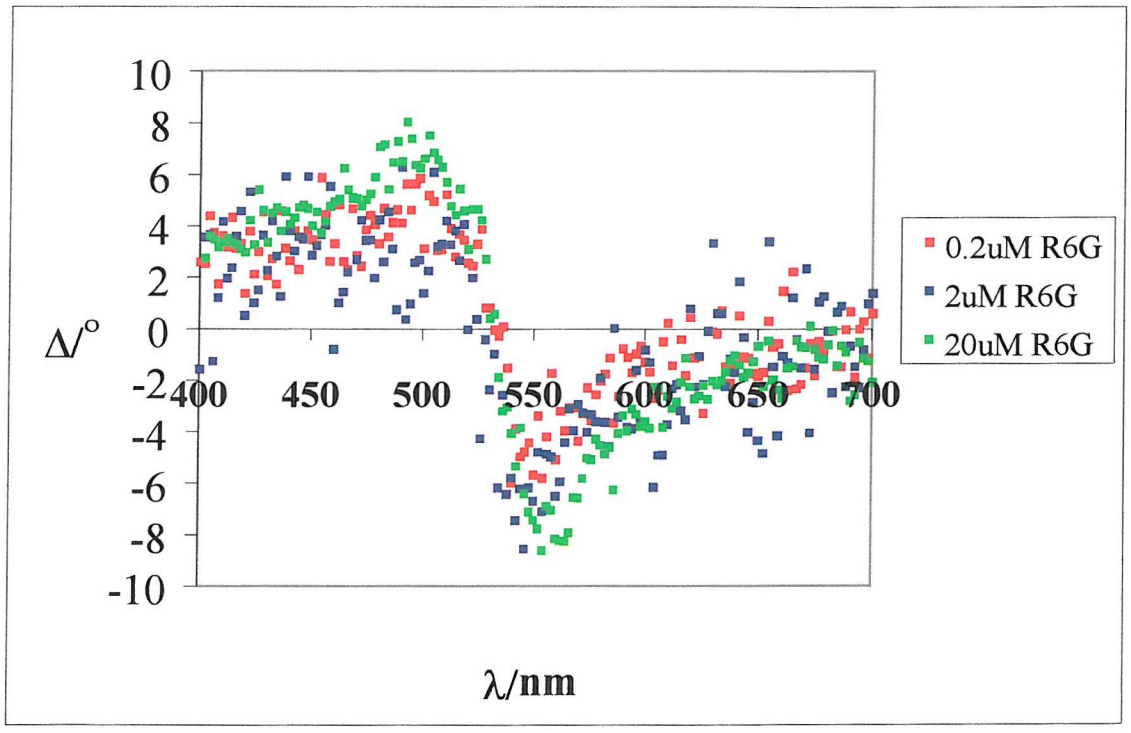

Figure 5.15 **Ellipsometry from R6G, for $\phi = 56°$. Δ vs. λ for 0.2, 2 and 20μM R6G.**

5.3.2.2 Constant Angle of Incidence

As with the constant concentration data (Section 5.3.2.1), the plots of Δ and ψ vs. λ again change dramatically as the angle of incidence passes through the Brewster angle. Graphs are plotted for concentrations of 0.2, 2 and 20 μM solutions of R6G. As concentration increases, the peaks in the Δ and ψ plots are found to become more pronounced, again because the interface begins to resemble a purely R6G surface.

Fitted values of n and k are again subject to a discontinuity at the absorption wavelength. Again this can be attributed to anomalous dispersion. The values for n and k obtained after input of various film thicknesses (from 10-1000Å) again support the conclusion:

In solution, R6G successfully supports an ellipsometric model of a single film on a water substrate, with a film thickness of not less than 10 Å.

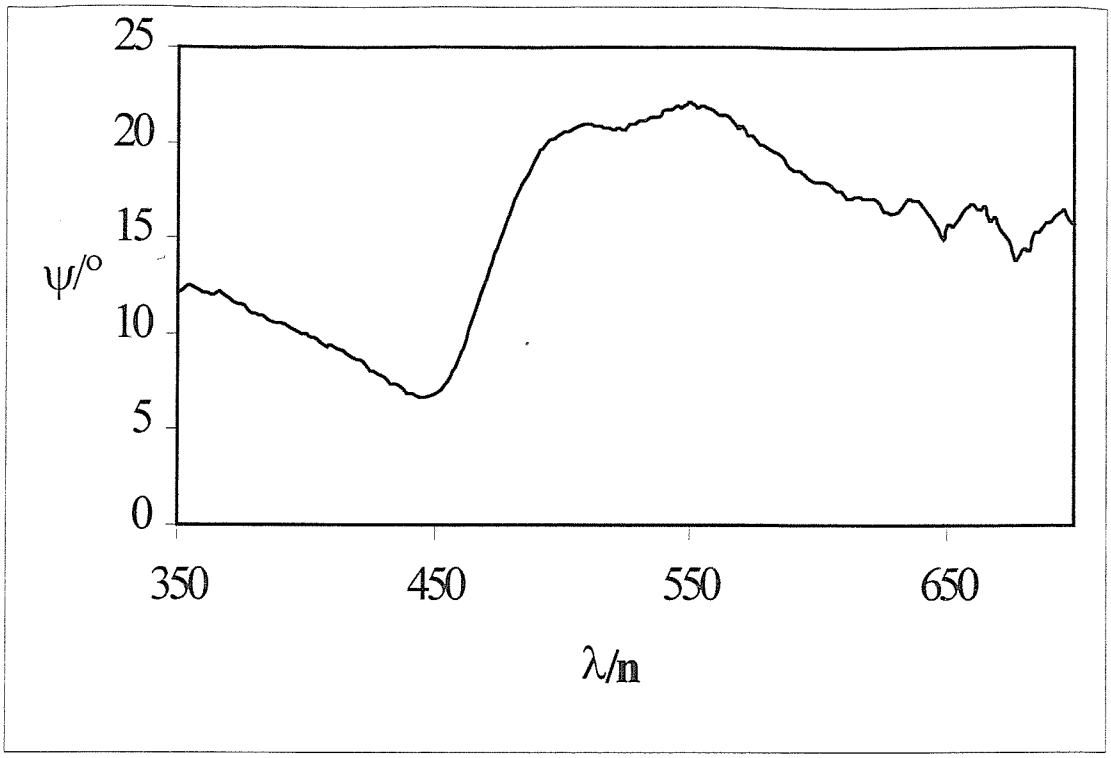

Figure 5.16 **Ellipsometry from R6G on Glass, for $\phi = 51°$. ψ measured for solid film created by evaporation of 10μM solution.**

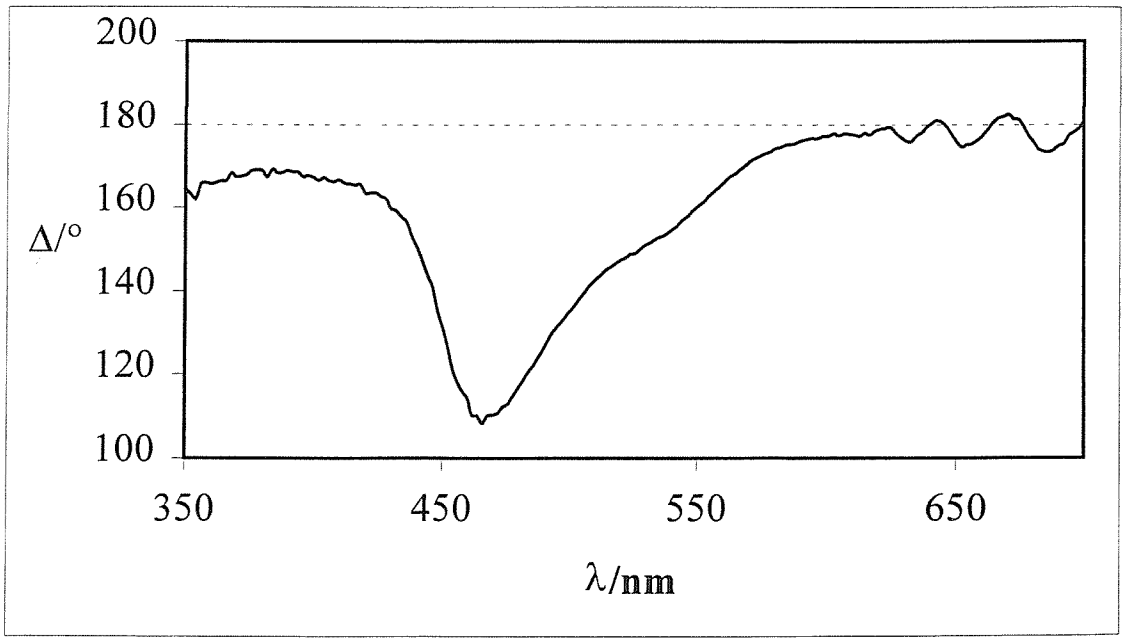

Figure 5.17 **Ellipsometry from R6G on Glass, for $\phi = 51°$. Δ measured for solid film created by evaporation of 10μM solution.**

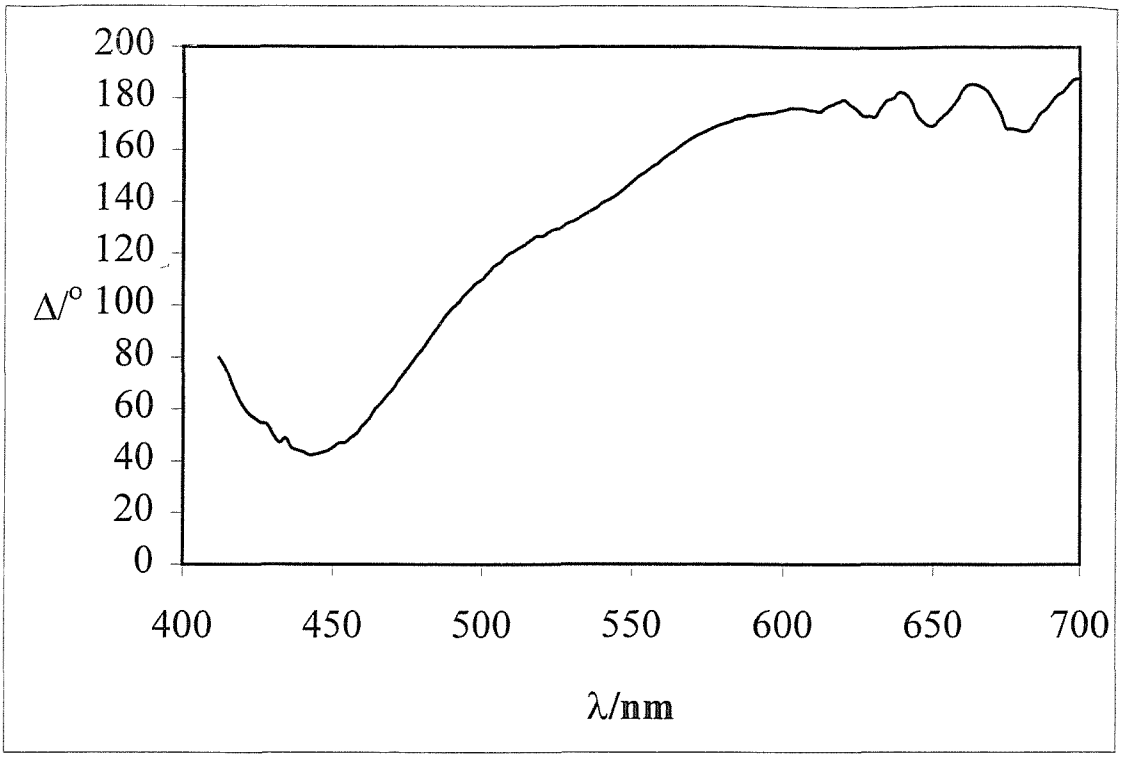

Figure 5.18 Ellipsometry from R6G on Glass, for $\phi = 56°$. Δ measured for solid film created by evaporation of 10μM solution.

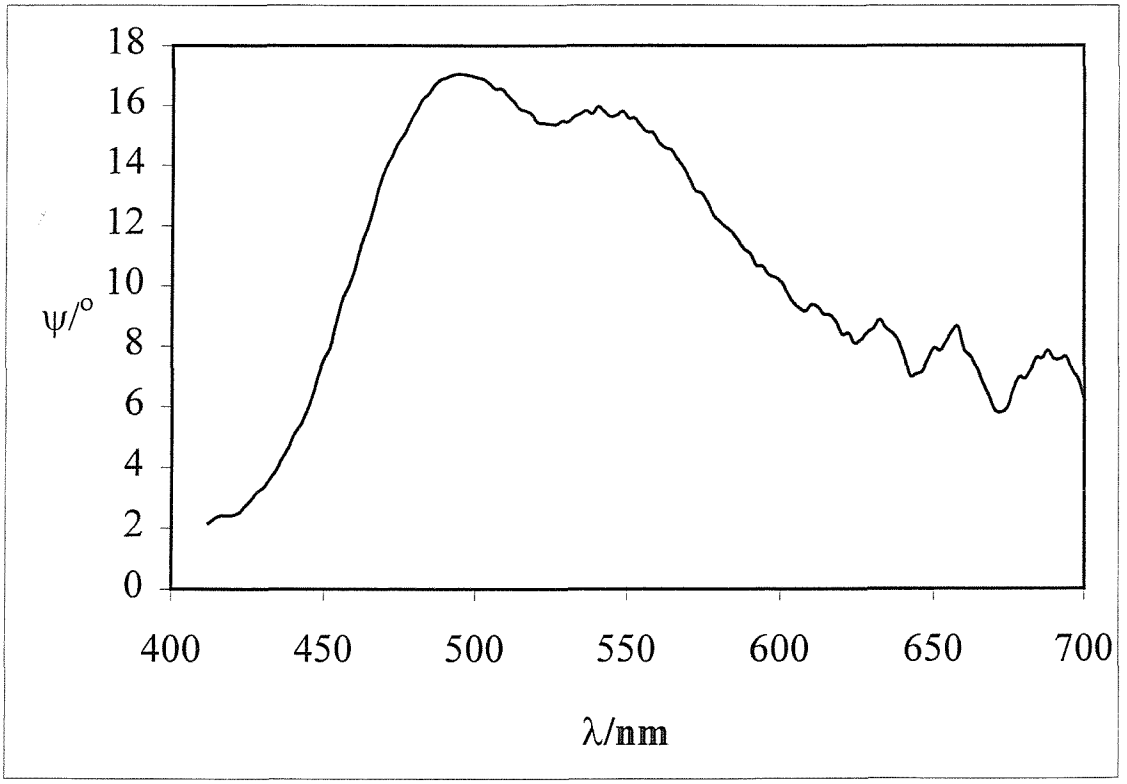

Figure 5.19 Ellipsometry from R6G on Glass, for $\phi = 56°$. ψ measured for solid film created by evaporation of 10μM solution.

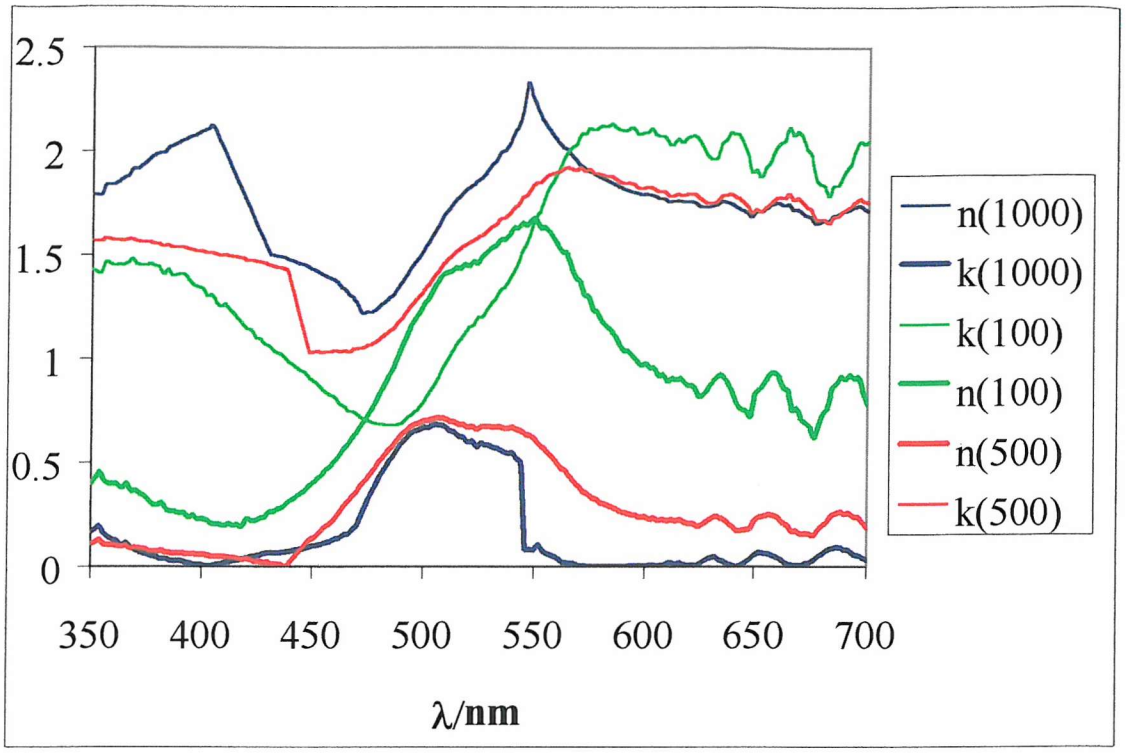

Figure 5.20 Ellipsometry from R6G on Glass, for angles of incidence, $\phi = 51°$. n and k calculated for solid film of thickness 100, 500 and 1000Å.

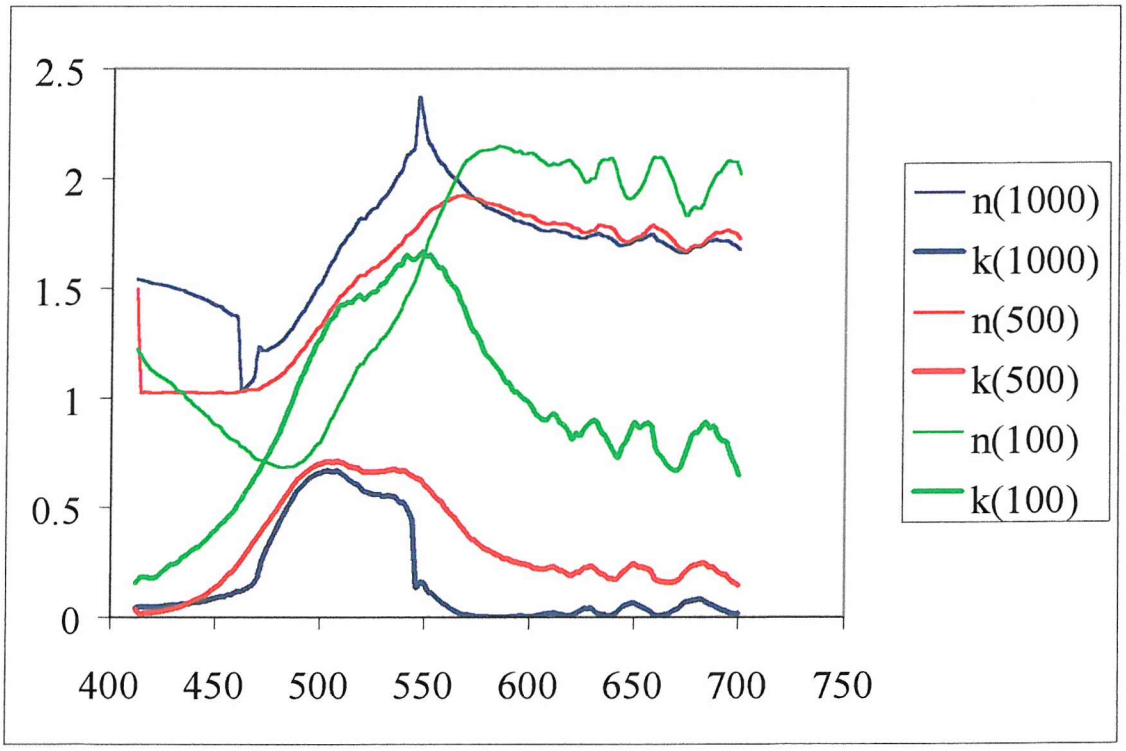

Figure 5.21 Ellipsometry from R6G on Glass, for angles of incidence, $\phi = 57°$. n and k calculated for solid film of thickness 100, 500 and 1000Å.

5.3.2.3 10μM Film deposited on Glass.

As expected, the plots of Δ and ψ vs. λ (Figures 5.16-5.19) are much smoother than for the liquid surface (which was due to liquid surfaces susceptibility to external vibration). The results are similar in that Δ varies from close to 180° at angles below the Brewster angle to 0° or 360° above the Brewster angle. Again, for the 51° plot, Δ changes from just below 180° to just above as the wavelength passes through the S_1 absorption at 525nm. Similarly in the plot for 57°, Δ changes from just above 0° below the S_1 absorption to just below 360° at higher wavelengths. Also, at high wavelength, the value of Δ clearly oscillates between below 180° and above 180°. This may be due to Fabry-Perot interference.

This time the sets of data were fitted against a substrate of bk7 for thicknesses of 100, 500 and 1000Å (Figures 5.20-5.21), and for a fixed thickness, the values of n and k were consistent for angles of incidence above and below the Brewster Angle. Fits were again possible for thicknesses greater than 10Å, although they varied sharply with film thickness. For example, the real part of the refractive index for thicknesses of less than 200Å was less than 1, which is due to anomalous dispersion occurring as the absorption was approached. As this work considers R6G concentration at less than monolayer thickness for concentrations of 0.2μM,

So, the constant values of n and k at fixed film thicknesses support the following conclusion:

> *A deposition of 10mM R6G on glass successfully supports an ellipsometric model of a single film with a film thickness of not less than 10 Å.*

Chapter Six

SHG and SHE Studies from Liquid Surfaces

6.1 Experimental

Surface second harmonic generation (SHG) measurements were carried out on water and R6G at the water/air interface using 45° input plane polarised light with the second harmonic measured at 0° (P) and 90° (S) output polarisations. The ratio I(45-P)/I(45-S) was compared to previous results (Refs. 6.1-6.2).

The same systems were examined using SHE. For the wavelength scan, at least three measurements were taken for each wavelength in the range 278-290nm. The concentration dependent measurements were taken for R6G at 282nm for concentrations of 0.2, 2, 5, 10 and 20μM.

In all cases care was taken to remove the surface layer of the liquid sample, in order to remove any organic impurities from the water supply (Purite, $\rho > 17.5 M\Omega cm^{-1}$). The laser beam power before the surface was measured using a Gentec power meter. The visible incident intensity was maintained at a constant value of 4.0 ± 0.2 mJ pulse^{-1} for water. However, for R6G, previous results (Ref. 6.2) showed that the power should be limited to 0.35 ± 0.1 mJ pulse^{-1}, by attenuating the fundamental using a double Fresnel rhomb placed before the incident polariser.

6.2 Water

The data for water is presented in Figure 6.1 and Table 6.1. The SHG intensity never rose above background levels for s-polarised input radiation, which is in agreement with results from Fordyce. As a result, it is impossible to measure Δ and ψ values for s input radiation. Definition of Δ around $\psi = 0°, 90°$ is markedly diminished, due to the wide variation in tan ψ around these angles.

When water was investigated by SHE, the value of ψ ($53.1 \pm 3°$) was close to the value of $47.0° \pm 5°$ obtained by Fordyce et al (Ref. 6.3). However, in this experiment, with every combination of input and output polarisations tried, Δ was found to be $21.29 \pm 2.0°$. This was clearly non-zero, indicating the presence of a circular component in the

output radiation. This value was small enough to remain unobserved in the SHG technique, indicating that SHE has the advantage of much enhanced resolution.

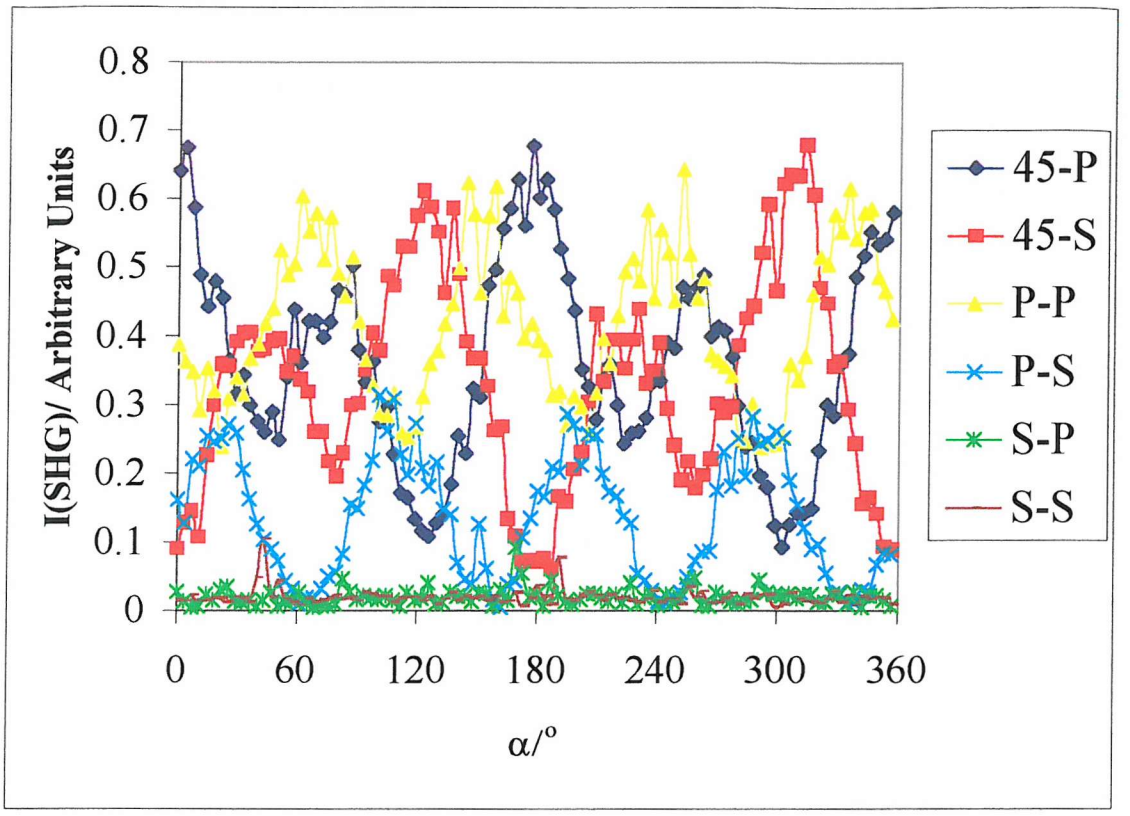

Figure 6.1 SHE from Water. I(SHG) vs Q for six Polarisation Combinations

Polariser Angle/°	Analyser Angle/°	Δ/°	ψ/°	Max I(SHG)/ a.u.
45	P (=0)	20.667 ≈ Δ	53.133 ≈ ψ	50
-45	P	201.49 ≈ Δ+180	53.119 ≈ ψ	50
45	180	18.486 ≈ Δ	48.514 ≈ ψ	50
45	S (=90)	200.27 ≈ Δ+180	34.619 ≈ 90-ψ	50
P	P	159.06 ≈ 180-Δ	86.575 ≈ ψ+45	30
P	S	334.13 ≈ 360-Δ	1.361 ≈ ψ-45	25
S	P	undefined	undefined	≈0
S	S	undefined	undefined	≈0
Right Circular	P	123.12 ≈ Δ+90	42.27 ≈ ψ_c	12
Left Circular	P	290.43 ≈ Δ-90	41.12 ≈ ψ_c	13

Table 6.1 SHE from Water - Δ and ψ for various polarisation combinations

The non-zero Δ value was found to revert to zero when nitrogen was bubbled through the sample. It was thought that the presence of dissolved oxygen in the sample could have caused this anomaly. However it is now known that miniscule amount of an unidentified organic impurity was sufficient to cause such a large deviation in the Δ value. This was not detected by the traditional method (i.e. surface tension measurements remained normal at 72.0mNm^{-1}). However, on replacement of the water supply's filters (Purite), the value of Δ reverted to zero.

6.3 Rhodamine 6G

The strength of the $S_0 \rightarrow S_1$ resonance is the reason that the Rhodamine family of laser dyes are in common use since it is an excellent match for the second Nd^{3+}:YAG harmonic at 532nm. The R6G molecule is photochemically stable under repeated excitation giving enhanced dye laser performance. These qualities also make the R6G molecule ideal as a probe molecule for study at the watr/air interface. The green fundamental light is on the edge of the $S_0 \rightarrow S_1$ resonance (529nm) and there is also resonance with the second harmonic light at 278-290nm (Figure 5.2). The double resonantly enhanced second harmonic signal will therefore be very large giving the desired high signal / noise ratio.

R6G has been studied absorbed to silica by Heinz *et. al.* (Ref. 6.4), where the orientation of the R6G and its second order nonlinear polarisability at resonance were deduced. The photochemistry of R6G on quartz was investigated by Meech and Yoshihara (Ref. 6.5) using a 532nm fundamental beam.

6.3.1 Second Harmonic Generation

For input radiation of 560nm, a wavelength scan of the output radiation revealed that only background intensity was observed outside the wavelength range 318-322nm. This proved that second harmonic generation was being observed. If a long tail of non-zero

intensity was observed at higher wavelengths, two-photon fluorescence may have been responsible.

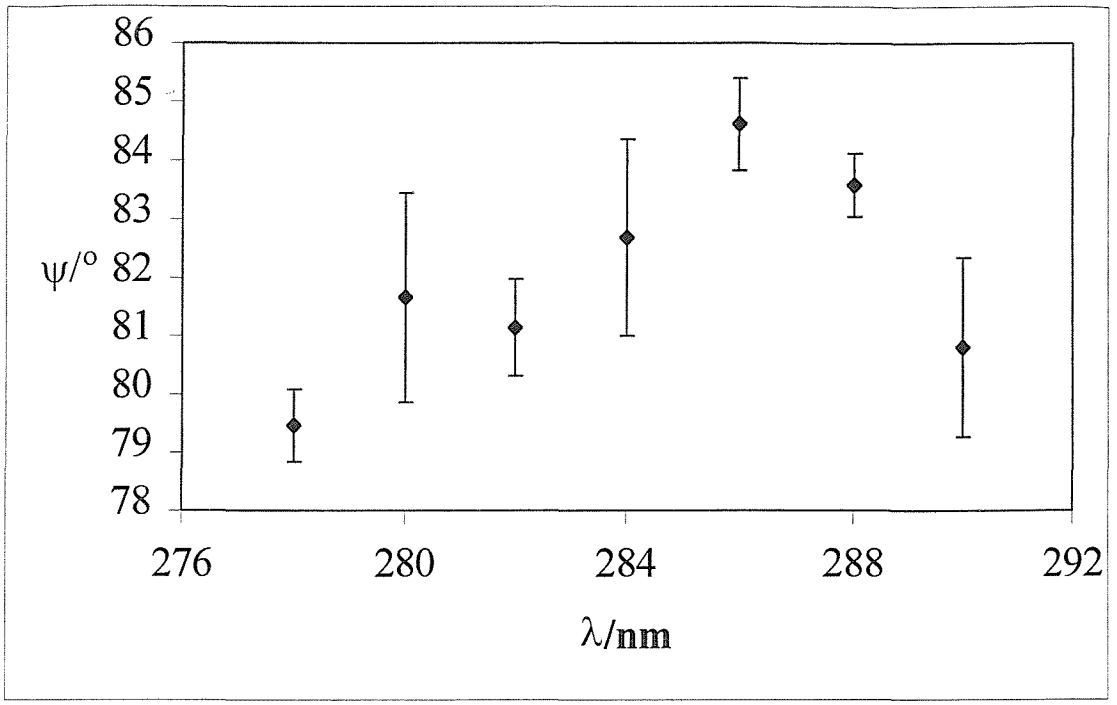

Figure 6.2 **SHE from 10μM R6G: ψ vs λ**

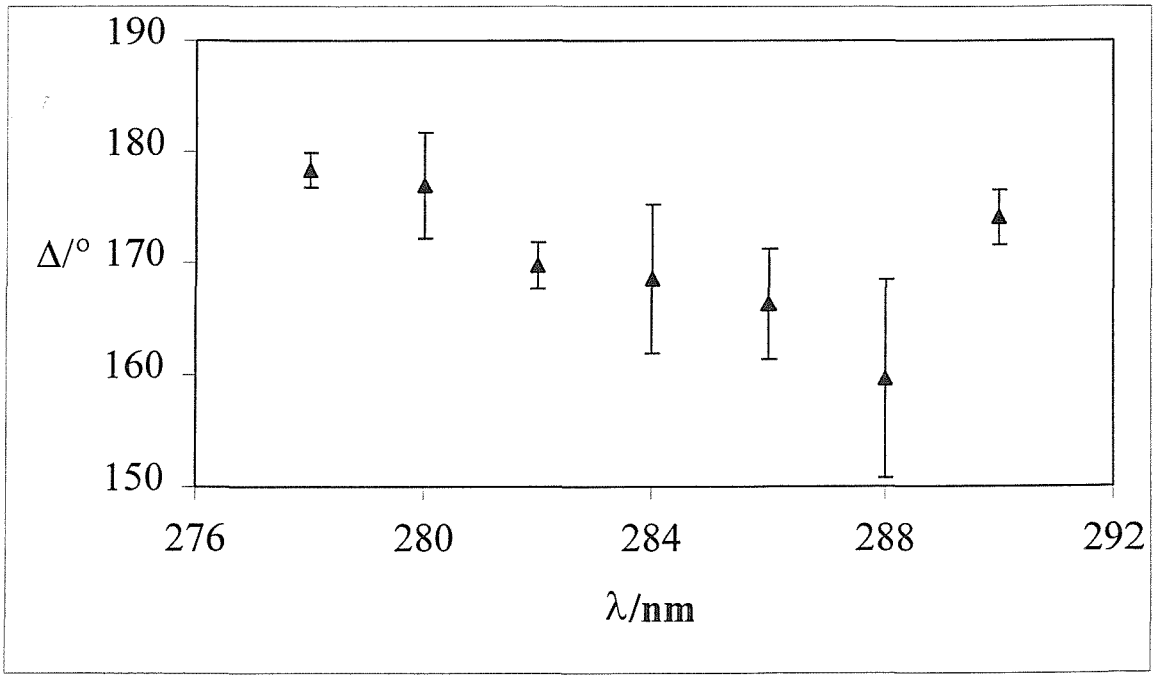

Figure 6.3 **SHE from 10μM R6G: Δ vs λ**

6.3.2 Comparison of SHG and SHE

The values of ψ are calculated from SHG (Ref 6.4) using the quotient of the I(45-P) and I(45-S) intensities.

Sample	ψ calculated from SHG /° $\tan^2 \psi = \frac{I(45-P)}{I(45-S)}$	ψ calculated from SHE /° $\psi = \tan^{-1}\left(\frac{r_p}{r_s}\right)$
10 μM R6G	72.3 ± 4	75.7 ± 3
Water	47.0 ± 5	53.1 ± 3

Table 6.2 Comparison between SHG (Refs 6.2-6.3), calculated from two measurements, and SHE (one measurement, also providing phase difference) for 10μM Rhodamine 6G and water at 282nm

Both values in table 6.2 give good agreement with the values calculated by SHG. The fact that the SHG experiments (Refs 6.2-6.3) were carried out at an angle of incidence of 60°, whereas SHE experiments were carried out at an angle of incidence of 70°, may account for the difference in values obtained. SHE only requires one measurement and also give the phase angle. 6 measurements are required for SHG to get less information about the polarisation state of the molecule.

One of the problems with SHG harmonic fit is that it can't differentiate between the ψ-equivalent values +45° and -45° and therefore cannot determine Δ with any certainty. This gives an incomplete picture of the polarisation state of the molecules at the surface, in particular for resonant systems. SHE tells this immediately as a value of Δ between 90° and 270° indicates that the sign of ψ is –ve whereas $0° < \Delta < 90°$ or $270° < \Delta < 360°$ indicates that $\psi > 0$. In the case of R6G, we can tell that ψ is negative as Δ lies in the middle of the 90°-270° range, whereas for water the converse is true.

The fact that Δ and ψ change with concentration is in agreement with the work of Haslam *et. al.* (Ref. 6.2) and suggests that there is not just straight accumulation of material at the interface. As Δ approximates to zero for water and is markedly non-zero for R6G at the air/water interface, this elliptical behaviour must be due to the presence of R6G alone.

6.4 References

6.1 A.J. Fordyce, PhD Thesis, University of Southampton (1999).

6.2 S. Haslam, PhD Thesis, University of Southampton (1998).

6.3 A.J. Fordyce, W.J. Bullock, A.J. Timson, S.Haslam, R.D. Spencer-Smith, A.K. Alexander and J.G. Frey, Submitted for Publication (2000)

6.4 T.F. Heinz, C.K. Chen, D. Ricard and Y.R. Shen, *Phys. Rev. Lett.*, **48** (1982) 478.

6.5 S.R. Meech and K. Yoshihara, Photochemistry and Photobiology Vol. 53, No. 5, (1991), 627.

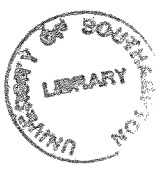

Appendix One

Units for χ_n

In the equation,

$$\mathbf{P} = \mu + \varepsilon_0(\chi_1\mathbf{E} + \chi_2\mathbf{EE} + \chi_3\mathbf{EEE} + ...) \qquad \textbf{Equation 1}$$

the quantities are often quoted with differing systems of units. These, and the conversions between them, are outlined in Table 1 below;

Unitary System	**SI**	**esu**	**cgs**
Electric field strength, **E**	Vm^{-1}	statvolt cm^{-1}	$cm^{-1/2}g^{1/2}s^{-1}$
Macroscopic nth order susceptibility, χ_n	$(mV^{-1})^{n-1}$	$(cm\ statvolt)^{n-1}$	$(cm^{1/2}g^{-1/2}s)^{n-1}$
Polarisation, **P**	Cm^{-2}	statvolt cm^{-1}	$cm^{-1/2}g^{1/2}s^{-1}$

Table 1 Conversion between unitary systems

Equations 2-4 show the relative magnitudes of the standard units

$$1\,statvoltcm^{-1} = 1cm^{-1/2}g^{1/2}s^{-1} = 3x10^4\,Vm^{-1} \qquad \textbf{Equation 2}$$

$$\chi_n(SI) \Big/ \chi_n(esu) = 4\pi \Big/ (10^{-4}c)^{n-1} \qquad \textbf{Equation 3}$$

$$P_n(SI) \Big/ P_n(esu) = 10^3 / c \qquad \textbf{Equation 4}$$

Appendix Two

SHE Studies from Boc-Trp-Trp

Introduction

Although insufficient data was collected on Boc-trp-Trpfor submission in the main part of the thesis, the results are interesting enough to be reported here for future reference.

Experimental

Surface second harmonic ellipsometry (SHE) measurements were carried out on 50μM Boc-Trp-Trp (pH2) at the water/air interface using 45° input plane polarised light with the second harmonic measured at 0° (P) output polarisation for each QWP angle. For the wavelength scan, at least three measurements were taken for each wavelength in the range 276-288nm.

Care was taken to remove the surface layer of the liquid sample, in order to remove any organic impurities from the water supply (Purite, $\rho > 17.5 M\Omega cm^{-1}$). The laser beam power before the surface was measured using a Gentec power meter. The visible incident intensity was maintained at a constant value of $0.35 \pm 0.1 mJ\ pulse^{-1}$, by attenuating the fundamental intensity using a double Fresnel rhomb placed before the incident polariser.

(t-butyloxycarbonyl)-tryptophan-tryptophan (Boc-Trp-Trp)

As Crawford et al have studied the second harmonic behaviour of (t-butyloxycarbonyl)-tryptophan-tryptophan (Boc-Trp-Trp) in depth (Ref. 1), this was a suitable molecule with which to commence study of liquid interfaces. There was sufficient previous work to compare results with, but also enough unanswered questions to require further study.

In order to discuss boc-trp-trp it is important to first understand several properties of its parent molecule, tryptophan. Tryptophan is one of twenty naturally occurring amino acids, which are characterised by the close proximity of an amine group and a

carboxylic acid group. This enables the hydrogen ion of the acid group to migrate to the nitrogen atom in the amine group, resulting in the formation of a zwitterion.

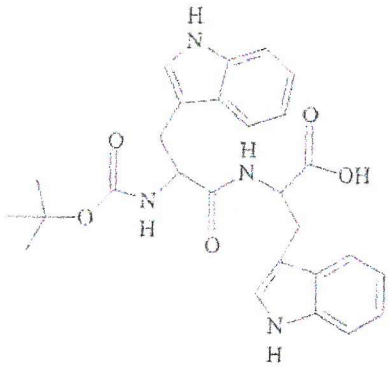

Figure 1 The Structure of Boc-Trp-Trp

Tryptophan absorbs strongly in the UV, suggesting that it may give SHG signals, indeed fingerprints (which contain amino acid residues) on glass were found to give second harmonic radiation upon excitation with lasers as early as 1964. Smiley and Vogel (Refs. 2-3) have extended this work to include the derivatives of tryptophan. Crawford et al who studied both tryptophan and Boc-Trp-Trp (Refs 1, 4) showed that in fact it was the latter molecule, which provided both the higher SHG intensity and the more marked chiral behaviour.

The fact that amino acids are chiral also means that their ellipsometric behaviour will be of particular interest. The aim of this work was to study the ellipsometric behaviour of Boc-Trp-Trp at UV wavelengths.

Results and Discussion

Sample graphs showing the behaviour of Δ and ψ against wavelength for the range 276-288nm are presented in Figures 2 and 3. The variation with wavelength is pronounced and further work needs to be done to map this more accurately. The results were reproducible over the course of a day but not from day to day, even though the sample was preserved in a refrigerator away from any bright light. Tests carried out by Prof. Mark Bradley showed that the sample was pure and that the day to day variation in results was not due to degradation of the sample.

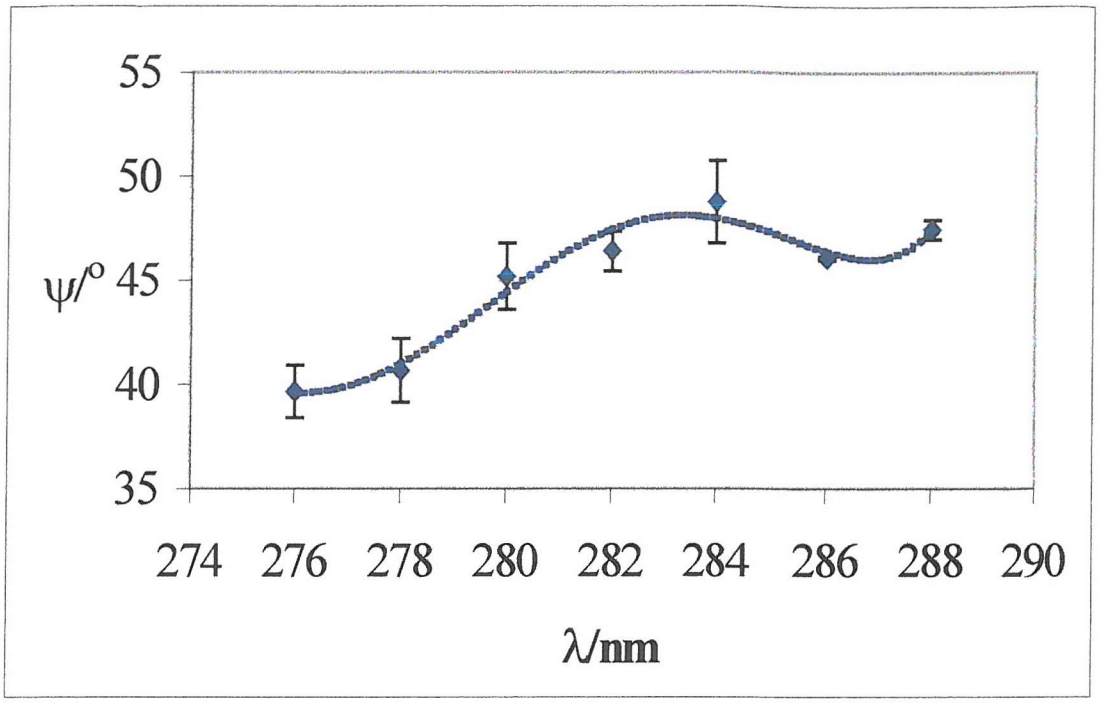

Figure 2 **SHE from 50μM Boc-Trp-Trp at pH2; ψ vs λ**

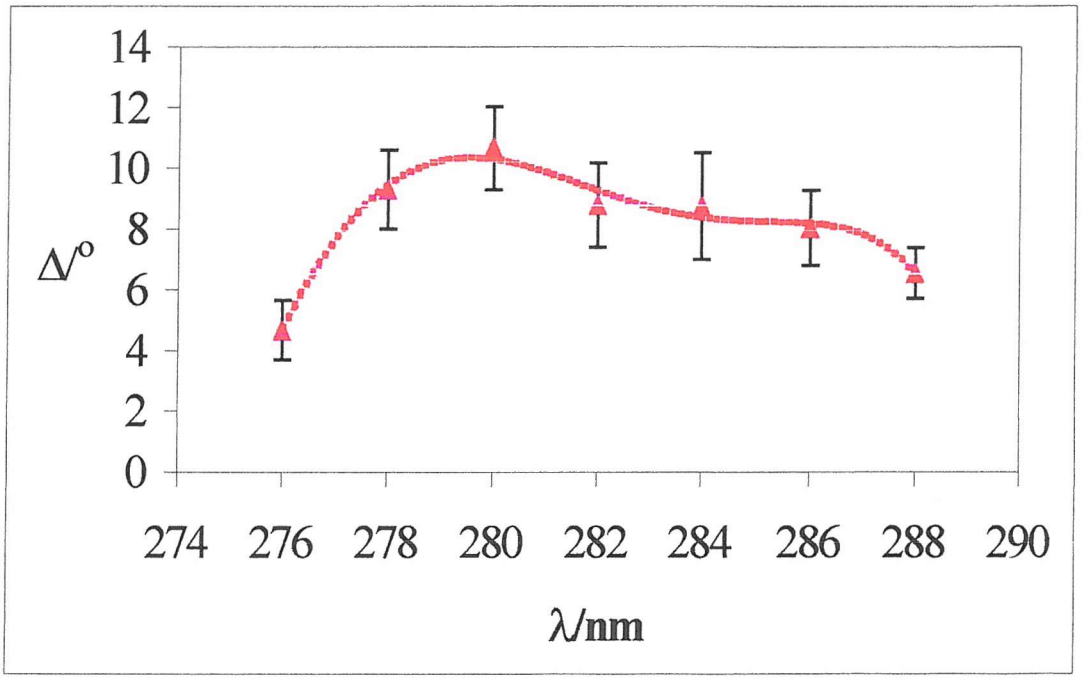

Figure 3 **SHE from 50μM Boc-Trp-Trp at pH2; Δ vs λ**

References

1. M. J. Crawford, S. Haslam, J. M. Probert, Y. A. Gruzdkov and J. G. Frey, *Chem. Phys. Lett.* **229** (1994) 260-264.
2. B.L. Smiley and V. Vogel, *J. Chem. Phys.* **103** (8) (1995) 3140-3144.
3. V. Vogel and B. L. Smiley, *SPIE Vol. 1922 Laser Study of Macroscopic Biosystems* (1992) 86-92.
4. M. J. Crawford, University of Southampton, PhD Thesis (1995).